

**STUDYING THE EFFECTS OF NORADRENERGIC
NEUROMODULATION ON THE BOLD GLOBAL SIGNAL AND
QUASI-PERIODIC PATTERNS IN RAT RS-FMRI**

A Dissertation
Presented to
The Academic Faculty

by

Nmachi Anumba

In Partial Fulfillment
of the Requirements for the Degree
Doctor of philosophy in the
Wallace H. Coulter Department of Biomedical Engineering

Georgia Institute of Technology and Emory University
May 2024

COPYRIGHT © 2024 BY NMACHI ANUMBA

**STUDYING THE EFFECTS OF NORADRENERGIC
NEUROMODULATION ON THE BOLD GLOBAL SIGNAL AND
QUASI-PERIODIC PATTERNS IN RAT RS-FMRI**

Approved by:

Dr. Shella Keilholz, Advisor
Department of Biomedical Engineering
*Georgia Institute of Technology and Emory
University*

Dr. Garrett Stanley
Department of Biomedical Engineering
*Georgia Institute of Technology and
Emory University*

Dr. David Weinshenker
Department of Human Genetics
Emory University

Dr. Candace Fleischer
Department of Radiology and Imaging
Sciences
Emory University

Dr. Erin Buckley
Department of Biomedical Engineering
*Georgia Institute of Technology and Emory
University*

Date Approved: March 25, 2024

To Adonai El Roi

ACKNOWLEDGEMENTS

There are numerous people I would like to thank for their help in the completion of this dissertation and their contribution to my graduate journey. I would be remiss to not start this section without first thanking my loving God, without whom I very likely would not be in graduate school and most definitely would not have had the strength to finish. This is for Him.

I would like to thank my advisor, Dr. Shella Keilholz for all of her support, guidance, and direction throughout this research. I am beyond blessed to have worked with such an amazing scientist and person, thank you for making my grad school experience so great. The majority of this work would not have been possible without the work, dedication, and support of my colleague and good friend Dr. Michael Kelberman. Thank you for doing this with me and sharing your brilliance with the rest of us. I have to thank the Keilholz MIND lab, yes for their scientific contributions, but also for the laughs they have given me throughout the years. Thank you to my committee: Dr. Garrett Stanley, Dr. Erin Buckley, Dr. Candace Fleischer, and Dr. David Weinshenker for their guidance with these projects. A special shoutout to the Weinshenker lab for adopting me and teaching me about the locus coeruleus. Thank you to all my friends, both near and far, for all of the emotional support and great memories you have provided over the past five years, you are also a part of this. Lastly, thank you to my incredible family. My parents, Claire and Chimay Anumba, for always believing in me never neglecting to mention how proud you are. And my sisters (read *best friends*), Kenechi and Chioma... welp, *shrugs* I couldn't have done it without you.

TABLE OF CONTENTS

ACKNOWLEDGEMENTS	iv
LIST OF TABLES	vii
LIST OF FIGURES	viii
LIST OF SYMBOLS AND ABBREVIATIONS	x
SUMMARY	xi
CHAPTER 1. INTRODUCTION	1
CHAPTER 2. ISOLATING A NEURAL COMPONENT OF THE GLOBAL SIGNAL IN A NOISE-CONTROLLED COHORT OF RATS	4
2.1 Background	5
2.2 Methods	8
2.2.1 Animal Preparation	8
2.2.2 Data Acquisition	10
2.2.3 Preprocessing	11
2.2.4 Global Signal Comparison to Non-Brain Tissue Signal	13
2.2.5 Power Analysis	14
2.2.6 Signal Spatial Correlation Analysis	15
2.2.7 Default Mode Network Analysis	15
2.2.8 Co-activation Pattern Analysis	15
2.3 Results	16
2.3.1 Power Distribution Results	17
2.3.2 Non-Brain Tissue vs. Brain Results	20
2.3.3 DMN Relationship to The Global Signal	24
2.3.4 CAPs Results	26
2.4 Discussion	28
2.4.1 Differences in Power Distribution	28
2.4.2 DMN Contribution to The Global Signal	30
2.4.3 Effects of Anesthesia on Results	32
2.4.4 Limitations	34
2.5 Conclusion	34
CHAPTER 3. INVESTIGATING THE EFFECTS OF LC STIMULATION ON THE GLOBAL SIGNAL AND QPPS	36
3.1 Background	37
3.2 Materials and Methods	41
3.2.1 Animal Preparation	42
3.2.2 Surgery and Pupillometry	44
3.2.3 fMRI Data Acquisition	45
3.2.4 Preprocessing	49

3.2.5	Tissue Preparation and Immunohistochemistry	49
3.2.6	Data Analysis	50
3.3	Results	54
3.3.1	Multimodal Confirmation of Optogenetic LC Stimulation	54
3.3.2	Functional Connectivity	56
3.3.3	Spatial Distribution of the Global Signal	61
3.3.4	Power Spectral Density Analysis of the Global Signal	62
3.3.5	QPP Analysis	63
3.3.6	Complex Principal Component Analysis (CPCA)	66
3.4	Discussion	74
3.4.1	LC Stimulation and Functional Connectivity	75
3.4.2	WT vs. AD Functional Connectivity	76
3.4.3	LC Stimulation and the Global Signal	78
3.4.4	LC Stimulation and QPPs	80
3.4.5	CPCA Findings	82
3.4.6	Potential Subtle Effects	84
3.4.7	Limitations	85
3.5	Conclusion	86
APPENDIX A. ADDITIONAL DATA FROM OPTOGENETIC-FMRI EXPERIMENTS		88
A.1	Animal Group Sizes and Sex	89
A.2	Functional Connectivity	90
A.3	Spatial Distribution of the Global Signal	93
A.4	QPP Analysis	95
REFERENCES		98

LIST OF TABLES

Table 2.1	Timeline of Anesthetic Application for Each Subject.	10
Table 3.1	Animal group sizes.	43
Appendix Table 1	Remaining Animal Group Sizes.	89
Appendix Table 2	Animal Group Sizes by Sex.	90

LIST OF FIGURES

Figure 2.1	Rat Brain Signal vs. Non-Brain Tissue Signal.	13
Figure 2.2	Power Distribution of the Brain Global Signal and the Tissue Signal.	18
Figure 2.3	Analysis of the Last 30 Minutes of Dexmedetomidine Scans.	19
Figure 2.4	Spatial Distribution of Power Under Isoflurane.	20
Figure 2.5	Correlation Values Between the Brain Global Signal and the Non-Brain Tissue Signal.	21
Figure 2.6	Spatial Correlation to the Brain Global Signal and the Non-Brain Tissue Signal.	23
Figure 2.7	Default Mode Network (DMN) Regional Relationship to the Global Signal.	25
Figure 2.8	Z-scored Co-Activation Patterns (CAPs) to the Global Signal and the Non-Brain Tissue Signal.	27
Figure 3.1	Methods timeline of optogenetic-fMRI experiments.	41
Figure 3.2	Scanning session timeline.	47
Figure 3.3	Confirmation of LC optogenetic stimulation and LC noradrenergic activity.	55
Figure 3.4	Functional connectivity differences as a result of LC stimulation.	57
Figure 3.5	Functional connectivity matrices as divided by stimulated hemisphere.	58
Figure 3.6	Functional connectivity differences between WT and AD animals.	60
Figure 3.7	Spatial distribution of the global signal during LC stimulation.	62
Figure 3.8	Power spectral density (PSD) estimates of the global signal.	63
Figure 3.9	QPP detection and templates.	65
Figure 3.10	Incidence percentage of the first three principal components during LC stimulation.	67

Figure 3.11	Incidence of the first three principal components throughout each scan during LC stimulation.	69
Figure 3.12	A representative look into the first three principal components in WT and AD animals.	70
Figure 3.13	Incidence percentage of the first three principal components in WT and AD animals.	73
Appendix Figure 1	Flowchart of Data Acquired.	88
Appendix Figure 2	Functional connectivity for 6-month AD ChR2 animals.	91
Appendix Figure 3	Functional connectivity for 15-month WT ChR2 Animals.	92
Appendix Figure 4	Functional connectivity for 15-month AD ChR2 animals.	93
Appendix Figure 5	Spatial distribution of the global signal for 6-month AD animals.	94
Appendix Figure 6	Spatial distribution of the global signal for 15-month WT animals.	94
Appendix Figure 7	Spatial distribution of the global signal for 15-month AD animals.	95
Appendix Figure 8	QPP templates for 6-month AD animals.	96
Appendix Figure 9	QPP templates for 15-month WT animals.	96
Appendix Figure 10	QPP templates for 15-month AD animals.	97

LIST OF SYMBOLS AND ABBREVIATIONS

AD	Alzheimer's Disease
BOLD	Blood Oxygen Level Dependent
CAP	Co-Activation Pattern
CPCA	Complex Principal Component Analysis
DMN	Default Mode Network
fALFF	Fractional Amplitude of low-Frequency Fluctuations
FDR	False Discovery Rate
GSR	Global Signal Regression
LC	Locus Coeruleus
LC-NE	Locus Coeruleus – Norepinephrine (system)
PSD	Power Spectral Density
QPP	Quasi-Periodic Pattern
ROI	Region of Interest
rs-fMRI	Resting-state Functional Magnetic Resonance Imaging
STC	Sliding Template Correlation
TPN	Task Positive Network
WT	Wildtype

SUMMARY

The study of dynamically changing resting-state fMRI (rs-fMRI) signals that span multiple brain regions provides an opportunity to better understand the intrinsic contexts of large-scale communication across the brain. Two prominent examples of these whole-brain spatiotemporal patterns are the blood oxygen level dependent (BOLD) global signal and quasi-periodic patterns (QPPs). The BOLD global signal is defined as the averaged activity of the brain during a scan and its use as a nuisance regressor has been a contentious topic for years. QPPs are propagating waves of anticorrelated activity that alternate between two prominent resting-state brain networks, though their origin is unknown. Both of these signals have been shown to exhibit notable relationships with measures of arousal and vigilance. Activity of the locus coeruleus (LC), a brainstem nucleus responsible for the synthesis and release of norepinephrine, is known to play a significant role in arousal. Speculation that QPPs may originate from the activity of brainstem nuclei, in addition to findings that link the global signal to levels of arousal, led us to believe that the widespread nature of LC influence could have a significant effect on these two signals. In this work we studied the direct effects of LC activity on the BOLD global signal and QPPs in rats. This was done by first identifying a neural global signal component in a noise-controlled environment that could consequently be affected by LC neuromodulation (Aim 1). Secondly, we used optogenetic-fMRI to stimulate the LC at different frequencies and study how these varying levels of LC activity affected both the global signal and QPPs in rats (Aim 2). Both spatiotemporal signals were analyzed both through traditional methods and through the employment of complex principal component analysis (CPCA). Our findings

show evidence for a neural global signal component that is distinct from noise. We also report spatially specific changes in global signal distribution under tonic LC stimulation as well as regional changes in QPP involvement under 5 Hz tonic and 15 Hz phasic stimulation. Given that the LC is also strongly implicated in Alzheimer's disease (AD), we also used the AD rat model TgF344-AD to investigate the effects of the disease on whole-brain dynamics using CPCA, for which we show age-specific AD effects. These results show that the neuromodulatory effects of the LC norepinephrine system on large-scale spatiotemporal patterns may be small in scale and more regionally specific than initially thought.

CHAPTER 1. INTRODUCTION

Throughout the years, the field of neuroscience has learned a lot about how specific parts of the brain correspond to specific actions and behaviors. More recently, there has been an increase in studies of at-rest brain activity that showcase dynamics and networks underlying important brain functions. In resting-state fMRI (rs-fMRI), performed when the subject is awake but not involved in a task, there is a unique opportunity to study the brain's intrinsic functionality through the blood oxygenation level dependent (BOLD) signal. However, as a result of this data being acquired at rest, there is also a real need to parse out what is considered signal and what is considered noise. One preprocessing step that has long been used to denoise rs-fMRI data is the removal of the global signal, most frequently achieved by global signal regression (GSR). In BOLD fMRI, the global signal is calculated by averaging the timecourses of all voxels in the brain region. This practice is motivated by the principle that any widespread fluctuations that are captured by this global average are likely to be the result of widespread sources of noise, such as head motion or non-relevant physiological activity. Should this be the case, GSR should considerably decrease the noise contained in rs-fMRI data. In fact, GSR has been shown to be effective in reducing noise from motion (Parkes et al., 2018; Satterthwaite et al., 2012; Yan et al., 2013) and physiological sources (Birn et al., 2006). Despite this, controversy remains surrounding GSR and the implications of removing the global signal from each voxel timecourse. Many argue that a blind average of every voxel in the brain leaves too many questions about its contents to comfortably regress it out of a dataset (T. T. Liu et al., 2017). Further reasoning against GSR says that the existence of widespread coherent activity in the form of resting-

state networks or whole-brain dynamics means that GSR could be removing neural data of interest, consequently affecting result outcomes and the interpretation of rs-fMRI studies (Ciric et al., 2017; Fox et al., 2009; Murphy & Fox, 2017; Saad et al., 2012).

The question of whether coordinated activity from different regions across the brain are captured in the global signal brings attention to whole-brain dynamic activity such as quasi-periodic patterns (QPPs). QPPs are defined as patterns of alternating levels of activation between different networks and brain areas that are observed as propagating throughout the brain (Majeed et al., 2011). Linked to infra-slow neural activity (< 0.1 Hz), QPPs have been observed in both rodents and humans and have been shown to contribute to functional connectivity (Abbas, Belloy, et al., 2019; Belloy, Naeyaert, et al., 2018; Majeed et al., 2009, 2011). In humans they often take the form of periodic anticorrelation between two resting-state networks: The default mode network (DMN) and the task positive network (TPN), whereas in rodents they are often observed as waves of high and low activation that propagate medially from lateral cortical areas (Majeed et al., 2011). These periodic waves of activation are thought to organize activity across the brain and contribute to the global signal (Belloy, Naeyaert, et al., 2018; Yousefi et al., 2018). Additionally, they have been shown to inform functional connectivity differences in attention deficit/hyperactivity disorder (ADHD) and improve classification of Alzheimer's disease (Abbas, Bassil, et al., 2019; Belloy, Shah, et al., 2018).

When considering these forms of dynamic brain activity, it is important to note that while at rest, brain activity is subject to constant neuromodulatory input from brainstem nuclei. These inputs can be in response to a stimulus or the result of baseline homeostatic maintenance. Either way, the effects of this neuromodulation on resting-state activity are

an important element of the complex intrinsic brain dynamics and connectivity being studied. In particular, the noradrenergic system of the locus coeruleus (LC) is of special interest as its involvement in arousal makes it a key contender for studying the global signal and global activity, which themselves have been related to levels of arousal (Chang et al., 2016; Deco et al., 2014; Pisauro et al., 2016). The LC, located in the brainstem, is primarily known for its role as the noradrenergic center of the central nervous system. Due to its dense projections throughout the brain and modulation through the release of norepinephrine, the LC plays a significant role in cognition, attention, and arousal (Aston-Jones & Cohen, 2005; Benarroch, 2018). Through its vast connections to many brain structures, the LC has the potential to influence whole-brain activity and connectivity. Not only are general brain states and levels of activity known to fluctuate during resting state, but pupil diameter, which is often used as a proxy for LC activity, has also been shown to fluctuate at rest (Schneider et al., 2016).

This dissertation summarizes the research that was done to investigate the role of LC activity on both the global signal and QPPs in rats. CHAPTER 2 summarizes the work done to provide evidence toward a neural component of the global signal in a cohort of rats for which contributions of noise were substantially controlled. CHAPTER 3 summarizes work in which optogenetics and fMRI were combined to study the effects of optogenetically stimulating the LC at different frequencies on both the global signal and QPPs.

CHAPTER 2. ISOLATING A NEURAL COMPONENT OF THE GLOBAL SIGNAL IN A NOISE-CONTROLLED COHORT OF RATS

Motivation: In resting-state fMRI (rs-fMRI), the global signal average captures widespread fluctuations related to unwanted sources of variance such as motion and respiration, as well as widespread neural activity, however relative contributions of neural and non-neural sources to the global signal remain poorly understood. This study sought to tackle this problem through the comparison of the BOLD global signal to an adjacent non-brain tissue signal, where neural activity was absent, from the same rs-fMRI scan obtained from anesthetized rats. In this dataset motion was minimal and ventilation was phase-locked to image acquisition to minimize respiratory fluctuations. Data was acquired using three different anesthetics: isoflurane, dexmedetomidine, and a combination of dexmedetomidine and light isoflurane.

Methods: A power spectral density estimate, a voxel-wise spatial correlation via Pearson's correlation, and a co-activation pattern analysis were performed using the global signal and the non-brain tissue signal. Functional connectivity was calculated using Pearson's linear correlation on default mode network (DMN) regions.

Results: We report differences in the spectral composition of the two signals (Section 2.3.1) and show spatial selectivity within DMN structures that show an increased correlation to the global signal (Sections 2.3.2 and 2.3.4) and decreased intra-network connectivity after global signal regression (Section 2.3.3). All of the observed differences between the global signal and the non-brain tissue signal were maintained across anesthetics.

Conclusion: These results show that the global signal is distinct from the noise contained in the tissue signal, as support for a neural contribution. This study provides a unique perspective to the contents of the global signal and their origins.

2.1 Background

In resting-state functional magnetic resonance imaging (rs-fMRI), there is a unique opportunity to study the brain's intrinsic functional organization as captured by low-frequency fluctuations in the blood oxygen level dependent (BOLD) signal (Biswal et al., 1995). However, the spontaneous BOLD fluctuations are small (Pais-Roldán et al., 2018) and contributions arising from neural activity can easily be swamped by signal changes related to motion and respiration (Murphy et al., 2013; Power et al., 2017). To minimize unwanted signal changes from non-neural sources, the average of the BOLD signal from all voxels in the brain ('global signal') is often regressed from data during preprocessing (Aguirre et al., 1998; Macey et al., 2004; Murphy & Fox, 2017; Zarahn et al., 1997). Despite the success of global signal removal as a denoising step (Birn et al., 2006; Parkes et al., 2018; Satterthwaite et al., 2012; Wise et al., 2004; Yan et al., 2013), regression of the signal remains controversial as many argue that the global signal contains relevant neural data (Ciric et al., 2017; Fox et al., 2009; T. T. Liu et al., 2017; Murphy & Fox, 2017; Saad et al., 2012).

The removal of the global signal from rs-fMRI data is primarily motivated by the principle that the majority of widespread fluctuations captured by this global average are the result of widespread sources of noise. Major sources of noise that are known to be

reflected in the global signal are motion (Parkes et al., 2018; Satterthwaite et al., 2012; Yan et al., 2013) and physiological factors such as cardiac pulsation, vascular tone, and changes in cerebral blood flow (Birn et al., 2006; Wise et al., 2004). These types of noise tend to be reflected in large portions of the brain signal, at times in the whole image, and their influence on image quality can be significantly reduced through global signal removal (Ciric et al., 2017; Fox et al., 2009; T. T. Liu et al., 2017; Murphy & Fox, 2017; Saad et al., 2012). These types of noise affect both brain signal and that of anatomical structures surrounding it. Imaged features such as the skull or surrounding head tissue are also affected by head motion, any whole-image scanner noise, and magnetic field shifts due to respiratory or other forms of motion. When comparing human and rodent imaging, the imaged head tissue in humans is minimal, whereas there is substantially more tissue surrounding the brain in rodents. A signal comprised of such tissues has been considered as a non-interest covariate in rodent fMRI preprocessing and could serve as a comparative measure for the global signal (Chuang et al., 2019; Lowe et al., 2008). As such, a rodent study comparing the global signal to the signal contained in these surrounding structures has the potential to elucidate neural contributions to the global signal.

The data used in this study was acquired using a protocol that was optimized to minimize motion and respiratory noise to better isolate the non-noise components captured in the BOLD signal. These noise-limiting steps included mechanical ventilation, the use of a paralytic, employment of stereotaxic head-fixation, and respiratory phase-locked image acquisition. With these procedures in place, we aimed to study the global signal in the context of minimal noise. An important tool for minimizing noise in rodent rs-fMRI is the use of anesthesia, which allows animals to be head-fixed without pain or stress and prevents

voluntary motion that can affect the magnetic field. However, the anesthetic agents used can affect neurovascular coupling (Franceschini et al., 2010) and induce potential confounds into the rs-fMRI data. Two of the most commonly used anesthetics for rodent rs-fMRI are isoflurane and dexmedetomidine. Each of these anesthetics can induce changes in vascular tone and cerebral blood flow. Isoflurane is a vasodilator which increases cerebral blood flow (Sicard et al., 2003) while dexmedetomidine is a vasoconstrictor which decreases cerebral blood flow (Ganjoo et al., 1998). These effects can influence measurements of functional connectivity (Grandjean et al., 2014) and even alter which frequency bands exhibit the greatest coherence between rs-fMRI and local field potentials (Pan et al., 2013). A common method in rodent rs-fMRI is to use a combination of both isoflurane and dexmedetomidine because the vasodilatory effects of isoflurane have been shown to be attenuated by the opposing vascular effects of dexmedetomidine (Ohata et al., 1999).

In this work, we investigated the spatial and spectral differences between the brain global signal and a same-scan adjacent non-brain tissue signal across three different anesthetic conditions: isoflurane, dexmedetomidine, and a combination of the two (isodex). The use of multiple anesthetics ensured that results were not specific to a single anesthetic condition. We examined how the tissue and brain signals differed through a power spectral density analysis, a voxel-wise correlation analysis, and a dynamic co-activation pattern (CAP) analysis. We provide evidence that the global signal contains specific spectral and spatial qualities that are separate from noise and could be linked to brain activity. Additionally, these findings were robust across the use of the different anesthetic protocols. The results of this study provide unique insight into the composition of the global signal.

2.2 Methods

2.2.1 Animal Preparation

All protocols were approved by the Institutional Animal Care and Use Committee (IACUC) and all procedures were performed in strict compliance with the IACUC protocols. Data was acquired from eight male Sprague Dawley rats (299g – 339g, Charles River). Animals were inducted under 5% isoflurane and were maintained at 2% isoflurane during handling and placement in the MRI cradle. All rats were intubated and underwent ventilator-assisted breathing at a rate of 1 Hz. An infusion line was inserted subcutaneously to administer the paralytic pancuronium at a rate of 1.5 mg/kg/hr for the duration of the scan. Animals were placed in a homemade custom MRI cradle and positioned with their teeth secured in a bite bar and their heads fixed using ear bars.

After preparation, the animals underwent a scanning session in which scans were consecutively collected under three different anesthetic protocols: isoflurane alone, dexmedetomidine alone, and a combination of dexmedetomidine with light isoflurane (isodex). Initially, animals were scanned under 2% isoflurane as part of a separate study; however these scans were not included in the analyses for this paper as deep levels of isoflurane have been shown to result in burst suppression and increase the spatial extent of contribution to the global signal (X. Liu et al., 2013). Afterwards, isoflurane was reduced to 1.5% and the animals were scanned for an average of 35 minutes. After the isoflurane scan, the animals were subcutaneously injected with a 0.025 mg/kg bolus of dexmedetomidine, taken off isoflurane five minutes later, and then switched to a 0.05

mg/kg/hr subcutaneous infusion of dexmedetomidine at 10 minutes post-bolus. The animals were then scanned again while exclusively under dexmedetomidine for an average of about 61 minutes. Functional dexmedetomidine scans were started an average of about 14 minutes after isoflurane was disconnected. Afterwards, the animals were introduced to a low dose of isoflurane at 0.5% in combination with the 0.05 mg/kg/hr subcutaneous infusion of dexmedetomidine. The animals were then scanned a final time while under isodex for 49 minutes on average. Functional isodex scans were started an average of 17 minutes after the low dose of isoflurane was introduced. A table with the exact timing of anesthetic introduction and image acquisition for each rat is displayed in Table 2.1. To use the maximum amount of data possible in accordance with the length of the shortest scan, only the first 30 minutes of the isoflurane and dexmedetomidine scans and the first 20 minutes of the isodex scans were used for the group analysis. The last 30 minutes of dexmedetomidine scans were also analyzed to compare for any unwanted effects of lingering isoflurane that could be present in the first 30 minutes of these scans. Physiological parameters of the animal were measured using a pulse oximeter that was placed on a hindpaw of the animal and through a rectal temperature probe. Temperature of the animal was maintained around 37 ± 0.5 °C using a heated water bath system.

Table 2.1 Timeline of Anesthetic Application for Each Subject.

	Length of isoflurane scan (minutes)	Time after disconnection of isoflurane that dexmedetomidine scan starts (minutes)	Length of dexmedetomidine scan (minutes)	Time after introduction of 0.5% isoflurane that isodex scan starts (minutes)	Length of isodex scan (minutes)
Subject 1	30	23	60	32	60
Subject 2	30	19	60	7	60
Subject 3	30	14	80	17	30
Subject 4	30	8	80	23	20
Subject 5	60	5	30	12	30
Subject 6	40	17	60	14	40
Subject 7	30	12	60	13	60
Subject 8	30	13	60	18	90

2.2.2 Data Acquisition

MRI data was acquired using a 20 cm horizontal bore 9.4 T Bruker Biospec MRI and a homemade transmit-receiver surface coil. A T2-weighted rapid acquisition with relaxation enhancement (RARE) anatomical scan was acquired for each rat (TR = 3500 ms, TE = 11 ms, 24 axial slices, 0.5 mm³ isotropic voxels). All functional rs-fMRI scans were acquired using a gradient-echo echo-planar imaging (EPI) sequence with the following parameters: partial Fourier encoding with a factor of 1.4, field of view (FOV) of 35x35 mm², matrix size of 70x70, isotropic voxel size of 0.5 mm³, 24 axial slices for whole-brain coverage, a flip angle of 68.4°, bandwidth = 216.45 kHz, TE = 15 ms, and TR = 2000 ms. A 3-volume reverse phase encoding blip EPI image with the aforementioned parameters was acquired before each longer functional scan for topup correction

(Andersson et al., 2003; Smith et al., 2004). All functional EPI scans included saturation bands to minimize signal from frontal and ventral regions outside the brain and were preceded by 10 dummy scans.

All functional EPI scans were phase-locked, meaning that the acquisition of the images was set to a multiple of the animal's respiratory rate so that each image was acquired during the same phase of the respiratory cycle (Pan et al., 2020). This practice was adopted to limit any effects of motion that could arise from movement of the chest cavity and volumes being imaged at different points in the respiratory cycle. In this study, images were acquired at a frequency of every other breath, or 2 Hz (TR = 2000 ms).

2.2.3 *Preprocessing*

All preprocessing of the data was performed using the following software: FSL (Jenkinson et al., 2012), Analysis of Functional NeuroImages (AFNI) (Cox, 1996), ITK-SNAP (Yushkevich et al., 2006), and ANTs (Avants et al., 2008). Distortion correction was applied to all scans using FSL Topup and volume registration to the 30th volume of each scan was performed using AFNI 3dVolReg. Motion regression (6 parameters and up to 2 polynomials) and bandpass filtering (0.01 – 0.2 Hz) were performed in one step using AFNI 3dTProject. The frequency filter range was chosen to compare all anesthetic conditions across the same frequencies, according to previous work that has shown contributions from higher frequencies at resting state under dexmedetomidine (0.01 – 0.25 Hz) than under isoflurane (0.01 – 0.1 Hz) (Pan et al., 2013). Spatial smoothing was not applied to this data as smoothing the non-brain tissue signal may have had differential

effects due to it being much smaller than the brain. Brain masks for each scan were acquired automatically in AFNI using 3dAutomask. The non-brain tissue signal was comprised of the skull, fat, and muscle surrounding the brain. Individual non-brain tissue masks were acquired manually using ITK-Snap and created to consist of 500 – 600 voxels for each scan. Areas of tissue closest to the brain were chosen for these masks in order to obtain good signal and maximize similarities in the types of noise that would affect both signals (Figure 2.1). The individual brain and non-brain tissue masks were then used to segment the two signals for analysis. For group average signals, all scans were aligned to a single subject using direct, linear EPI to EPI registration via AFNI 3dAllineate. For the group voxel-wise correlation analysis, scan segments, global signals, and non-brain tissue signals from each rat were concatenated. For analyses involving structures in the default mode network, the SIGMA-Wistar anatomical atlas (Barrière et al., 2019) was inversely registered to the single subject mentioned previously using antsRegistration.

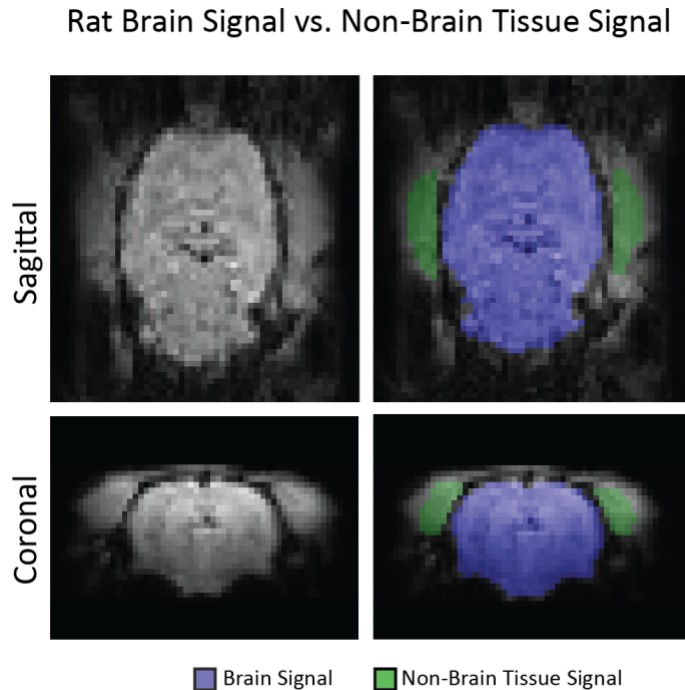


Figure 2.1 Rat Brain Signal vs. Non-Brain Tissue Signal. Rat anatomy results in notably more non-brain tissue being imaged around the brain than is observed in human imaging. This figure shows slices from a functional scan of subject 6 (left column) and then shows those same slices with the actual non-brain tissue mask used in this study as well as a representative brain mask (right column). The substantial amount of tissue imaged alongside the brain in rats allowed us to carry out these adjacent signal comparisons.

2.2.4 *Global Signal Comparison to Non-Brain Tissue Signal*

A comparison was made between the global signal and the averaged signal of the surrounding tissue in the same scan. This was done to identify any characteristics of the global signal that could be consistently linked to brain activity and were separate from noise. The rationale between comparing these two signals comes from the fact that both signals would be affected by any residual motion, scanner noise, and magnetic field shifts that were to occur. Therefore, any signal attributes that result from brain activity would

stay confined within the global signal, whereas any signal characteristics that primarily reflect noise would potentially be observed in both signals. In this way, the tissue signal acts as a comparable noise measure.

All analyses of these signals were performed in MATLAB using custom scripts. The global signal was calculated by averaging the timecourses of all voxels within the brain and then z-scoring the signal by subtracting its mean and dividing by its standard deviation. The tissue signals were calculated in a similar manner, by averaging the timecourses of all voxels within the segmented tissue region and z-scoring them.

2.2.5 Power Analysis

Power spectral density (PSD) estimates of the global signal were compared to those of the tissue signal to evaluate the various frequency contributions within the range of 0.01 – 0.2 Hz. PSDs were computed in MATLAB using Welch’s method with a Hamming window and 50% overlap. The PSDs found for each individual scan were averaged to create the group average for each anesthetic group. These PSDs were then normalized to a scale of 0 to 1 for simple comparison. The fractional amplitude of low-frequency fluctuations (fALFF), as defined by Zou *et al.* (Zou et al., 2008), was calculated for each power spectrum by summing the square root of the power within the 0.01 – 0.08 Hz range and dividing this by the sum of the square root of the power across the entire frequency range (0.01 – 0.2 Hz). A voxel-wise power distribution map was calculated by summing the power at each voxel over a specified frequency range. In accordance with previous findings that showed selective frequency ranges for peak BOLD-LFP coupling under

different anesthetics, the frequency ranges used were 0.01 – 0.1 Hz for isoflurane scans and 0.01 – 0.25 Hz for dexmedetomidine and isodex scans (Pan et al., 2013).

2.2.6 Signal Spatial Correlation Analysis

The global signal and the non-brain tissue signal for each scan were correlated using Pearson's linear correlation. A voxel-wise correlation analysis was performed in which a Pearson's linear correlation was calculated between the global signal and each voxel timecourse within the brain, and again with the non-brain tissue signal and each voxel timecourse within the brain.

2.2.7 Default Mode Network Analysis

To assess the involvement of structures in the default mode network (DMN), select regions were extracted using the SIGMA-Wistar anatomical atlas (Barrière et al., 2019) and according to the list of rat DMN structures reported in Lu et al., 2012 (Lu et al., 2012) that corresponded to the atlas. Bilateral regions were averaged to create one region. All analysis was done in MATLAB using custom scripts.

2.2.8 Co-activation Pattern Analysis

To compare the non-brain tissue and brain global signals as they vary over time, as opposed to the static correlation comparison, we performed a co-activation pattern (CAP)

analysis. CAP analysis is a dynamic analysis method that was first proposed by Liu and Duyn (X. Liu & Duyn, 2013). This method involves choosing a seed region or region of interest (ROI) and setting a threshold for that ROI signal. The timepoints at which the ROI signal passes the threshold are used to extract fMRI volumes, which are then clustered and averaged to produce different CAPs. We took advantage of CAP analysis to identify areas of the brain that are co-active with peaks in activity of the global signal and the non-brain tissue signal. This was done by using the two signals as distinct ROIs to calculate two separate CAPs. The tissue CAP and the global signal CAP were calculated individually for each scan. These individual CAPs were averaged for each group as a representative pattern that highlights the major structures involved, as has been demonstrated previously (X. Liu, de Zwart, et al., 2018; X. Liu, Zhang, et al., 2018). The ROI signal timecourses were z-scored and the threshold was set to a z-score greater than 1 to capture about the top 15% of peaks in each ROI timecourse, as is common practice (X. Liu & Duyn, 2013; Maltbie et al., 2022). For each ROI, all frames at timepoints that exceeded the threshold were averaged resulting in the global signal and non-brain tissue signal CAPs.

2.3 Results

We studied both spectral and spatial features of the global signal in eight male Sprague Dawley rats. These characteristics were compared to a same-scan non-brain tissue signal that was segmented for each rat. This section includes the group results for each analysis.

2.3.1 Power Distribution Results

We created a PSD estimate for both the global signal and the non-brain tissue signal for each scan (Figure 2.2A). The group average power spectra are shown for scans under isoflurane, dexmedetomidine, and isodex. The comparison of the contributing frequencies in both signals across anesthetics shows distinct differences between the global signal and the non-brain tissue signal. Most notably, the tissue signal appears to exhibit a higher proportion of low-frequency contribution to the overall signal. To evaluate this, we calculated the fractional amplitude of low-frequency fluctuations (fALFF) (Zou et al., 2008) for each trace. The fALFF values for the global signal were 0.4398, 0.4652, and 0.4393 for isoflurane, dexmedetomidine, and isodex, respectively. However, all conditions showed an increase in fALFF for the tissue signal with fALFF values being 0.5181, 0.4811, and 0.5049 for isoflurane, dexmedetomidine, and isodex, respectively. The differences displayed in these power spectral plots emphasize the distinct spectral constitutions of these two signals, implying that there may be certain activity captured in the global signal that is not being captured in the tissue signal. It is also important to note that the spectra themselves look different across anesthetic conditions for the two signals. In particular, the tissue signal shows two small peaks around 0.02 Hz under isoflurane and two bigger more distinct peaks around 0.02 and 0.05 Hz under isodex. The global signal also has a notable drop in power around 0.03 and 0.02 Hz under isoflurane and dexmedetomidine, respectively, however under isodex the decrease in low frequency power is more gradual. Similar results to those shown under dexmedetomidine were also observed when analyzing the last 30 minutes of dexmedetomidine scans to account for any lingering effects of isoflurane (Figure 2.3).

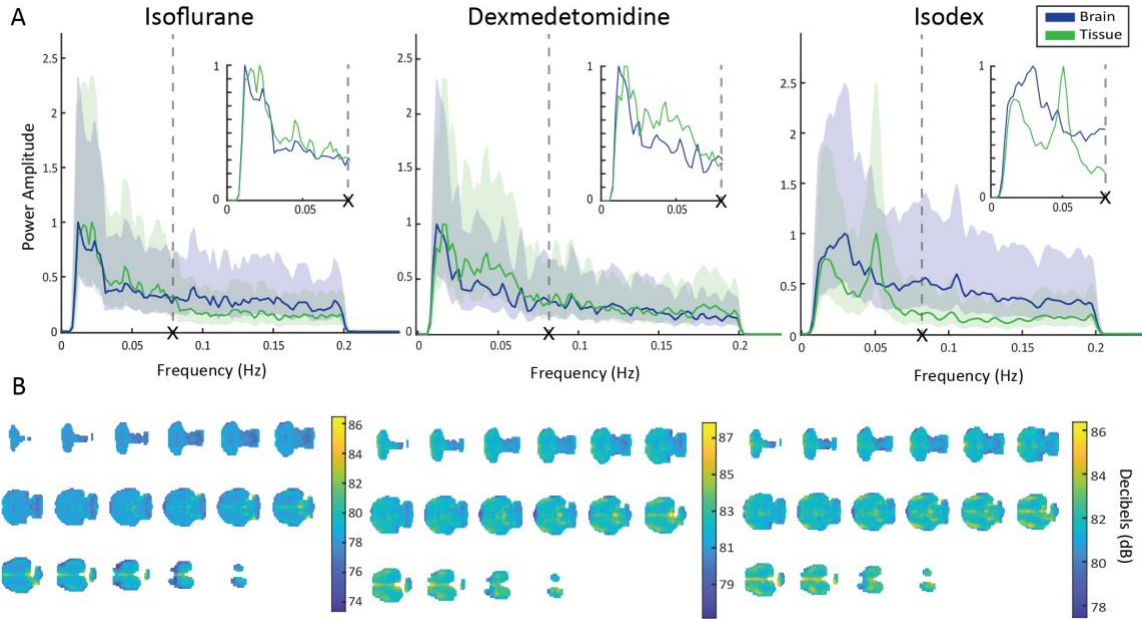


Figure 2.2 Power Distribution of the Brain Global Signal and the Tissue Signal. (A) Power spectral density estimates for the global signal (blue) and the non-brain tissue signal (green) across the three anesthetic conditions. A magnified version is provided for each group to better compare the low frequency differences between the two signals. The X and dashed line mark 0.08 Hz as used for the fALFF calculation. Under all three anesthetic conditions the tissue signal had a higher fALFF value than the brain global signal. (B) Group level spatial distribution of power across the brain under all anesthetic conditions, reported in decibels. High levels of power were localized to voxels along the posterior midline of the brain and, in the case of dexmedetomidine and isodex, bilaterally in the cortex.

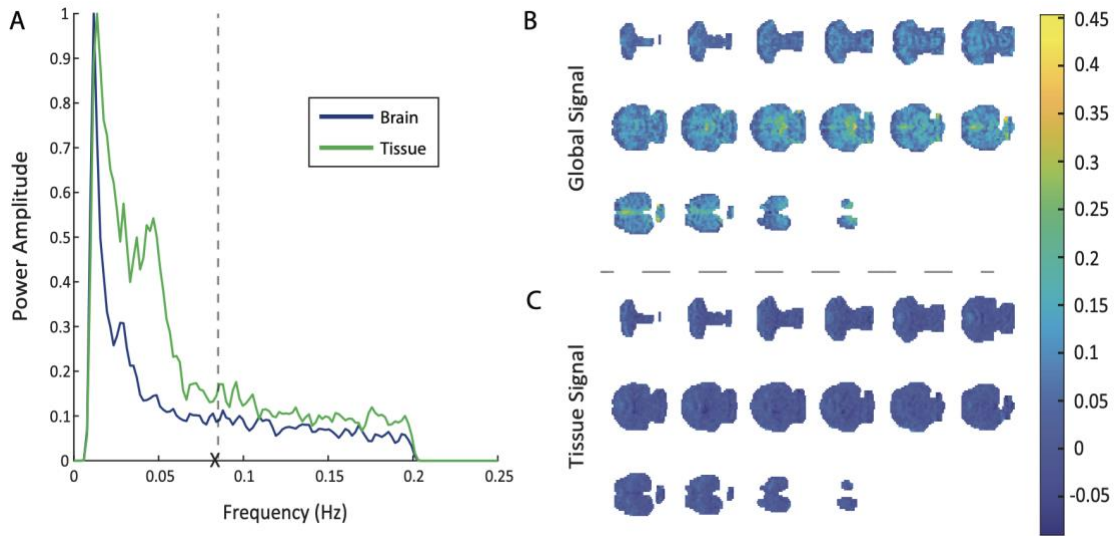


Figure 2.3 Analysis of the Last 30 Minutes of Dexmedetomidine Scans. To account for any lingering effects of isoflurane on the first 30 minutes of dexmedetomidine scans, we also looked at the PSD estimate and spatial correlation of the global and tissue signals in the last 30 minutes of these scans. For both analyses, we saw similar results to those presented in the main analysis. (A) The tissue signal consisted of a higher contribution from lower frequencies than the brain global signal, with the tissue signal having a fALFF of 0.5396 and the global signal having a fALFF of 0.5035. (B) A voxel-wise correlation to the global signal shows higher correlation to the global signal from medial brain structures, as was seen in the first 30 minutes. (C) The same voxel-wise analysis to the tissue signal shows lower overall correlation, as was seen in the first 30 minutes.

Additionally, we observed the power distribution of the brain signal across all three anesthetic conditions (Figure 2.2B). For scans acquired under isoflurane, we summed the power for each voxel over the 0.01 – 0.1 Hz range, for dexmedetomidine and isodex scans we summed the power over the 0.01 – 0.25 Hz range. Results are reported in decibels. Across all anesthetic conditions the highest amount of power is observed in a posterior medial part of the brain and throughout the entire medial section in more superior slices of the brain. Similar results were observed for isoflurane scans between 0.01 – 0.25 Hz (Figure 2.4) and in the last 30 minutes of dexmedetomidine scans (Figure 2.3).

Spatial Distribution of Power under Isoflurane

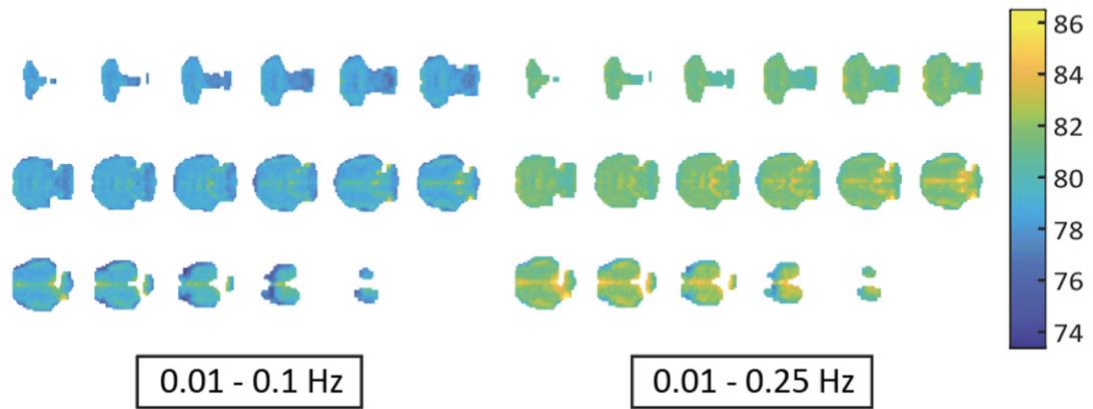


Figure 2.4 Spatial Distribution of Power Under Isoflurane. This figure shows the spatial distribution of power in the isoflurane scans over the original frequency range (0.01 – 0.1 Hz) and the frequency range used for dexmedetomidine and isodex (0.01 – 0.25 Hz). When the frequency range is expanded, the power levels throughout the brain increase by way of including more power values to the sum for each pixel. However, the distribution of power spatially does not change with the increased frequency range. In fact, the addition of more frequencies appears to increase the power in all regions proportionally so that the original spatial distribution of power is maintained.

2.3.2 *Non-Brain Tissue vs. Brain Results*

To show the distinct temporal nature of the global signal from the non-brain tissue signal, we performed a Pearson’s linear correlation to correlate the two signals for each scan at an individual level (Figure 2.5). The mean values of correlation from all eight rats were -0.0038, 0.0072, and 0.0313 for isoflurane, dexmedetomidine, and isodex, respectively. When analyzed with a one-sample t-test, these mean values were not statistically different from zero (isoflurane: $p = 0.8943$; dexmedetomidine: $p = 0.7925$; and

isodex: $p = 0.1357$). The correlation values for all rats were within the range of 0.15 to -0.15, reflecting little to no correlation. The lack of correlation between the global signal and the tissue signal show that even on an individual rat level there is very little similarity between these two signals and provides evidence that they contain different information.

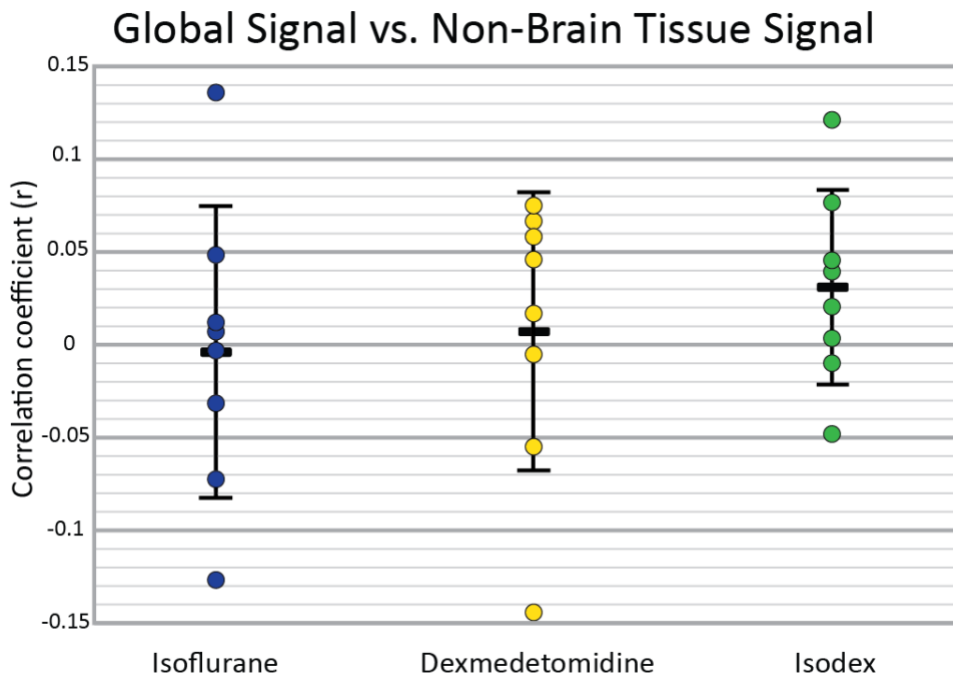


Figure 2.5 Correlation Values Between the Brain Global Signal and the Non-Brain Tissue Signal. The correlation between the global signal and the non-brain tissue signal for each rat across anesthetic conditions. Black rectangles represent the means for each group: isoflurane (blue) = -0.0038, dexmedetomidine (yellow) = 0.0072, isodex (green) = 0.0313. These means were not statistically different from zero ($p = 0.8943, 0.7925,$ and 0.1357 , respectively). The low r values indicate very little correlation between the two signals.

To demonstrate the spatial distribution of the global signal, we performed a voxel-wise correlation analysis (Figure 2.6). A Pearson's correlation between the global signal

and the timecourse of each voxel within the brain mask was computed. Similarly, we also computed the correlation between the tissue signal and the timecourse of each voxel. This comparison was made to display the fact that spatial patterns observed with the global signal were not the result of whole-image noise. The spatial correlation to the global signal across all anesthetic conditions showed higher correlation in an anterior medial part of the brain. In isoflurane scans, higher correlation is also shown bilaterally and throughout the outer cortical regions. Correlation to the global signal in dexmedetomidine scans was overall slightly lower and showed a weaker correlation than that seen bilaterally in cortex under the other two conditions. In isodex scans, there was also a high bilateral correlation to the global signal in anterior cortical regions. When comparing the global signal correlation to the non-brain tissue signal correlation, it can be seen that the tissue signal correlation was overall much lower and that there were no detectable spatial patterns. Note too that while high signal power was primarily localized to the midline (Figure 2.2B), correlation with the global signal also extends to anterior cortical areas (Figure 2.6), evidence that the global signal is not completely dominated by midline areas of strong fluctuation.

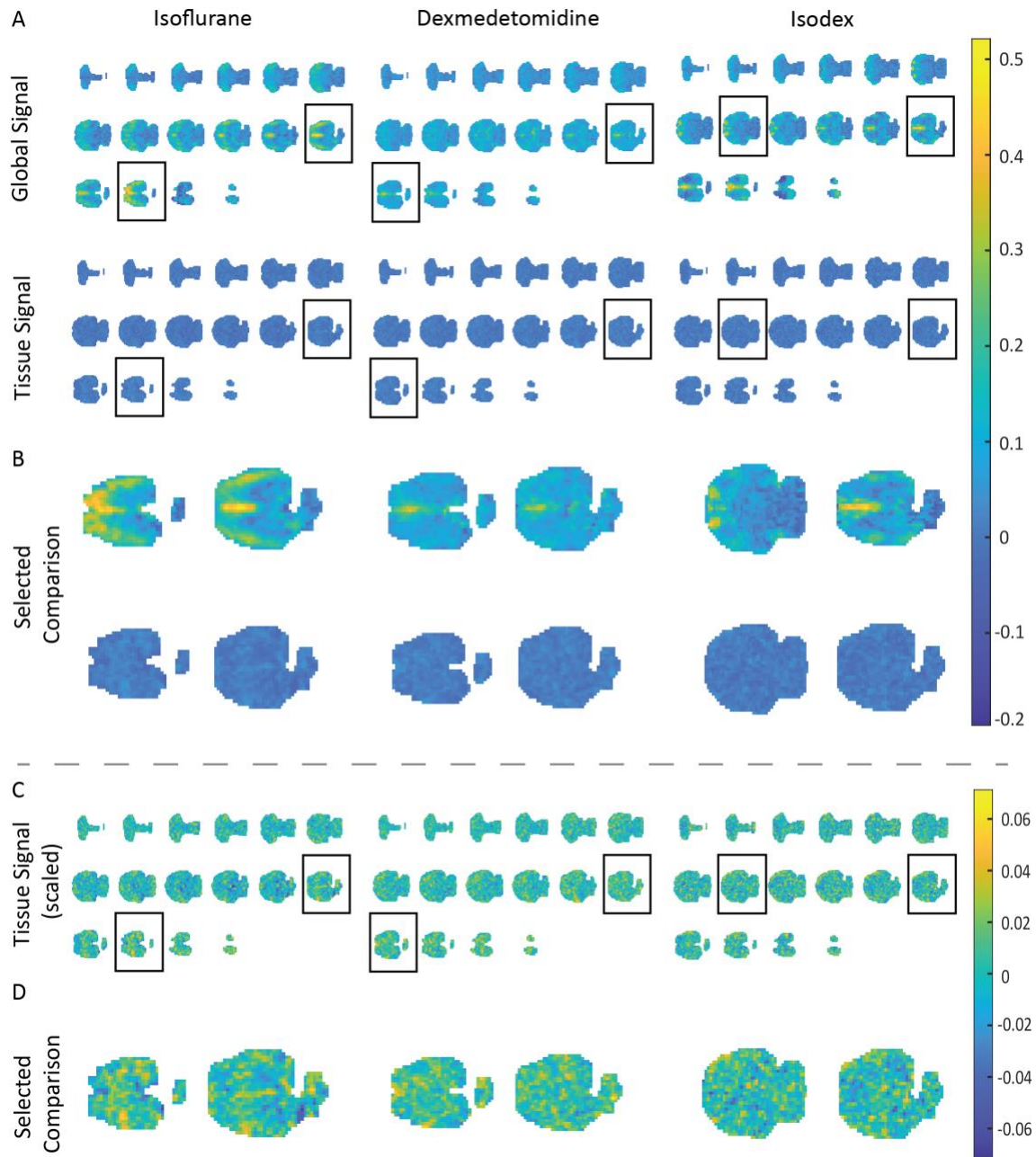


Figure 2.6 Spatial Correlation to the Brain Global Signal and the Non-Brain Tissue Signal. (A) The correlation of each voxel to the global signal (top row) and to the tissue signal (bottom row). Correlation is shown in Pearson's correlation coefficients (r). Specific slices are outlined by a black box and enlarged in the following section for a clearer comparison. High correlation to the global signal is observed in an anterior medial part of the brain across all anesthetic conditions and bilaterally under isoflurane and isodex. Overall correlation to the non-brain tissue signal is much lower. (B) The enlarged slices that were highlighted in the previous section, show a clearer comparison between

correlation to the global signal (top row) and to the tissue signal (bottom row). (C) Voxel-wise correlation to the tissue signal with the color bar adjusted so that spatial differences can be observed. The same slices outlined in (A) are highlighted and enlarged in (D) where no spatial specificity in correlation to the tissue signal can be observed.

2.3.3 *DMN Relationship to The Global Signal*

To assess whether the regions highlighted in the voxel-wise correlation analysis could be considered part of the DMN, select DMN regions were extracted from the SIGMA-Wistar anatomical atlas. The regions included were the primary cingulate cortex (CG1), the secondary cingulate cortex (CG2), the posterior parietal cortex (PPC; an average of the atlas' parietal cortex postero caudal, dorsal, and rostral parts), the prelimbic cortex (PrL), the orbital cortex (Orb; an average of the atlas' orbitofrontal region and dorso lateral orbital cortex), the retrosplenial cortex (RSC; an average of the atlas' retrosplenial system), and cornu ammonis 1 of the hippocampus (CA1). The correlation values of each region to the global signal were extracted for each group (Figure 2.7A). The corpus callosum was included as a comparative white matter region given its proximity to some of the regions with high correlation. Regions in dexmedetomidine scans generally had lower levels of correlation than isoflurane and isodex scans reflecting what is displayed in Figure 2.6. Across all anesthetics, the secondary cingulate region shows a higher correlation to the global signal than other regions. The corpus callosum shows consistent levels of correlation across anesthetics that are on par with some DMN regions, and reliably lower than others like the cingulate cortex. Functional connectivity within the DMN was also investigated before and after global signal regression (Figure 2.7B). The same defined DMN regions used previously were also used for this analysis. As a measure of network

strength, the sum of the absolute value of all correlation values within the functional connectivity matrix was calculated before and after global signal regression. A negative difference in network strength for all anesthetic conditions showed that DMN strength decreased after global signal regression (isoflurane: $\Delta = -10.6192$; dexmedetomidine: $\Delta = -7.8689$; isodex: $\Delta = -9.2165$). A paired t-test showed that the regression of the global signal resulted in a statistically significant change in connectivity to all regions (for CG1, CG2, PPC, PrL, Orb, RSC, CA1, respectively, isoflurane: $p = 0.0022, 0.0029, 0.0043, 0.0027, 0.0023, 0.0013, 0.0048$; dexmedetomidine: $p = 0.0026, 0.0040, 0.0017, 0.0023, 0.0021, 0.0018, 0.0039$; isodex: $p = 0.0021, 0.0028, 0.0028, 0.0019, 0.0036, 0.0027, 0.0047$).

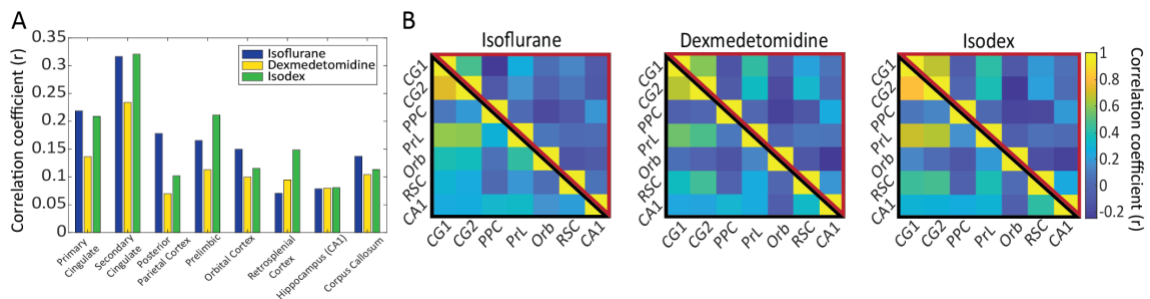


Figure 2.7 Default Mode Network (DMN) Regional Relationship to the Global Signal. The SIGMA-Wistar anatomical atlas was inversely registered with the EPI scans and select rat DMN regions as defined by Lu et al., 2012, as well as the corpus callosum, were extracted and analyzed. (A) The correlation values of each region to the global signal. Regions included: primary cingulate cortex (CG1), secondary cingulate cortex (CG2), the posterior parietal cortex (PPC), prefrontal cortex (PrL), orbital cortex (Orb), the retrosplenial cortex (RSC), and cornu ammonis 1 of the hippocampus (CA1). The corpus callosum was included as a comparative white matter region. The secondary cingulate cortex consistently shows the highest correlation to the global signal across anesthetics. (B) Functional connectivity matrix of the DMN before global signal regression (lower black triangle) and after global signal regression (upper red triangle). In each anesthetic group, functional connectivity within the DMN decreases after global signal regression

(isoflurane: $\Delta = -10.6192$; dexmedetomidine: $\Delta = -7.8689$; isodex: $\Delta = -9.2165$), indicating that the network's activity is notably represented in the global signal.

2.3.4 CAPs Results

To further emphasize the spatial differences between the global signal and the tissue signal, we performed a co-activation pattern (CAP) analysis (Figure 2.8). In this case, the two "ROIs" used to calculate the CAPs were the global signal and the tissue signal. Unsurprisingly, the global signal CAPs show high activation from similar brain regions that showed high correlation to the global signal in the voxel-wise analysis (Figure 2.7). In the isoflurane scans, the global signal CAP displays high activation bilaterally throughout cortex, and in some subcortical structures, as well as medially. The dexmedetomidine scans show lower levels of activation in the global signal CAP when compared to the other two conditions, however, higher levels of activation are observed both medially and bilaterally in cortex. The global signal CAP from the isodex scans shows high activation in medial cortex as well as bilaterally in anterior regions of cortex. In comparison, the tissue signal CAPs across all anesthetic conditions display much lower activation overall and little to no detectable spatial specificity.

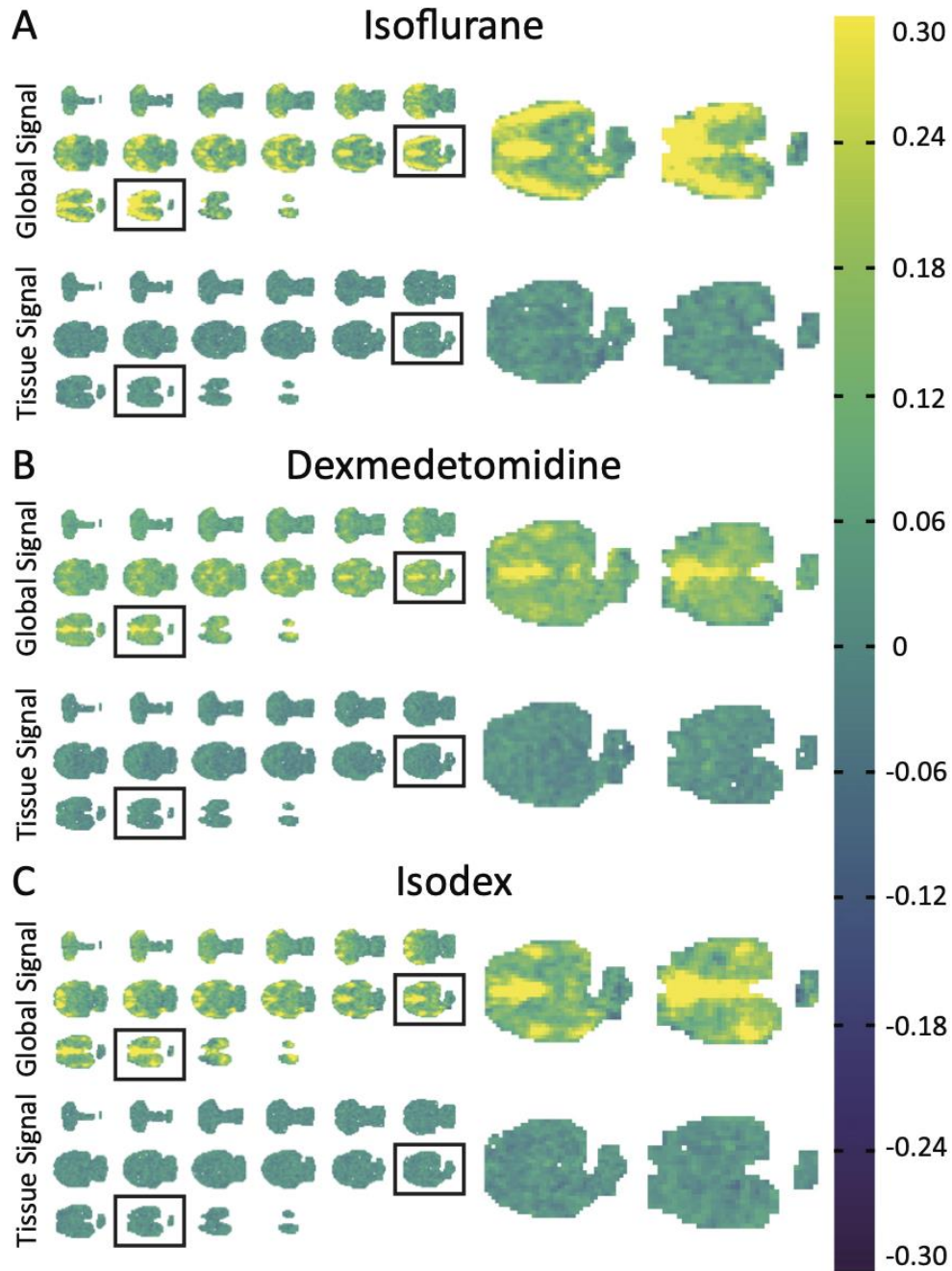


Figure 2.8 Z-scored Co-Activation Patterns (CAPs) to the Global Signal and the Non-Brain Tissue Signal. The average CAPs for scans acquired under isoflurane (A), dexmedetomidine (B), and isodex (C) when the global signal and the tissue signal were used as regions of interest. Figure displays z-scored activation level. The global signal CAP showed clear high activation in certain areas of the brain across all anesthetic conditions. These brain regions are very similar to those that showed high correlation to the global signal in the correlation analysis shown in Figure 4. In contrast, the non-brain tissue signal

CAP displays overall lower activation throughout the brain and undetectable spatial specificity.

2.4 Discussion

The use of global signal regression in preprocessing for rs-fMRI remains controversial. While the global signal captures widespread fluctuations related to motion and physiological cycles (Birn et al., 2006; Parkes et al., 2018; Satterthwaite et al., 2012; Wise et al., 2004; Yan et al., 2013), spatially-extended patterns of neural activity are also included (Ciric et al., 2017; Fox et al., 2009; T. T. Liu et al., 2017; Murphy & Fox, 2017; Saad et al., 2012). In an animal model where both motion and physiological noise are minimal, we have shown differences in spatial and spectral distribution between the global signal and a comparable noise signal that are similar under multiple anesthetic conditions. This work provides strong evidence that much of the global signal may arise from neural sources, particularly in default mode areas such as the cingulate areas, in this well-controlled model.

2.4.1 Differences in Power Distribution

PSD estimates of both the global signal and the tissue signal show distinct differences between the two signals across the different anesthetics. The most notable difference being that the tissue signals show a higher fractional power amplitude in the low frequency range than the global signals, as indicated by their fALFF values. This is interesting considering that a higher fALFF value is often considered a proxy for increased

neural activity (Zou et al., 2008). A low frequency peak is shown in the global signal power spectra which is assumed to reflect spontaneous brain activity. However, it is more difficult to identify the source of the similar low frequency power increase in the tissue signal since fALFF is typically compared within brain regions and is not examined outside of the brain. Therefore, there is little context for the relatively high values in the muscle tissue where no neurovascular coupling is present. Discerning the origin of these high fALFF values would be an interesting direction for future exploration.

Another important thing to note is that while the difference between the global signal and the tissue signal is consistent across anesthetics, the PSDs themselves are different for each anesthetic. This is not surprising since it is well known that vasculature and cerebral blood flow are affected differently by anesthetics (Slupe & Kirsch, 2018). The mechanistic differences between isoflurane and dexmedetomidine (e.g., vasodilation and vasoconstriction, respectively) could, in part, be responsible for these differences. Additionally, certain dissimilarities between groups, for example, the second peak in the non-brain tissue signal under isodex, could be attributed to vasomotion. A previous paper by Magnuson et al. looked at the time-dependent effects of both isoflurane and dexmedetomidine and found power spectral (among other) differences that occurred not only based on the anesthetic used but also on the duration of time under the anesthetics (Magnuson et al., 2014). These insights show that the power of brain activity can vary quite a bit under the use of anesthetics based on a variety of factors.

The areas of localized power in this study were similar to those that showed high correlation to the global signal (Figure 2.2 & Figure 2.6). However, the areas that show high power in the rats, presumably reflecting areas with high neural or metabolic activity,

also show similarity to the brain areas that show high correlation to the global signal in humans, namely the posterior midline (Billings & Keilholz, 2018; Power et al., 2017).

2.4.2 *DMN Contribution to The Global Signal*

The correlation to the global signal and its spatial distribution of power appeared to be highly localized along the midline of the brain, regardless of the anesthetic used (Figure 2.6). No such spatial specificity was observed when correlating voxel timecourses to the tissue signal. Upon further evaluation of these brain areas, we found that they showed striking resemblance to structures that have been identified to form the default mode network (DMN) in rats (Liang et al., 2012; Lu et al., 2012; Upadhyay et al., 2011). Consequently, we used a registered atlas to further investigate DMN specific regions and found that cingulate cortex showed higher correlation to the global signal than other DMN regions and a close white matter structure (Figure 2.7A). When looking at the comparison of DMN structures to the corpus callosum, it is important to note that the corpus callosum displayed correlation values that were on par with some DMN regions. This could be due to its size and potential grey matter contamination; however, this also demonstrates the fact that the global signal by nature captures signal from many different structures. While not all of those signals may be of interest, the combination of those signals with notable contribution from grey matter structures begs careful consideration of how the global signal is utilized. We also showed that functional connectivity within the DMN decreased after global signal regression (Figure 2.7B), implying that this network's activity is notably represented in the global signal.

In humans, areas of high correlation to the global signal are most notable along the posterior midline and in the occipital cortex, with relatively low correlation in frontal cortex (Billings & Keilholz, 2018; Power et al., 2017). The reason behind these regional differences between rat and human studies could be largely due to anatomical and functional differences in brain organization across species (Xu et al., 2022). For example, when considering the midline, higher correlation in humans was observed in posterior regions, whereas in rats, higher correlation is observed along the anterior midline, more specifically, the cingulate cortex. This is in accordance with defined regions that make up that DMN for each species; the precuneus and posterior cingulate in humans (Thomas Yeo et al., 2011) and the cingulate and retrosplenial cortices in rats (Lu et al., 2012). Additionally, the human data contained notably more signal contribution from head motion and respiratory patterns (Power et al., 2017), factors that were largely accounted for in our rat study. *Power et al.*, highlight the variability of spatial distribution of the global signal across individuals, scanning protocol used, and hardware artifacts (Power et al., 2017). In contrast, the current study saw similar results on an individual level (Anumba et al., 2023), possibly due to the strict control of motion and respiration.

A previous study done in humans that used CAP analysis based on peaks of the global signal identified high co-activation among sensory cortices in the global signal CAP (X. Liu, Zhang, et al., 2018). While we did not find the same high contribution from sensory cortices in our rat dataset, a substantial cause of this would be the use of anesthesia with our rats, whereas the HCP data used in the cited study was acquired from awake humans.

When comparing to the non-brain tissue signal, in both the static and dynamic methods, the tissue signal showed no resemblance to the global signal results with little to

no spatial coherence and very low levels of correlation and activation. These differences emphasize the different information contained in these two signals and support the idea that the global signal may contain a sizable neural component that is not present in the tissue signal.

The findings of this paper indicate that DMN brain areas may contribute a disproportionate amount of activity to the global signal in rats. This is significant as preprocessing steps that eliminate the global signal in rodent studies are most likely removing potentially relevant information from large-scale brain activity, including contributions from large neural networks like the DMN and potentially whole-brain dynamics. However, the contribution of noise to the global signal could be stronger in freely breathing and awake animals.

2.4.3 Effects of Anesthesia on Results

To account for differences in brain signal that arise due to the use of an anesthetic (X. Liu et al., 2013; Masamoto et al., 2009; Masamoto & Kanno, 2012), we carried out our analysis in data collected under three different anesthetic protocols: isoflurane, dexmedetomidine, and isodex. The anesthetic effects of vasodilator isoflurane are mediated by a complex interaction with GABAergic neurotransmission (Ferron et al., 2009) through a completely different mechanism than the sedative effects of vasoconstrictor dexmedetomidine, which are mediated by interaction with alpha2-adrenergic receptors (Ganjoo et al., 1998). Deeper levels of anesthesia have been shown to cause less spatially-specific functional connectivity across the brain (X. Liu et al., 2013). Consequently, the

anesthetic levels used in this study were kept relatively light and we continued to see spatially specific correlation to the global signal across all anesthetic conditions.

One advantage of performing a study in humans or awake animals would be the absence of such effects, although this absence also comes with the inclusion of more inherent noise from motion and physiological cycles. This tradeoff however, does not negate the utility of using anesthetized rodents as the paralyzed, mechanically-ventilated rat presents a unique situation in which to study neural aspects of the rs-fMRI signal (Xu et al., 2022). These findings, in addition to the application of rodent disease models and genetic manipulation tools, are invaluable to our understanding of human brain function.

As discussed earlier, when looking at the PSD estimates for each signal, there were notable differences across the anesthetics that could be attributed to a variety of factors. However, despite the mechanistic differences across these anesthetics, the spatial correlation results found were consistent regardless of the type of anesthetic used. This is especially apparent in Figure 2.6, Figure 2.7, and Figure 2.8, where similar brain areas are shown to have higher static and dynamic correlation to the global signal under isoflurane, dexmedetomidine, and isodex. That being said, it should be noted that different anesthetics showed varying levels of correlation within these structures. For example, isoflurane and isodex consistently show a stronger and more extensive correlation to the global signal than dexmedetomidine (Figure 2.6, Figure 2.7, and Figure 2.8). This difference is something to be considered when choosing an anesthetic for rodent studies and how said anesthetic could affect the global signal's involvement with the data. Despite the anticipated anesthetic-induced effects on brain activity, the results of the present study demonstrate consistent non-random correlation to global brain signal with a similar spatial distribution across

anesthetic conditions, indicating that these results are unlikely to be artifacts of the anesthesia.

2.4.4 *Limitations*

One limitation of this study is the fact that the timing of introduction for the anesthetics varied from scan to scan, due to differences in time required for setup and maintenance of physiological conditions. Despite this difference, similar results were found across scans when these analyses were done on an individual basis ([Anumba et al., 2023](#)). Because we were primarily interested in the spatial differences between the tissue and global signal, we averaged all timepoints corresponding to peak activity to obtain a single CAP for each signal, rather than cluster the results into multiple CAPs. Further insight into which areas of the brain contribute to the global signal at different timepoints might be obtained with the clustering approach. Moreover, CAP analysis is only one tool available for time-resolved analysis of resting state fMRI, and other methods such as sliding window correlation, signal complexity, or spatiotemporal patterns might provide further insight into the characteristics of the global signal (S. Keilholz et al., 2020; S. D. Keilholz et al., 2013; Majeed et al., 2011).

2.5 **Conclusion**

Our findings provide strong evidence that the global signal and the acquired non-brain tissue signal contain different information and that the information contained in the global

signal is likely to include substantial contributions related to neural activity. The global signal is often attributed to large-scale contributions from motion and noise, both of which were considerably reduced in this study. As a result, we believe it is reasonable to suggest that a substantial amount of the effects we are seeing stem from neural origins. The relative paucity of noise related to motion and physiological cycles in the global signal suggests that for studies in anesthetized rodents, global signal regression is likely to do more harm than good, attenuating information about neural activity while making only modest reductions in other noise. For humans, where motion and physiological noise make greater contributions, the implications of the study are less clear, but at a minimum this work should motivate a cautious approach to the removal of the global signal, and an additional level of care in the interpretation of the results.

CHAPTER 3. INVESTIGATING THE EFFECTS OF LC STIMULATION ON THE GLOBAL SIGNAL AND QPPS

Motivation: Patterns of whole-brain dynamic activity in rs-fMRI, such as the BOLD global signal and QPPs, have been known to change with different brain states, arousal in particular. The LC is not only known to be involved in arousal but also has extensive projections throughout the brain, giving it neuromodulatory influence over the coordinated activity of structurally separated regions. This study sought to investigate the role that LC activity plays in the BOLD global signal and QPPs in rats.

Methods: Optogenetic-fMRI was used to stimulate the LC at different frequencies while obtaining whole-brain imaging data. Analysis of this data utilized Pearson's linear correlation to measure functional connectivity and establish voxel-wise correlation to the global signal, a power spectral density estimate to assess frequency involvement in the global signal, a pattern-detection algorithm to identify QPPs, and complex principal component analysis (CPCA) as an additional approach to investigate these spatiotemporal patterns.

Results: We report spatially specific changes in global signal distribution as a result of tonic LC stimulation (Section 3.3.3) as well as regional changes QPP activity at 5 Hz tonic and 15 Hz phasic stimulation (Section 3.3.5). We also found similar results to those found in humans regarding CPCA components and discovered differences in these components when comparing WT animals to an Alzheimer's model (Section 3.3.6).

Conclusion: These results show that the effects of LC activity on the BOLD global signal and QPPs in rats may be small and regionally specific, as opposed to widespread and globally acting. This study provides additional information into our understanding of how global spatiotemporal dynamics are affected by neuromodulation and changing brain states.

3.1 Background

Functional MRI (fMRI) is increasingly used to non-invasively study changes in brain activity. In particular, the study of dynamically changing resting-state fMRI (rs-fMRI) signals that span multiple brain regions provides an opportunity to better understand the intrinsic contexts of large-scale communication across the brain. One such signal that has been the source of much debate over the years is the blood oxygenated level dependent (BOLD) global signal, often measured to be the average of all brain activity over the course of a scan. Often used as a nuisance regressor, the global signal can be regressed out of a scan to successfully reduce the effects of widespread noise in rs-fMRI data ([Birn et al., 2006](#); [Parkes et al., 2018](#); [Satterthwaite et al., 2012](#); [Yan et al., 2013](#)); although the existence of resting state networks and large-scale patterns of activity have caused many to pause at the removal of the global signal from fMRI datasets ([Ciric et al., 2017](#); [Fox et al., 2009](#); [Liu et al., 2017](#); [Murphy & Fox, 2017](#); [Saad et al., 2012](#)). Like the global signal, quasi-periodic patterns (QPPs) are comprised of the simultaneous activity of multiple brain structures that are defined by varying networks and functions. The term QPP is used to describe the semi-regular waves of alternating activity between different structures and

networks that have been observed across species. QPPs are most often characterized as propagating wave-like patterns of anticorrelation between the default mode network (DMN) and task positive network (TPN) in humans ([Majeed et al., 2011](#)) and between the rodent DMN and lateral cortical network (LCN), which is believed to exhibit similar activity to the human TPN, in rodents ([Belloy et al., 2018](#)). They are also thought to organize functional connectivity across the brain and contribute to the global signal ([Abbas et al., 2019](#); [Belloy et al., 2018](#); [Yousefi et al., 2018](#)). Despite most often being measured during resting state, both of these signals have been shown to exhibit notable changes during arousal and in correspondence with vigilance-related measures. The global signal is well known to be inversely correlated with various measures of vigilance and arousal across different species. In humans, an EEG measurement of vigilance was found to be inversely correlated with the amplitude of the global signal ([Wong et al., 2013, 2016](#)). A negative correlation to the global signal was also found with a local field potential (LFP) measure of arousal in non-human primates ([Chang et al., 2016](#)), and a study in mice used pupil diameter as a proxy for arousal and showed that changes in pupil diameter were anticorrelated to changes in global hemodynamics ([Pisauro et al., 2016](#)). Additionally, the introduction of caffeine as a measure of vigilance has been shown to increase anticorrelation between the DMN and the TPN ([Wong et al., 2012](#)), and a wave-like propagation of phase shifts was reported to occur as a result of infra-slow arousal-related activity ([Raut et al., 2021](#)). These relationships present a need to better understand the genesis of and underlying mechanisms behind these signals, and consequently their explicit association with arousal states.

In recent years, the locus coeruleus–norepinephrine (LC-NE) neuromodulatory system has gained a lot of attention for the potential role that it plays in these spatiotemporal dynamic signals. As the primary brainstem nucleus for NE synthesis and release throughout the central nervous system, the vast projections of the LC have strong potential to influence whole-brain levels of activity. Of interest to fMRI in particular, it has also been shown that LC-NE vascular innervation helps to optimize neurovascular coupling leading to a potential increase in sensitivity of the BOLD signal (Bekar et al., 2012). Among being known to play a role in cognition and sleep, the LC is perhaps most known for its role in attention and arousal (Aston-Jones & Cohen, 2005; Benarroch, 2018), providing further cause to investigate its involvement in the BOLD global signal and QPPs. In fact, evidence shows that the activity of brainstem nuclei may play a significant role in large-scale spatiotemporal signals (van den Brink et al., 2019). Turchi et al., showed that inhibition of the basal forebrain decreased the amplitude of global signal fluctuations (Turchi et al., 2018). However, these effects were more pronounced during less alert behavioral states, indicating a connection of this effect to arousal and potentially the activity of other brainstem nuclei. The origin of QPPs has been speculated to arise from the activity of neuromodulatory brainstem nuclei (Abbas et al., 2019) and preliminary work has shown that extreme interventions of NE levels drastically reduce the detection of QPPs (Abbas et al., 2018). The cholinergic and noradrenergic systems have been hypothesized to work in an almost opposing manner in their influence over widespread cognitive processing, with the LC-NE system in particular believed to coordinate and integrate activity across structurally segregated regions (Shine, 2019). LC activation has further been shown to

effect large-scale measures of activity by strengthening brain-wide connectivity and even modulating nodes of the DMN ([Oyarzabal et al., 2021](#); [Zerbi et al., 2019](#)).

In this study, we aimed to further investigate the role played by the LC-NE system in the composition of the BOLD global signal and QPPs through the utilization of optogenetic-fMRI. In contrast to the use of chemogenetics, optogenetics provides us with the additional control needed to not only stimulate the LC, but to selectively stimulate it at different frequencies. We used optogenetic-fMRI in rats to investigate distinct characteristics of the BOLD global signal and QPPs during low tonic (2 Hz), high tonic (5 Hz), and phasic burst (15 Hz phasic) stimulation of the LC. For certain analyses we also investigated the effects of Alzheimer's disease (AD) on whole-brain dynamic signals using the AD rat model TgF344-AD ([Cohen et al., 2013](#)). The LC itself has been shown to be the first brain structure to exhibit AD pathology and has projections to many regions that are prone to severe atrophy in AD such as the hippocampus and many cortical structures ([Braak et al., 2011](#); [Braak & Del Tredici, 2011](#); [Elobeid et al., 2012](#); [Grudzien et al., 2007](#)). The TgF344-AD rat model carries mutant human amyloid precursor protein (APP_{sw}) and presenilin-1 (PS1 Δ E9) genes and has been shown to develop tau pathology in the LC before the entorhinal cortex and hippocampus ([Cohen et al., 2013](#); [Rorabaugh et al., 2017](#)). In executing certain analyses in an AD model, we hoped to gain a better understanding of how some of these whole-brain metrics are affected by widespread degeneration and dysfunction as caused by Alzheimer's disease. We report spatially specific changes in global signal distribution under tonic LC stimulation as well as regional changes in QPP involvement under 5 Hz tonic and 15 Hz phasic stimulation. We also show differences in functional connectivity as a result of AD, as well as age-specific AD effects in the primary

principal components as captured by complex principal component analysis (CPCA). These results show that the neuromodulatory effects of the LC-NE system on large-scale spatiotemporal patterns may be small in scale and more regionally specific than initially thought.

3.2 Materials and Methods

An overview of the methods involved in the optogenetic-fMRI experimentation from initial surgery to data analysis can be seen in Figure 3.1.

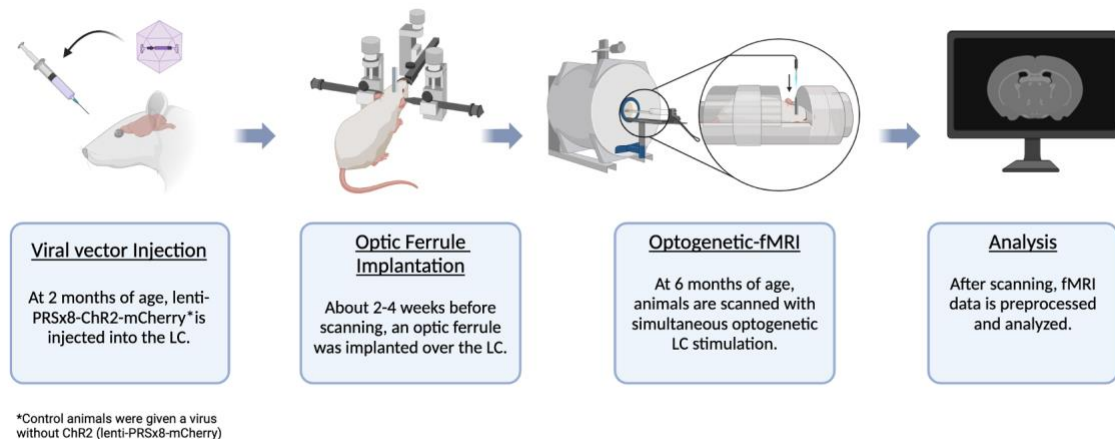


Figure 3.1 Methods timeline of optogenetic-fMRI experiments. When rats were 2-months old, they were given bilateral injections to the LC with a lentivirus containing the noradrenergic promotor PRSx8, the mCherry fluorescent protein, and channelrhodopsin-2 if they were not control animals. Two to four weeks before scanning took place, animals were implanted unilaterally with an optic ferrule over the LC. At 6 months of age, animals underwent an fMRI scanning session with varying levels of simultaneous optogenetic LC stimulation. After scanning, all fMRI data was preprocessed and analyzed.

3.2.1 *Animal Preparation*

Two separate cohorts of different ages, 6-month-old and 15-month-old, of male and female TgF344-AD Fischer rats that were heterozygous for the APP^{sw}/PS1^{deltae9} transgene in addition to their wildtype (WT) littermates were used in this study. For analyses that showcase the effects of LC stimulation only 6-month-old WT animals were included (For mCherry control groups: n = 9, 8, 7, 8 for baseline, 2 Hz, 5 Hz, and 15 Hz phasic groups, respectively; For ChR2 groups: n = 7, 4, 5, 6 for baseline, 2 Hz, 5 Hz, and 15 Hz phasic groups, respectively). For analyses that include AD rats, 6-month and 15-month-old mCherry control groups of WT and AD were included (6-month WT mCherry control groups reported above; For 15-month WT mCherry control groups: n = 10, 6, 9, 9 for baseline, 2 Hz, 5 Hz, and 15 Hz phasic groups, respectively; For 6-month AD mCherry control groups: n = 11, 9, 10, 9 for baseline, 2 Hz, 5 Hz, and 15 Hz phasic groups, respectively; For 15-month AD mCherry control groups: n = 12, 10, 10, 9 for baseline, 2 Hz, 5 Hz, and 15 Hz phasic groups, respectively). For a breakdown of how many animals and scans were included for each group refer to Table 3.1. Expression of both virus and cFos in the LC were verified post-mortem and ChR2 animals that lacked expression were either eliminated from the study or moved to the control group. Difference in scan number across groups can also be explained by the elimination of scans with significant artifacts as well as by the study design in which each session contained more scans of certain conditions (e.g., each session included two baseline and 15 Hz phasic scans) (Figure 3.2). All analyses were also performed on 6-month AD ChR2 animals, 15-month WT ChR2 animals, and 15-month AD ChR2 animals, however these results are not included in the

results section due to small group sizes. Results for these groups as well as their group sizes can be found in APPENDIX A. All rats were bred in-house, kept on a 12 hr light/dark cycle (lights on at 7:00 am), and provided access to food and water *ad libitum* throughout the experimental period. Rats were group-housed in groups of 2-3 animals up until implantation of the optic ferrule, after which they were singly housed until they underwent scanning in the MRI machine (between 2-4 weeks). Experimental groups were comprised of animals of both sexes as past work has shown a lack of significant sex-based differences in this specific model (Cohen et al., 2013), and each rat was randomly assigned to an experimental group. For a breakdown of the sex makeup of each group refer to Appendix Table 2. All protocols used in this study were approved by the Institutional Animal Care and Use Committee (IACUC) at Emory University and all procedures were performed in accordance with the IACUC protocols.

Table 3.1 Animal group sizes.

	6-month WT mCherry Animals (Scans)	6-month WT ChR2 Animals (Scans)	6-month AD mCherry Animals (Scans)	15-month WT mCherry Animals (Scans)	15-month AD mCherry* Animals (Scans)
Baseline	9 (15)	7 (13)	11 (19)	10 (18)	12 (18)
2 Hz	8 (8)	4 (4)	9 (11)	6 (6)	10 (11)
5 Hz	7 (7)	5 (5)	10 (13)	9 (10)	10 (12)

15 Hz Phasic	8 (12)	6 (10)	9 (13)	9 (14)	9 (15)
---------------------	--------	--------	--------	--------	--------

*The 15-month AD mCherry control group included sessions for some rats that had fewer timepoints than the others and consequently (due to the necessity of scan concatenation), scans from these animals were removed for CPCA, network-level functional connectivity, and QPP analysis. The adjusted group sizes of the 15-month AD mCherry group for these analyses were 9 (14), 8 (9), 8 (9), and 8 (13) for baseline, 2 Hz, 5 Hz, and 15 Hz phasic scans, respectively.

3.2.2 *Surgery and Pupillometry*

Stereotaxic surgery was performed on all rats at 2-months of age. Rats were initially put under anesthesia with 5% isoflurane. Isoflurane was then lowered to 2% for the remainder of the surgery and rats were given ketoprofen (5 mg/kg, s.c.) directly following incision. To avoid contact with the sagittal sinus a 15-degree head tilt was utilized and bilateral injections (1.3 ul/hemisphere) of lentivirus expressing either channelrhodopsin-2 (ChR2)-mCherry or mCherry alone were administered to the rats to target the LC (AP: -3.8 mm from lambda, ML: +/- 1.2 mm, DV: 7.0 mm from skull surface). Both ChR2 and control animals included the fluorescent protein mCherry in order to verify viral expression in post-experimental imaging. After the infusion, the needle was left for 5 minutes after which it was moved 1 mm dorsally and 2 minutes were allotted to permit appropriate viral diffusion at the injection site. In order to limit viral expression to noradrenergic LC neurons, PRSx8 was utilized as a noradrenergic-specific promotor ([Hwang et al., 2001](#)).

Between 2–4 weeks before undergoing MRI scanning rats were implanted with a fiber optic ferrule (FG200UCC, 200 um, 0.22 NA, 7.5 mm length; Thorlabs) above the LC to enable delivery of optogenetic stimulation. The hemisphere in which the LC was

targeted was randomized for each rat so that stimulation of both the left and right LC were incorporated into group analysis. The aforementioned surgical protocol was observed with optic ferrules being implanted dorsal to the LC (AP: -3.8 mm from lambda, ML: +/-1.2 mm, DV: 6.5-6.8 mm from skull surface). Afterwards, the skull was implanted with three MRI-compatible screws.

Stimulation of the LC has been shown to result in pupil dilation, providing a useful measure to verify successful viral expression and optic ferrule targeting. We performed this verification via pupillometry following previously published setup and procedure protocols ([Privitera et al., 2020](#); [Zerbi et al., 2019](#)). Our setup involved the use of a Raspberry Pi NoIR Camera Module V2 night vision camera, an infrared light source, and a Raspberry Pi 4 Model B (CanaKit). During optic ferrule implantation, while the rats were still under anesthesia, 90 seconds of pupil recordings were taken of the eye ipsilateral to the hemisphere of the stimulated LC. The recordings were comprised of 30 seconds of baseline (no stimulation) followed by 30 seconds of LC stimulation via constant laser exposure and ended with another 30 seconds of post-stimulation baseline footage (Figure 3.3). After successful viral expression and LC stimulation had been verified, dental cement was used to fix the optic ferrules in place. Rats were then given approximately 2-4 weeks to recover from surgery before they underwent MRI scanning.

3.2.3 fMRI Data Acquisition

On the day of MRI scanning, rats were initially inducted under anesthesia for 5 minutes at 5% isoflurane in combination with a 2:3 ratio of O₂ and medical grade air. After

initial induction with isoflurane, animals were maintained under 2-3% isoflurane for the remainder of handling and cradle preparations. Rats were intubated and administered the paralytic pancuronium dibromide (1.5 mg/kg/hr, s.c.) (Selleck) immediately after intubation. Through the tracheal tube, breathing of the rats was maintained at 1.6 Hz by use of a ventilator. Animals were then placed in a custom-made MRI cradle where a custom-made transmit-receiver surface coil was placed over the brain and the optic fiber patch cord was connected to the optic ferrule. Animals were then head-fixed with ear bars and their teeth secured in a bite bar to limit head motion during scanning. To prevent the escape of light during stimulation, a black marker was used to 'blackout' the headcaps and tape was placed over the connection between the optic fiber and the optic ferrule implant. Eye ointment was placed over both eyes prior to scanning and isoflurane was reduced to 1.3% and maintained at this level for the rest of the scanning session. Heart rate and blood oxygen levels of the animals were monitored throughout the scanning session using a pulse oximeter that was connected to the hindpaw of the animal. Temperature of the rat during scanning was maintained at 37 ± 0.5 °C using a heated water bath system.

All fMRI scans were acquired using a 9.4T Bruker Biospec MRI scanner with a 20 cm horizontal bore. Scans were 10 minutes in length and were gradient-echo echo-planar imaging (EPI) with partial Fourier encoding with a factor of 1.4. The following parameters were used to acquire the images: isotropic voxel size = 0.5 mm^3 , matrix size = 70×70 , slice number = 24, TE = 15 ms, TR = 1250 ms, flip angle = 90° , bandwidth = 216.45 kHz. All scans were phase-locked so that each acquisition was set to occur at a multiple of the animal's respiratory rate. In this study, the repetition time of 1250 ms (0.8 Hz) was employed to acquire images at the frequency of every other breath of the 1.6 Hz respiration

rate. This practice was adopted to ensure that each image slice was obtained at the same point in the animal's respiratory cycle and therefore limit motion-induced artifacts as a result of chest cavity movements during respiration (Pan et al., 2020). A single volume reversed blip EPI image with the same parameters was acquired before each 10-minute scan and used for topup correction (Andersson et al., 2003; Smith et al., 2004). Saturation bands were used with all functional EPI scans to minimize signal from outside of the brain, additionally, each scan was preceded by 10 dummy scans for system calibration purposes.

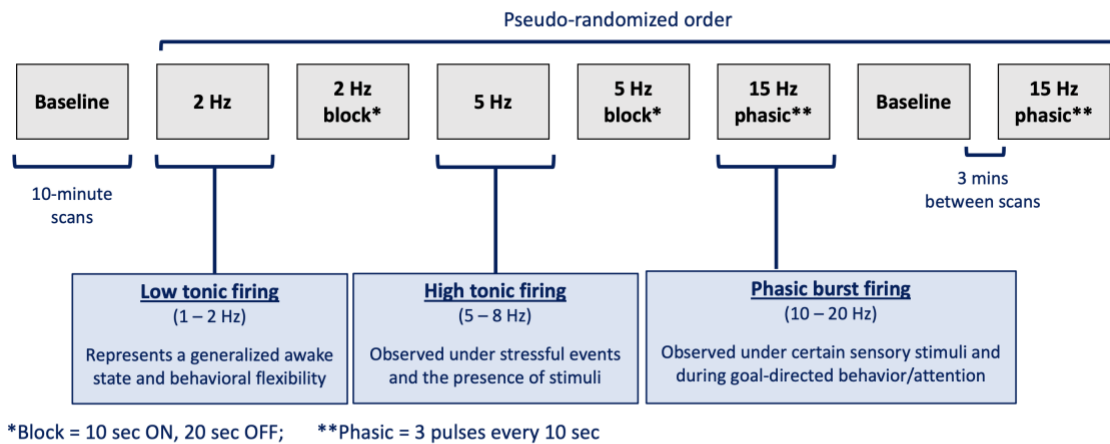


Figure 3.2 Scanning session timeline. All scanning sessions consisted of eight 10-minute fMRI scans with three minutes between scans. Stimulation of the LC was done at 2 Hz, 5 Hz, and 15 Hz phasic bursts to replicate the common modes of firing displayed by the LC. Each session started with a baseline scan (no stimulation) that was followed by the remaining seven scans in a pseudo-randomized order. The block stimulation scans were not used in this study.

Four different levels of LC stimulation were incorporated into this study: baseline (i.e., no stimulation), 2 Hz stimulation, 5 Hz stimulation, and a 15 Hz phasic stimulation (comprised of 3 pulses of stimulation at 15 Hz every 10 seconds). These frequencies were chosen to mimic the distinct firing modes that have been observed to occur naturally in the LC. The LC is characterized by three distinct firing modes: low tonic, high tonic, and phasic burst firing. Low tonic firing (1–2 Hz) is observed under a generalized awake state, high tonic firing (3–8 Hz) is observed in the presence of stressful events and stimuli, and phasic burst firing (10–20 Hz phasic bursts) helps drive goal-directed behavior and focused attention ([Berridge & Waterhouse, 2003](#); [Carter et al., 2010](#); [Chalermpananupap et al., 2017](#); [McCall et al., 2015](#)). Each scanning session consisted of a total of eight scans that were presented in a pseudo-randomized order: two baseline scans and two scans each at 2 Hz, 5 Hz, and 15 Hz phasic stimulation (Figure 3.2). For the scans in which 2 Hz and 5 Hz stimulation was presented, one of the two scans was acquired with constant stimulation at that frequency for the entirety of the 10 minutes, while a block design of stimulation (10 seconds of stimulation and 20 seconds of rest) was employed for the other scan. Only the constant stimulation scans are included in this study. Each session started with a baseline scan, a 5 Hz constant scan was employed as the fourth scan and followed by the second baseline scan; the placement of all other stimulation levels was randomized for each session. Placement of the 5 Hz constant stimulation scan was maintained to ensure optimal expression of cFos during staining approximately 90 minutes later ([Tillage et al., 2020](#)). All optogenetic stimulation was done with 60mW of laser power with 10 ms-long pulses. Three minutes was allotted between scans to allow for norepinephrine levels to return to baseline post-stimulation.

3.2.4 Preprocessing

Preprocessing of fMRI data was done using the *Rodent Whole-Brain fMRI Data Processing Toolbox* (Xu et al., 2023). Through use of this toolbox, the following preprocessing steps were performed: slice time correction, motion correction, topup correction, nuisance regression (constant, linear, and quadratic trends as well as 6 motion regressors), normalization, bandpass filtering (0.01–0.1 Hz), spatial smoothing (FWHM = 0.5 mm), and registration to and seed extraction from the functional SIGMA-Wistar atlas (Barrière et al., 2019).

3.2.5 Tissue Preparation and Immunohistochemistry

After scanning was complete, the rats were removed from the ventilator and perfused immediately. Perfusion of the rats was done with 0.1 M kPBS before being followed up by 4% paraformaldehyde. After brains were extracted, they were placed in 4% paraformaldehyde and stored overnight before being moved to 30% sucrose for a minimum of 3 days before slicing. Brain slices were 30 μ m in thickness at the level of the LC and sections were mounted on Colorfrost® Plus slides (Erie Scientific) to be stained (if not stained right away, sections were stored in cryoprotectant until they were stained). As mentioned before, neutral red was used to counterstain the mounted sections for confirmation of correct placement of the optic ferrule implant.

Free floating sections at the level of the LC were washed 3 x 5 minutes in 1x PBS and then incubated for 1 hour in blocking buffer (5% normal goat serum, 3% bovine serum albumin in 0.1% PBST). After this, sections were incubated in chicken anti-tyrosine hydroxylase (TH) (1:1000;) and rabbit anti-cFos (1:3000;) for 48 hours. Sections were then washed 3 x 5 minutes in 1x PBS and incubated for 2 hours with the corresponding secondary antibodies goat anti-rabbit 488 and goat anti-chicken 633 (1:500;). Then, sections were washed again 3 x 5 minutes and mounted on slides, dried, and coverslipped.

The aforementioned sequence of scan stimulation levels was orchestrated so that the sacrifice of the animal would occur approximately 90 minutes after a scan with constant 5 Hz stimulation had been acquired. This was done in order to stain for cFos, an immediate early gene and neuronal activity marker, on a timeline that has previous been reported ([Tillage et al., 2020](#)). A Leica DM6000B epifluorescent upright microscope was used to image the sections at 10x. Using ImageJ, TH was used as a marker to manually outline the LC, a common Otsu threshold was set and despeckling was performed. Then, the number of cFos labelled cells was counted using standard criteria (pixel size: 100-infinity and circularity: 0.7-1.0). A two-way repeated measures ANOVA was used to assess differences in cFos expression across groups.

3.2.6 *Data Analysis*

3.2.6.1 Functional Connectivity

Functional connectivity was calculated by performing a Pearson's linear correlation between the timecourses of all atlas parcellations. Connectivity matrices were acquired for each scan individually and then Fisher Z-transformed prior to being averaged by group. A two-sample t-test was performed for each group between baseline and the 2 Hz, 5 Hz, and 15 Hz phasic stimulation levels at both the parcellation level and the network level (for which connectivity values within each network were averaged to represent that network). Significant effects were defined as those whose p-values were < 0.05 . A post-hoc False Discovery Rate (FDR) test was performed on the results of the t-tests to account for multiple comparisons.

3.2.6.2 Spatial Distribution of the Global Signal

In order to investigate how LC stimulation affects the spatial aspect of the global signal, the regional distribution of the global signal was assessed. The global signal was calculated by extracting all timecourses within the brain region and averaging them into a single timecourse. The global signals for each scan were then z-scored by subtracting the mean and dividing by the standard deviation. The scans and global signals for each group were concatenated and the timecourse of each voxel within the brain was correlated to the global signal via a Pearson's linear correlation. The map of correlation values of each voxel to the global signal are displayed by group. All analysis was performed in MATLAB using custom scripts.

3.2.6.3 Power Spectral Density Analysis of the Global Signal

The frequency of the global signal was observed by way of a power spectral density (PSD) analysis. PSD estimates were obtained in MATLAB using Welch's method with a Hamming window and 50% overlap. The global signals for each group were z-scored and concatenated, after which a PSD was calculated for the concatenated signals producing the group results.

3.2.6.4 QPP Analysis

QPPs were calculated using a repeated pattern detecting algorithm that was initially reported in (Majeed et al., 2011) and later modified in (Yousefi et al., 2018). This algorithm starts by taking a template, comprised of a number of images within the scan that is dictated by the user defined window length, and uses a sliding window approach to correlate this template to each timepoint of the acquired scan. A threshold is set for the correlation timecourse and at all points at which the correlation between the template and the scan is higher than the threshold, the images are taken and averaged to create a new template. This process is repeated until the template does not change after two iterations ($cc > 0.9999$). The modified pattern finding algorithm used in this study differs from that which was initially reported in that instead of this process being carried out only a certain number of times as defined by the user, the process is executed with a starting template from every scan timepoint with the best template (the one with the highest supra-threshold correlation sum) being chosen from among them. This modification results in a more robust pattern-detection method that is independent of algorithm starting point. Prior to the detection of

QPPs, the global signal was regressed from each scan as inclusion of the global signal is known to obscure the detection of network-alternating QPPs (Yousefi_et_al., 2018). For group QPP analysis, the algorithm was run on the concatenation of all scans within said group.

To assess the frequency of QPP occurrence for each group, a histogram of the final sliding template correlation (STC) timecourse for each group was created. STC values above the standard threshold of 0.2 were considered to be QPP events. To evaluate the pattern of the QPP itself, the final template provided by the algorithm was observed and compared between groups. This analysis was performed in MATLAB using custom scripts.

3.2.6.5 Complex Principal Component Analysis (CPCA)

As a way to further investigate the spatiotemporal dynamics of this dataset we performed complex principal component analysis, or CPCA. Through the application of PCA on the complex Hilbert-transformed BOLD timecourses, CPCA provides a way to assess the magnitude and phase-lag differences between the activity of different brain structures. These transformed BOLD signals contain a real part (the magnitude) and an imaginary part (the phase). Subsequently, the principal components extracted from these complex signals are also complex, allowing us to observe both the magnitude and the phase attributes of each component. CPCA was performed using a python command line script (Bolt, 2023/2023) that utilizes a randomized singular value decomposition (SVD) algorithm that was developed by Facebook (Facebookarchive/Fbpca, 2014/2024). Custom MATLAB scripts were then used to visualize and evaluate the magnitude, phase, and

incidence of the first three principal components. Incidence of a principal component at any given timepoint was defined by which of the first three components explained the most variance in the scan at that timepoint.

3.3 Results

3.3.1 *Multimodal Confirmation of Optogenetic LC Stimulation*

Taking advantage of the link between LC activity and pupil dilation, we used pupillometry to confirm accurate placement of the optic ferrule implant and expression of the virus (Figure 3.3A). This was done by recording robust dilation of the ipsilateral pupil in ChR2 expressing animals during optogenetic stimulation; stimulation-driven pupil dilation was not observed in animals expressing the mCherry control virus. Pupil dilation was quantified and compared between all mCherry and ChR2 animals (Figure 3.3B). After scanning and sacrificing the animals, optic ferrule placement was further confirmed via staining using a neutral red counterstain, immunofluorescence indicating viral expression, and staining for the immediate early gene cFos displaying activation of the LC (Figure 3.3C). For cFos staining a two-way repeated measures ANOVA revealed no effect of virus ($F(1,39) = 1.83, p = 0.18$), a main effect of hemisphere ($F(1, 39) = 29.03, p < 0.0001$), subject ($F(39, 39) = 5.83, p < 0.0001$), and a virus x hemisphere interaction ($F(1, 39) = 37.51, p < 0.0001$). Tukey's multiple comparison tests revealed significant differences between the stimulated hemisphere of mCherry and ChR2 injected animals ($p = 0.0006$) and between the stimulated and non-stimulation hemisphere in ChR2 animals ($p < 0.0001$) (Figure 3.3D). For the 15-month animals (data shown in APPENDIX A), a two-way

repeated measures ANOVA showed a main effect of virus ($F(1,32) = 6.245, p = 0.018$), of hemisphere ($F(1, 32) = 64.54, p < 0.0001$), subject ($F(32, 32) = 12.82, p < 0.0001$), and a virus x hemisphere interaction ($F(1, 32) = 82.4, p < 0.0001$). Tukey's multiple comparison tests revealed significant differences between the stimulated hemisphere of mCherry and ChR2 injected animals ($p < 0.0001$) and between the stimulated and non-stimulation hemisphere in ChR2 animals ($p < 0.0001$).

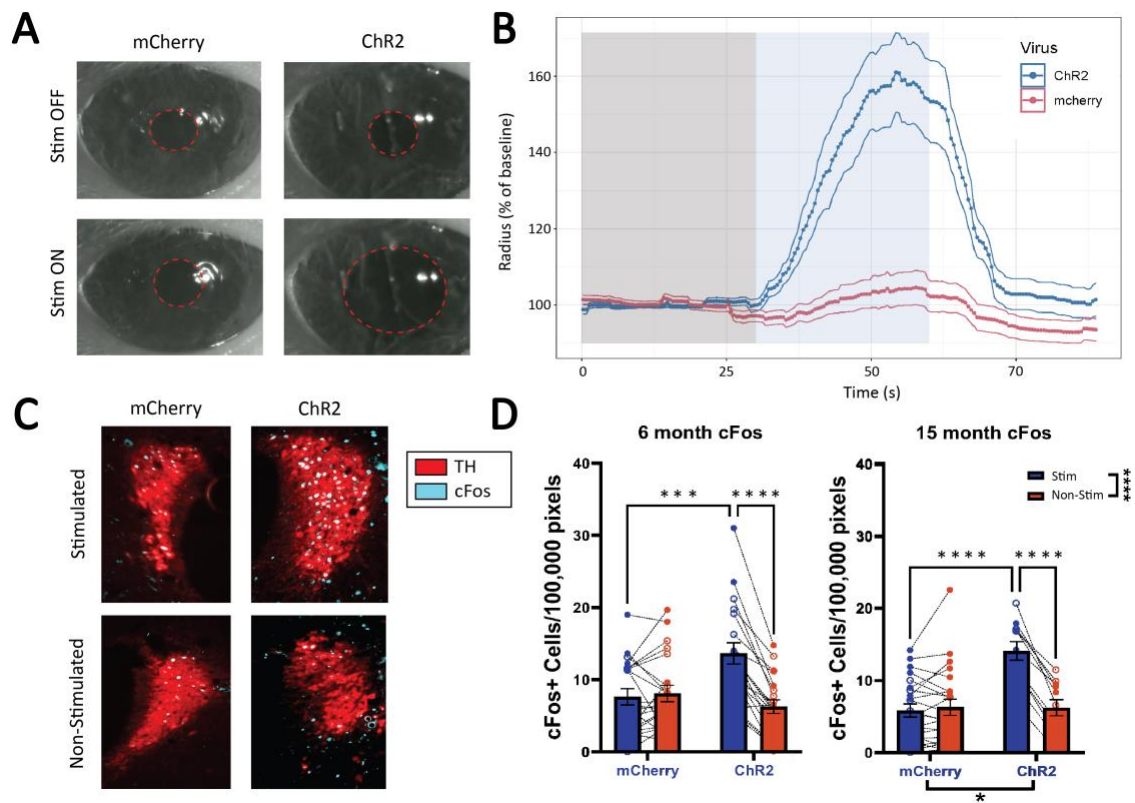


Figure 3.3 Confirmation of LC optogenetic stimulation and LC noradrenergic activity. Verification of accurate viral expression in the LC was done using pupillometry. (A) shows the visual increase in pupil diameter experienced during LC stimulation via optic fiber. (B) The change in pupil radius was quantified and compared between all mCherry animals and all ChR2 animals. (C) cFos expression was used to confirm the activity of LC neurons roughly 90 minutes after constant stimulation at 5 Hz. Shown is a representative image of an mCherry and a ChR2 animal and the differences in cFos

expression between their stimulated and non-stimulated hemispheres. (D) The cell count of neurons expressing cFos quantified for both the mCherry and ChR2 animals at 6 months and 15 months (data shown in APPENDIX A).

3.3.2 *Functional Connectivity*

In order to detect any potential whole-brain effects of LC stimulation we first looked at whole-brain functional connectivity (Figure 3.4). When comparing each stimulation level to baseline no large-scale effects on functional connectivity were observed. Smaller significant changes, however, were observed at the parcellation level for each stimulation level. Upon 2 Hz stimulation scattered changes in connectivity were primarily seen in regions in the olfactory and pons networks. However, only three changes were maintained at the network level, the limbic network to the somatosensory and thalamic networks, as well as the connectivity between the olfactory and retrosplenial network. None of these effects were significant enough to pass FDR correction for multiple comparisons. At 5 Hz stimulation scattered significant effects were seen involving regions within the somatosensory, striatal, olfactory, and pons networks. Only the connectivity between the limbic and pons networks was maintained at the network level which did not pass FDR correction. During 15 Hz phasic LC stimulation, detected significant changes in connectivity were more scattered across the brain and were not maintained at the network level. No effects during 15 Hz phasic stimulation passed FDR correction for multiple comparisons. The results for 6-month AD ChR2, 15-month WT ChR2, and 15-month AD ChR2 are shown in APPENDIX A.

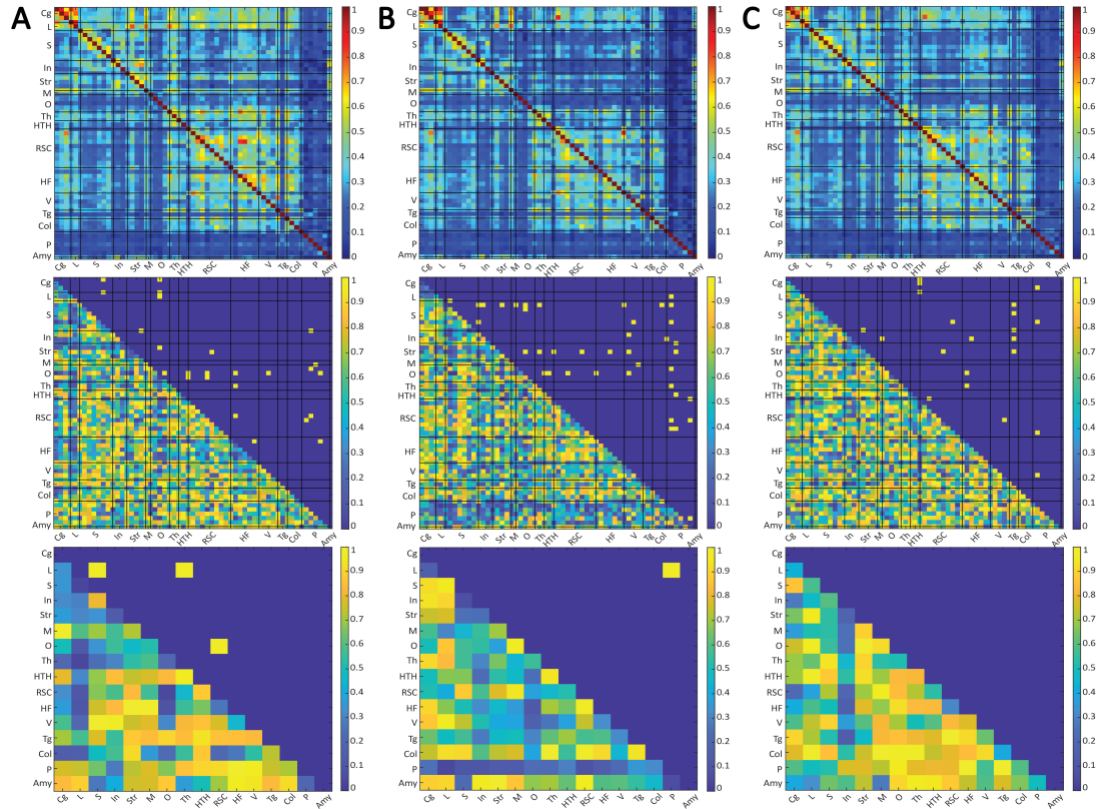


Figure 3.4 Functional connectivity differences as a result of LC stimulation. Results and comparisons between baseline and 2 Hz (A), 5 Hz (B), and 15 Hz phasic (C). The first row shows the Fisher Z-transformed Pearson's correlation values used to calculate functional connectivity, where the bottom triangle across all columns is connectivity for the baseline scans. The top triangle is the functional connectivity for the respective stimulation level. The middle row of figures shows the statistical outcomes of an unpaired t-test between baseline and the respective frequency of stimulation at the parcellation level. The bottom triangle shows the p-values for all comparisons and the top triangle shows statistically significant comparisons before FDR correction ($p < 0.05$). The bottom row shows the same as the middle row at the network level. Network abbreviations are as follows: Cg = cingular; L = limbic; S = somatosensory; In = insular; Str = striatal; M = motor; O = olfactory; Th = thalamus; HTH = hypothalamus; RSC = retrosplenial; HF = hippocampal formation; V = visual; Tg = tegmentum; Col = colliculi; P = pons; Amy = amygdala.

Given that the LC is a bilateral structure and has been shown to produce unilateral effects as a result of stimulation (Grimm et al., 2022), we looked at functional connectivity as divided by stimulated hemisphere (Figure 3.5). It is important to note that in doing this,

certain groups sizes were largely diminished (e.g., $n = 1$). So, while these results should be taken cautiously, they provided a general overview of any potential unilateral effects that could arise from unilateral LC stimulation. Although upon first glance stimulation of the right hemisphere appeared to result in stronger connectivity across the brain, with the exception of 5 Hz, the group sizes for left-stimulated scans were smaller than those of the right side. Additionally, since this effect could also be seen in the baseline scans it is more likely that this is a result of individual subject variability than it is of LC stimulation.

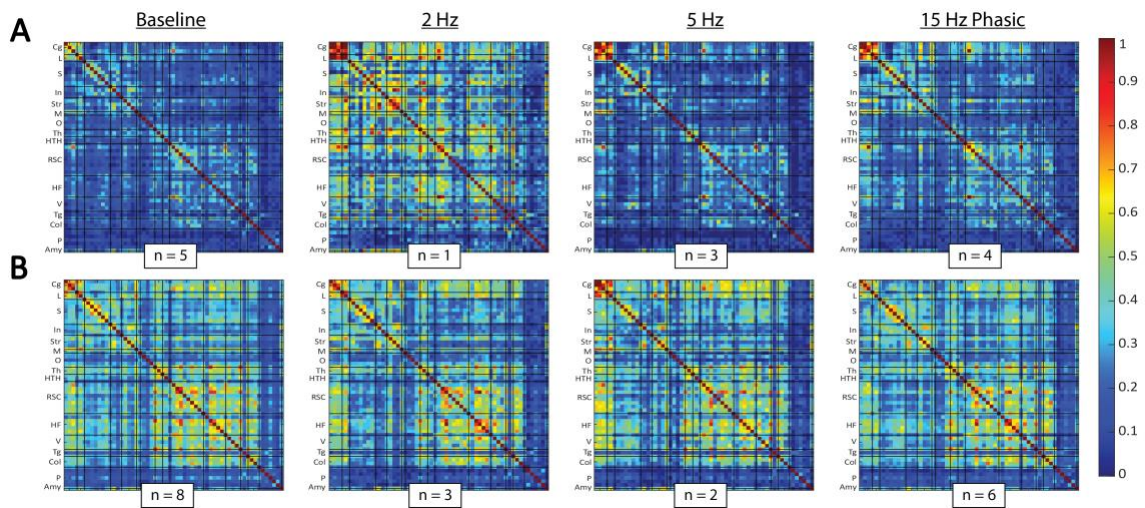


Figure 3.5 Functional connectivity matrices as divided by stimulated hemisphere. (A) Functional connectivity matrices for animals stimulated on the left hemisphere. (B) Functional connectivity for matrices stimulated on the right hemisphere. Differences at the baseline level in addition to small groups sizes indicate that differences shown are a result of individual variability and not differences caused by stimulated hemisphere. Network abbreviations are as follows: Cg = cingular; L = limbic; S = somatosensory; In = insular; Str = striatal; M = motor; O = olfactory; Th = thalamus; HTH = hypothalamus; RSC = retrosplenial; HF = hippocampal formation; V = visual; Tg = tegmentum; Col = colliculi; P = pons; Amy = amygdala.

We also compared the baseline functional connectivity between the WT and AD animals at 6 months and 15 months of age (Figure 3.6). At 6 months, certain regions showed stronger connectivity in the AD animals than in the WT, whereas at 15 months more regions showed similar if not weaker connectivity in AD than WT. Significant changes were observed when comparing across genotype and these changes were notably different at the two age points. At the 6-month timepoint many significant connectivity changes were seen in regions within the limbic, somatosensory, olfactory, thalamic, hippocampal, and amygdala networks. At the network level, significant connectivity changes were dominated by the olfactory network, hypothalamic network, insular network, and the amygdala. However, none of these changes passed FDR correction for multiple comparisons. At 15 months, widespread changes in connectivity were observed with many regions pertaining to the cingular, limbic, insular, olfactory, hippocampal networks, and the amygdala. At the network level, significant changes were seen for the cingular network, the limbic network, within the insular, striatal, and motor networks, as well as in the pons and amygdala. The only effect that survived FDR correction was connectivity between the amygdala and the limbic network (adjusted $p = 0.0319$).

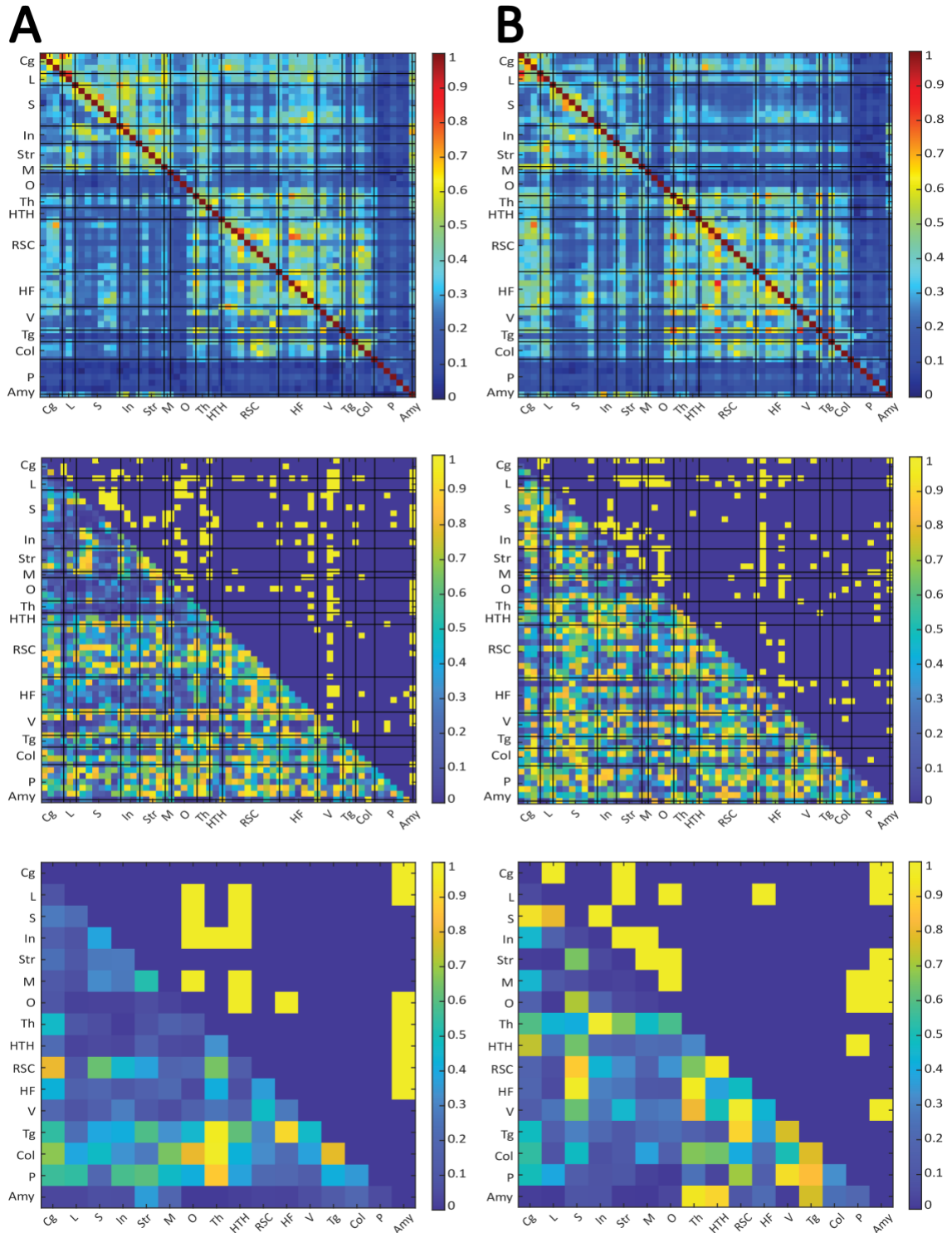


Figure 3.6 Functional connectivity differences between WT and AD animals. Results and comparisons between wildtype (WT) and Alzheimer’s model (AD) animals at 6 months (A) and 15 months (B). The first row shows the Fisher Z-transformed Pearson’s

correlation values used to calculate functional connectivity, where the bottom and top triangles show connectivity for WT and AD animals, respectively. The middle row of figures shows the statistical outcomes of an unpaired t-test between WT and AD at the parcellation level. The bottom triangle shows the p-values for all comparisons and the top triangle shows statistically significant comparisons before FDR correction ($p < 0.05$). The bottom row shows the same as the middle row at the network level. Network abbreviations are as follows: Cg = cingular; L = limbic; S = somatosensory; In = insular; Str = striatal; M = motor; O = olfactory; Th = thalamus; HTH = hypothalamus; RSC = retrosplenial; HF = hippocampal formation; V = visual; Tg = tegmentum; Col = colliculi; P = pons; Amy = amygdala.

3.3.3 *Spatial Distribution of the Global Signal*

To assess whether LC stimulation affects the level of contribution of different brain regions to the global signal we assessed the spatial distribution of the global signal via a voxel-wise correlation analysis (Figure 3.7). In the mCherry control group across all levels of stimulation, higher correlation to the global signal was seen along the midline and bilaterally in posterior regions of the brain. This finding replicates previous work that investigated the spatial distribution of the global signal in a noise-controlled cohort of rats ([Anumba et al., 2023](#)). The same finding was generally observed in the ChR2 stimulated rats however the correlation values were widely elevated throughout the brain in these animals. Of note is the fact that although correlation values were higher throughout the whole brain, the increase was disproportionately higher in the central anterior region during 2 Hz and 5 Hz stimulation of the LC. The more posterior central region of high correlation also appeared to be further increased during 2 Hz stimulation. The results for the 6-month AD, 15-month WT, and 15-month AD animals are shown in APPENDIX A.

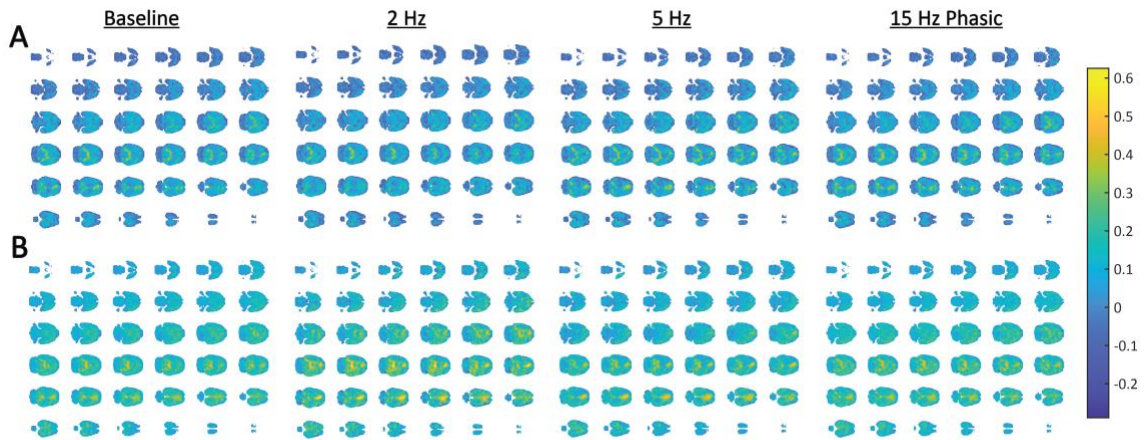


Figure 3.7 Spatial distribution of the global signal during LC stimulation. (A) The spatial distribution of the global signal in the mCherry control animals at different levels of LC stimulation. Correlation is shown in Pearson's correlation coefficients (r). The highest correlation to the global signal was found along the midline in anterior cortical structures as well as bilaterally in posterior parts of the brain, replicating previous results (Anumba et al., 2023). (B) The spatial distribution of the global signal in ChR2 stimulated animals at different levels of LC stimulation. The same pattern of highly correlated structures as seen in the control animals was observed here although with higher correlation seen throughout the whole brain. When compared to baseline, correlation in the bilateral posterior region was stronger during 2 Hz LC stimulation and correlation in the anterior medial structure was stronger during 2 Hz and 5 Hz stimulation of the LC.

3.3.4 Power Spectral Density Analysis of the Global Signal

To evaluate the frequencies contained in each scan, a PSD estimate was created for the scans at each stimulation level for both the mCherry control and ChR2 stimulated rats (Figure 3.8). Typical for resting-state fMRI scans (Pan et al., 2013), at all stimulation levels a low frequency (< 0.02 Hz) peak in activity was observed, after which the magnitude of power proceeded to steadily taper off at higher frequencies. The magnitude of this low frequency peak was maintained around the same level in the ChR2 stimulated animals when compared to the mCherry controls, with the exception of the baseline and 15 Hz

phasic scans for which the low frequency peak was slightly larger in the ChR2 animals. However, no strong notable differences were observed in the power spectra when comparing the corresponding traces for the ChR2 animals to the mCherry controls.

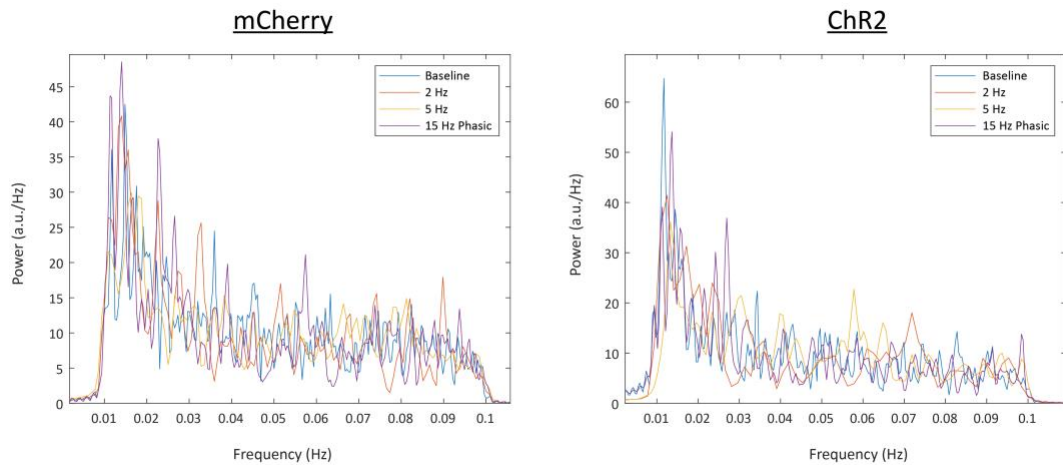


Figure 3.8 Power spectral density (PSD) estimates of the global signal. PSD estimates for the mCherry control animals (left) and the ChR2 stimulated animals (right) are displayed in this figure. All stimulation groups showed a high low-frequency peak in power with a gradual decrease in power as the frequency increased. In the ChR2 animals, the power of this low-frequency peak was higher in the baseline and 15 Hz phasic scans when compared to the control animals. However, no other strong differences were observed between the two groups of animals.

3.3.5 QPP Analysis

As described in the methods, a pattern finding algorithm was used to detect the occurrence of QPPs in this dataset. The STC values of the final QPP template with the scans of each group are shown plotted as a histogram (Figure 3.9A). The set threshold for a QPP event was set to 0.2 and any timepoints at which correlation was above this threshold

were considered QPP events. The distributions of correlation values for all scan groups were fairly normal distributions and the baseline distributions between the mCherry and ChR2 animals showed a near complete overlap. However, when looking at the distributions for the 2 Hz and 5 Hz stimulation levels there was a higher percentage of correlation values above the absolute value of the 0.2 threshold in the ChR2 stimulated animals than in the mCherry controls. This indicates that slightly more QPP events were detected in the ChR2 animals during 2 Hz and 5 Hz stimulation when compared to the mCherry controls. At 15 Hz phasic stimulation, there was more overlap between the two virus groups above the threshold, although this overlap was not as complete as it is for the baseline scans.

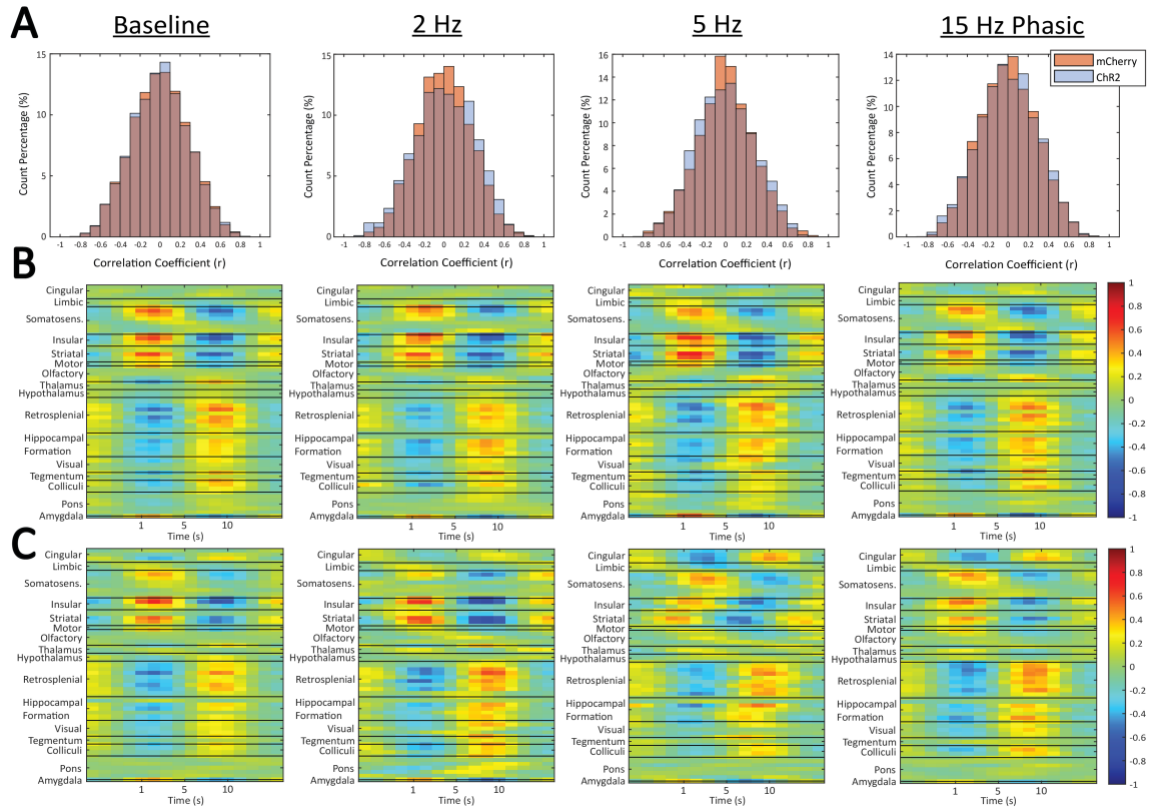


Figure 3.9 QPP detection and templates. (A) STC histograms for mCherry (orange) and Chr2 (blue) animals where values over 0.2 were considered QPP events. Very little difference was shown between the two animal groups; however, a slightly higher percentage of counts were above the 0.2 threshold for the Chr2 animals during 2 Hz and 5 Hz stimulation. (B) QPP templates, or regional activity within the QPP, for mCherry animals at each stimulation level. (C) QPP templates, or regional activity within the QPP, for Chr2 animals at each stimulation level. Distinct differences in regional activity were seen during 5 Hz tonic and 15 Hz phasic LC stimulation.

The QPP template generated for each scan group was also compared across groups as a way to assess the contributed activity of each brain region within the QPP (Figure 3.9B-C). The templates show the waves of activation and deactivation that were experienced by distinct regions and that characterize the QPP. Notably, certain regions exhibited activity that was in phase with each other and distinctly out of phase with other regions, whereas other regions showed very little oscillatory activity in the pattern at all.

The somatosensory, insular, striatal, motor, and amygdala regions all exhibited similar activity that was almost exactly anti-correlated to the activity of the retrosplenial cortex, hippocampal formation, and certain deep brain structures. Other cortical regions, such as the olfactory network and cingulate cortex, and sub-cortical regions such as the thalamus, hypothalamus, and the pons, contributed very little to the dynamic pattern. Of importance is that in the ChR2 animals under 5 Hz tonic and 15 Hz phasic LC stimulation the cingulate cortex showed a much stronger involvement in the QPP than was observed in any of the control animals or at other stimulation levels in the same group. This cingulate activity, when present, moved in phase with the retrosplenial and hippocampal regions. Additionally, during 5 Hz stimulation in the ChR2 animals there was an apparent phase shift in the activity of the insular and striatal regions when compared to that of the somatosensory network. The results for the 6-month AD, 15-month WT, and 15-month AD animals are shown in APPENDIX A.

3.3.6 Complex Principal Component Analysis (CPCA)

Using the unique feature of CPCA to evaluate regional differences in time-lag activity, we performed the analysis as a distinct way to observe the spatiotemporal dynamics in this dataset. Of particular interest to this study is that previous work in humans has shown strong similarity of the first complex principal component to the BOLD global signal and of the second principal component to what is generally considered to be the anticorrelated QPP, or the observed anti-correlation between the DMN and TPN (Bolt et al., 2022). For this reason, also given that the majority of variance explained in the data

was confined to the first few components (Figure 3.12), CPCA results in this study were confined to the first three principal components (PC1, PC2, and PC3).

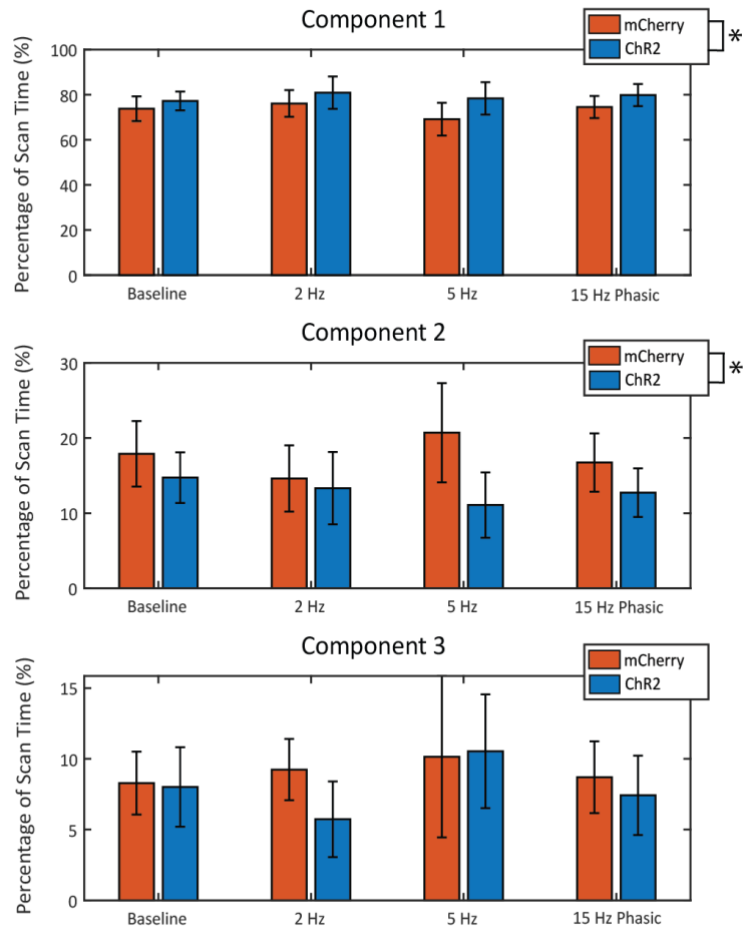


Figure 3.10 Incidence percentage of the first three principal components during LC stimulation. The percentage of scan time for which each of the first 3 principal components was dominant is displayed in this figure. The differences between the control animals (orange) and the stimulated animals (blue) were compared for each level of LC stimulation. Incidence for PC1 across all groups was much higher than it was for PC2 and PC3. A two-way ANOVA revealed significance on account of virus for the first two components, however post-hoc analysis showed no further significance at the level of stimulation.

The effects of LC stimulation on the incidence of each principal component were analyzed by comparing the percentage of scan time that was dominated by each component for the mCherry control group and the ChR2 stimulation group (Figure 3.10). As expected, across groups and stimulation levels, PC1 was responsible for the majority of the variance explained with scans being dominated by PC1 for about 70% of the time. Incidence of PC1 was slightly higher for all stimulated animals as indicated by a two-way ANOVA that reported no effect of stimulation level ($F(3, 66) = 0.68, p = 0.5691$) but a significant effect of the virus used (i.e., whether the virus used contained ChR2 or only mCherry) ($F(1, 66) = 6.19, p = 0.0154$). A post-hoc unpaired t-test at each stimulation level revealed no significant effects of the virus at baseline, 2 Hz stimulation, 5 Hz stimulation, or 15 Hz phasic stimulation ($p = 0.3486, 0.3651, 0.1185, 0.1554$, respectively). The overall incidence of PC2 was much lower than was observed for PC1, however incidence of PC2 was consistently lower in ChR2 stimulated animals when compared to mCherry control animals. A two-way ANOVA revealed no effect of stimulation level ($F(3, 66) = 0.39, p = 0.7578$) but a significant effect of the virus used (i.e., whether the virus used contained ChR2 or only mCherry) ($F(1, 66) = 6.42, p = 0.0137$). A post-hoc unpaired t-test at each stimulation level revealed no significant effects of the virus at baseline, 2 Hz stimulation, 5 Hz stimulation, or 15 Hz phasic stimulation ($p = 0.2821, 0.7358, 0.0561, 0.1469$, respectively). The overall incidence of PC3 was the lowest of the three components with no consistent trend observed across stimulation level or virus. A two-way ANOVA revealed no significant effect of stimulation level ($F(3, 66) = 0.82, p = 0.4892$) or the virus used ($F(1, 66) = 0.89, p = 0.3486$).

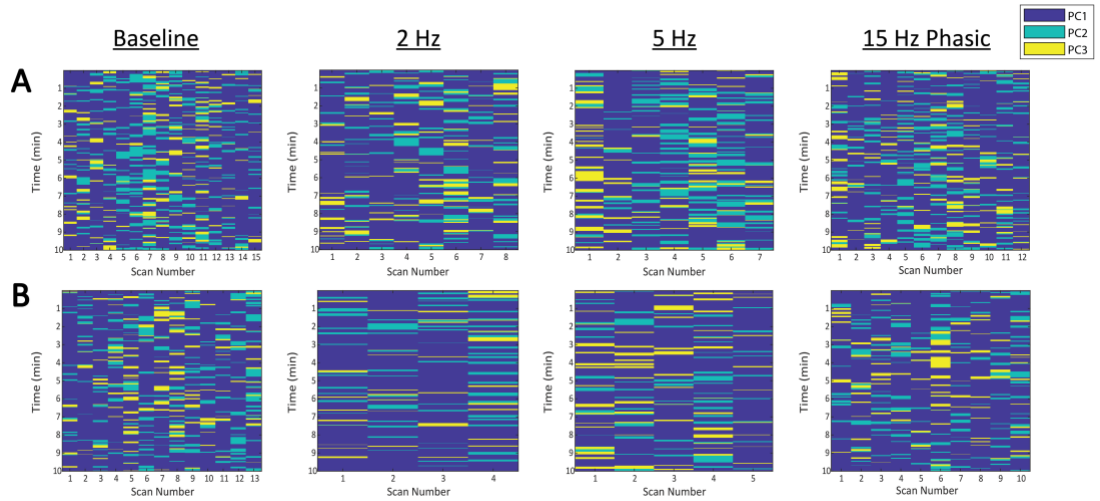


Figure 3.11 Incidence of the first three principal components throughout each scan during LC stimulation. Each graph shows the number of scans in each group and the principal component that was dominant at each timepoint throughout the scan. The results for the mCherry control animals (A) and ChR2 stimulated animals (B) are shown. These graphs show strong individual variability in terms of timing and the temporal distribution of components across scans and across groups.

The timing of when a component was dominant throughout the scan proved to be highly varied across scans (Figure 3.11). It can be clearly seen that most scans spent a majority of their time dominated by PC1 with short periods of PC2 and PC3 interspersed throughout the scan. Although overall the least amount of time was spent in PC3, certain scans were seen to spend more time in PC3 than others (such as scan 1 in the mCherry 5 Hz group and scan 6 in the ChR2 15 Hz phasic group). While longer periods of time (sometimes on the order of minutes) were observed to remain in PC1, the positioning of these time periods with respect to the beginning and the end of the scan varied quite a bit across rats. No observable pattern as to the timing and sequence of the varying component states was seen on the basis of virus or stimulation level.

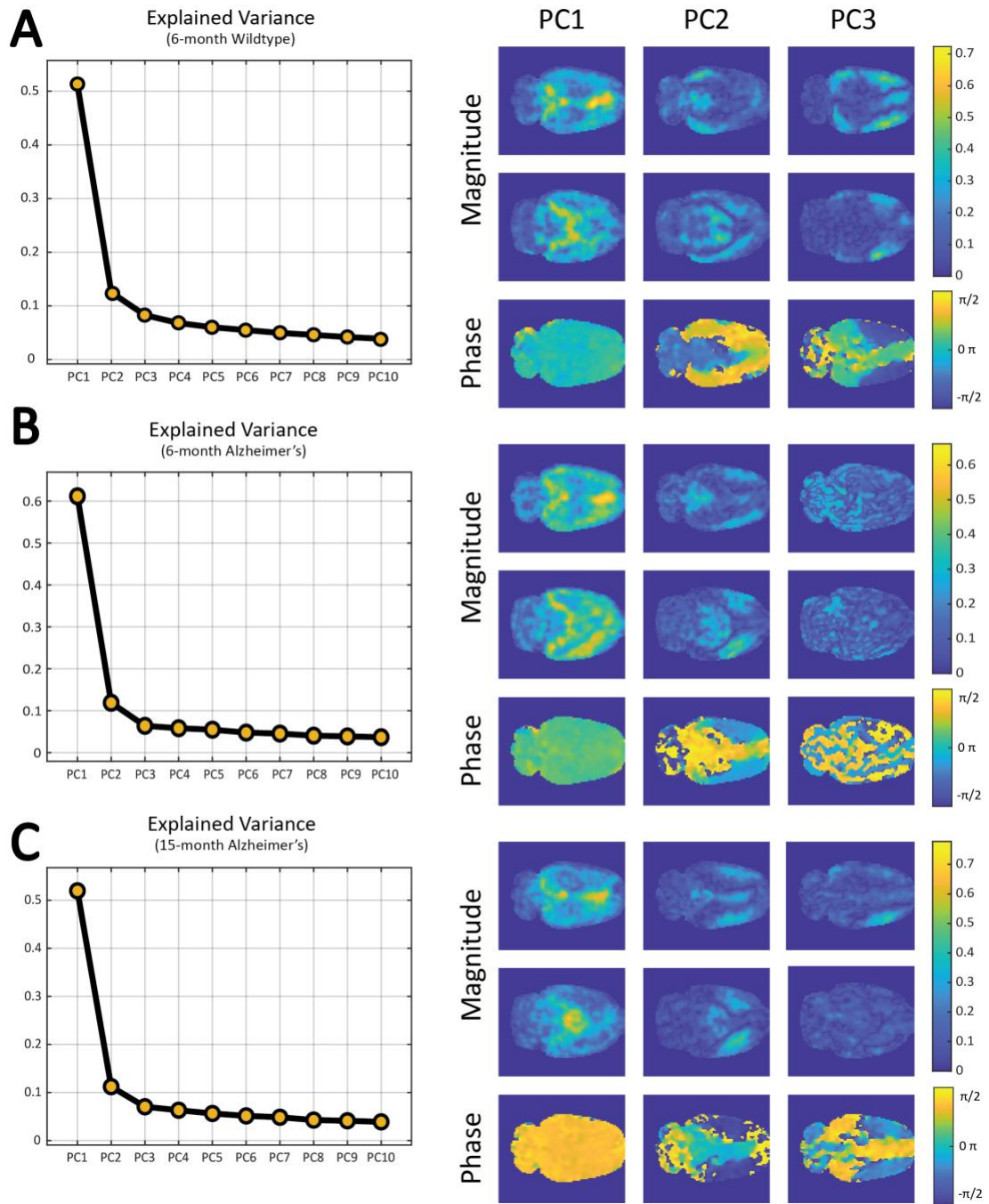


Figure 3.12 A representative look into the first three principal components in WT and AD animals. Graphs for the explained variance and representative slices of the phase and magnitude maps of the first three components (PC1, PC2, PC3) for the 6-month WT animals (A), the 6-month AD animals (B), and the 15-month AD animals (C). Data shown

for each group were taken from the baseline scans of the mCherry control animals for that group. The first three principal components for all groups accounted for the majority of variance explained in the scans. The phase and magnitude maps of PC1 reflected those of the global signal as seen in rats. The phase and magnitude maps of PC3 in the WT animals reflected behavior of the QPP, whereas activity shown in the AD animals showed slight differences in magnitude and apparent dephasing in certain regions. When compared to the WT animals, the magnitude and phase of PC3 in the 6-month AD animals showed extensive spatial disruption, whereas the magnitude in the 15-month AD animals reflected this to a lesser degree with the phase more closely resembling that of the WT animals.

Given the novelty and recent introduction of CPCA as it applies to neuroimaging and BOLD signals ([Bolt et al., 2022](#)), we decided to utilize this analysis as a means to provide a fresh angle of studying Alzheimer's disease (AD). To the best of our knowledge, CPCA has not previously been applied to Alzheimer's data where it could provide a unique perspective on changes in the time-lag activity of brain regions in the disease. We applied CPCA to the baseline scans of the WT and TgF344-AD mCherry rats in both the 6-month and 15-month cohorts as a preliminary examination of how principal component magnitude, phase, and incidence are affected by both AD pathophysiology and age (Figure 3.12). Similar to WT animals, AD rats showed a much larger proportion of variance explained by PC1 when compared to the other principal components. The spatial map of the magnitude of PC1 also showed that the strongest magnitude levels were confined to the first component. PC1 magnitude was also spatially similar across genotypes and age groups, exhibiting a higher magnitude along the anterior midline and bilaterally in posterior cortical areas, reflecting previous findings of the distribution of the global signal in rats ([Anumba et al., 2023](#)). However, this bilateral increase in magnitude was more dispersed in the 6-month AD rats and appeared to be almost non-existent in the 15-month AD animals, where instead higher magnitude was localized to the center of the brain. Despite these

differences, the phase of PC1 across all groups showed the entire brain being in phase, also bearing resemblance to the global signal. The magnitude of PC2 in the 6-month WT animals showed higher levels bilaterally in posterior cortex and in the midbrain, whereas the bilateral levels of elevated magnitude in the AD animals were shown to be anteriorly located with lower magnitude levels in the midbrain exhibited at 15 months. The magnitude map of PC2 in the 15-month AD animals more closely resembled that of PC3 in the 6-month WT animals. The phase map of PC2 in the WT animals showed most of cortex being in phase with each other and almost directly out of phase with midbrain regions. The PC2 phase map in the 6-month AD rats showed a similar division of phase, although bearing more resemblance to that of PC3 in the WT, with some dephasing appearing in the cerebellar and midbrain regions. At 15-months in the AD animals, the PC2 phase looked similar to that of the 6-month AD animals however, more dephasing was seen throughout the brain. PC3 in the WT animals showed elevated magnitude distributed throughout anterior cortex, however in the 6-month AD animals coherent structure of high magnitude was almost lost. The same was true in the 15-month AD animals, with the exception of a small region of cortex in the right hemisphere. The division of phase for PC3 in the WT animals displayed differences between anterior cortex and both the midbrain and posterior cortex, with varied dephasing in the cerebellar region. Similar to the corresponding magnitude map, the PC3 phase map in 6-month AD animals showed almost noise-like dephasing throughout the brain, whereas in 15-month AD animals the phase division more closely resembled that seen in the 6-month WT animals.

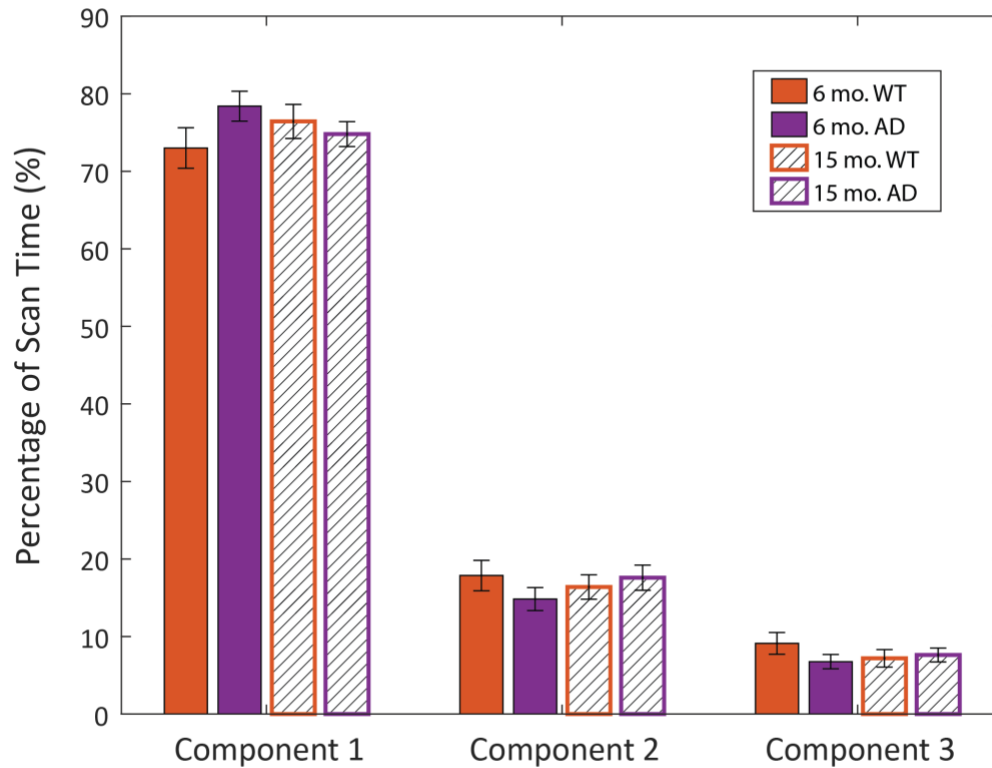


Figure 3.13 Incidence percentage of the first three principal components in WT and AD animals. The percentage of time dominated by each of the first three principal components was looked at in both WT and AD animals at 6-months and 15-months. No significant effects were reported via two-way ANOVA on the basis of genotype or age. However, the interaction of genotype x age was significant for all three components, indicating that effects of aging on the incidence of these components is impacted by genotype.

We also observed the incidence of the first three components with respect to age and genotype of the animals (Figure 3.13). The proportion of time dominated by each component showed only small differences across groups. For WT animals the incidence of PC1 increased slightly with age, whereas in AD animals PC1 incidence decreased slightly

with age. A similar phenomenon was observed with PC2 and PC3, however the trends were observed in reverse as incidence decreased with age in WT animals and increased with age in AD animals. These trends were verified by a two-way ANOVA for each component. For PC1 no effect was revealed on the basis of genotype ($F(1, 243) = 3.01, p = 0.0838$) or age ($F(1, 243) = 0.01, p = 0.9301$), however a significant interaction effect was found for genotype x age ($F(1, 243) = 10.51, p = 0.0014$). For PC2 no effect of genotype ($F(1, 243) = 1.17, p = 0.2804$) or age ($F(1, 243) = 0.56, p = 0.4559$) was reported, but a significant interaction effect was found for genotype x age ($F(1, 243) = 6.23, p = 0.0132$). For PC3 no effect was observed on the basis of genotype ($F(1, 243) = 2.94, p = 0.0878$) or age ($F(1, 243) = 0.92, p = 0.338$), however a significant interaction effect was seen for genotype x age ($F(1, 243) = 6.16, p = 0.0137$). These results indicate that genotype may influence the impact of aging on the incidence of each component.

3.4 Discussion

Both the BOLD global signal and QPPs are known to hold relationships with arousal and measures of vigilance ([Pisauro et al., 2016](#); [Wong et al., 2012, 2013, 2016](#)), while the LC is known to play a strong role in arousal and has neuromodulatory influence throughout the brain ([Aston-Jones & Cohen, 2005](#); [Berridge & Waterhouse, 2003](#)). Through the use of optogenetic-fMRI, we have shown that stimulation of the LC at different frequencies results in small and regionally specific changes however in the global signal and QPPs, however no significant whole-brain effects were observed.

3.4.1 *LC Stimulation and Functional Connectivity*

Very little effects on functional connectivity were observed on the whole-brain level as a result of LC stimulation at any frequency (Figure 3.4). When looking at regional connections that were initially proven to be statistically significant, they are sparse and unconvincing, as evidenced by the fact that very few are maintained on the network level and that none survived FDR correction for multiple comparisons. However, the results of a recent study showed very small regional effects, on the order of ~0.5% BOLD signal change, as a result of optogenetic LC stimulation at 3 Hz, 5 Hz, and 15 Hz (Grimm et al., 2022). These results indicate that optogenetic stimulation of the LC may result in very small-scale effects, in which case it is likely that we are not capturing such effects with such a large-scale connectivity analysis. This theory is emphasized when looking at functional connectivity matrices as divided by stimulated hemisphere, where individual variability in connectivity seems to be the dominant characteristic present across stimulated levels (Figure 3.5). However, the strongest changes at the network level were observed under 2 Hz LC stimulation, which is often associated with a generalized awake state (Morris et al., 2020). The changes seen here involve the limbic network with the somatosensory network and the thalamus, where LC outputs to the thalamus have been hypothesized to be involved in the promotion of wakefulness (Samuels & Szabadi, 2008). Another big change at this level was between the olfactory network and the retrosplenial network, the latter of which is a primary node of the rat DMN which is most active during this generalized awake state (Lu et al., 2012). At 5 Hz stimulation, which is most strongly associated with stressors and anxiety (Morris et al., 2020), the biggest network change was seen between the limbic network and the pons. However, as explained in the limitations

section, and as can be seen in the top row of (Figure 3.4), use of a surface coil resulted in low signal from the pons and consequently any results involving this region should be taken with caution.

3.4.2 *WT vs. AD Functional Connectivity*

More widespread differences in connectivity were observed between the WT and AD animals (Figure 3.6). Functional connectivity in this AD model has been documented to change with age and disease progression (Anckaerts et al., 2019). In that study, AD animals were compared to WT at five different timepoints, of which the most relevant to this study are 6 months and 16 months. At 6 months they saw a significant decrease in connectivity between the somatosensory, visual, and auditory cortices, as well as between the auditory cortex and the hippocampus, retrosplenial, and cingulate cortices. Conversely, our findings show an uncharacteristic increase in connectivity in the 6-month AD animals when compared to WT (Figure 3.6A). This was observed throughout the brain but showed up most statistically at the parcellated level in the somatosensory, olfactory, and visual cortices, and then at the network level with the olfactory network, insular network, the hypothalamus, and the amygdala. Despite this timepoint being early and corresponding to preclinical stages of AD progression (Kelberman et al., 2022, 2023; Rorabaugh et al., 2017), functional connectivity has been shown to decrease in early AD when compared to healthy controls (Adriaanse et al., 2014; Anckaerts et al., 2019). However, a meta-analysis found reports of significant hyperconnectivity within the DMN and limbic networks in

mild cognitive impairment (the prodromal stage of AD) (Badhwar et al., 2017), trends that can be seen in our data (Figure 3.6A).

In their 2019 paper, Anckaerts et al., saw the least amount of significant connectivity decreases at 16 months, where decreases were observed between the cingulate cortex and the hippocampus and retrosplenial cortex. Additionally, they showed decreases in connectivity between the cingulate cortex and the auditory and visual cortices. At 15 months, our data replicates some of these findings as decreases in functional connectivity are observed with the hippocampus at the parcellation level as well as with the cingulate cortex at the network level (Figure 3.6B). Additionally, we see significant changes at the network level between the insular, striatal, motor, and olfactory networks, and also largely with the limbic network and the amygdala. Interestingly, at neither of these timepoints did we see any big changes in functional connectivity regarding the retrosplenial cortex, a primary hub of the rat DMN, a network in which functional connectivity is well known to decrease in AD (Brier et al., 2012; Gour et al., 2013; Jr et al., 2011). Despite the reported changes, only one survived FDR correction for multiple comparisons: decreased connectivity between the limbic network and the amygdala in 15-month AD animals when compared to WT. The amygdala, often regarded as part of the limbic network, has been shown to exhibit decreased functional connectivity in AD (Yao et al., 2013).

An interesting difference and potential source of explanation for differences between our functional connectivity findings and previous reports is that the current study utilized both male and female rats, whereas many previous studies in the same TgF344-AD rat model have only used rats of one sex (Anckaerts et al., 2019; Muñoz-Moreno et al., 2018, 2020; Tudela et al., 2019). Although no sex differences in AD hallmarks were

reported in the development of the TgF344-AD model (Cohen et al., 2013), sex differences have been reported in Fischer 344 rats with respect to aging (Fowler et al., 2022). While this cannot be stated as a cause of differences in this study, it makes for an interesting focus for future directions.

3.4.3 LC Stimulation and the Global Signal

The global signal has been shown to exhibit an anti-correlated relationship with arousal and vigilance measures across species ([Chang et al., 2016](#); [Pisauro et al., 2016](#); [Wong et al., 2013, 2016](#)). Given this relationship with arousal, we were curious to see how the global signal would be affected by stimulation of the LC whose activity is well-known to be involved in arousal. When looking at PSD estimates, very few differences were observed in the frequencies of activity contained in the scans when comparing the activity in the control group to that of the stimulated group (Figure 3.8). In fact, the largest noticeable difference was observed in the baseline scans where no light exposure was present. It is important to note that this data was bandpass filtered between 0.01 – 1.0 Hz to highlight ultralow fluctuations associated with resting-state activity ([Pan et al., 2013](#)). Therefore, it is possible that higher frequencies contained in the global signal may be significantly affected by LC stimulation.

With respect to the spatial distribution of the global signal, LC stimulation did indeed appear to result in certain changes. Firstly, the primary layout of correlation to the global signal that was observed in both the mCherry and ChR2 animals reflected that reported in ([Anumba et al., 2023](#)), where the midline structure in which correlation to the

global signal was highest was believed to be the cingulate cortex. Interestingly, stimulation of the LC in the ChR2 animals did not equally increase correlation to the global signal throughout the brain, instead resulted in higher correlation from regions that previously showed elevated global signal correlation (Figure 3.7). In (Anumba et al., 2023), the DMN was shown to contribute significantly to the global signal in rats and when matching regions of high global signal correlation to the rat DMN as reported in (Lu et al., 2012), the strongly correlated midline structure was thought to be the cingulate cortex and potentially part of the retrosplenial cortex as well. Studies in humans have also shown that certain DMN nodes, including the posterior cingulate cortex (PCC) for which the retrosplenial cortex is a homologue, have shown both higher activity than the global signal (Raichle et al., 2001) and a higher amplitude of ultra-low frequency fluctuations than the global signal (Yu-Feng et al., 2007). The anterior cingulate cortex (ACC), which corresponds to the cingulate cortex in rodents, is known to be involved in a wide array of high-order cognitive functions such as the regulation of emotions, decision making, and learning (Apps et al., 2016; Stevens et al., 2011). A human brain mapping study that considered brainstem structures showed that the ACC had the strongest summed functional connectivity to all brainstem nuclei, making it a primary hub for cortical-brainstem functional connectivity (Hansen et al., 2023). Beyond being connected to all brainstem nuclei, stimulation of noradrenergic alpha-2a receptors in non-human primates was reported to increase the encoding of negative prediction errors in the ACC, linking the noradrenergic system to the ACC's involvement in learning (Hassani & Womelsdorf, 2023). It is important to note that this effect in which the cingulate cortex showed increased global signal correlation was only observed during tonic 2 Hz and 5 Hz stimulation of the

LC, which are associated with generalized awake states and anxiety, respectively (Morris et al., 2020). These results show that tonic LC stimulation increased the contribution of the cingulate cortex to the global signal, any behavioral or cognitive implications of this would be an interesting direction for future study.

3.4.4 LC Stimulation and QPPs

When identifying QPPs using the robust pattern-detection algorithm reported in (Yousefi et al., 2018), QPPs were detected although there was very little change in their detection rate during LC stimulation (Figure 3.9A). However, when observing the histograms of STC values during different levels of stimulation, we observed slightly higher percentages of correlation values above the 0.2 threshold in the Chr2 animals during 2 Hz and 5 Hz LC stimulation. These findings are contrary to a preliminary study in which atomoxetine, a norepinephrine reuptake inhibitor, and DSP4, a noradrenergic neurotoxin, were used to increase extracellular norepinephrine and lesion the LC, respectively (Abbas et al., 2018). This study reported a decrease in the number of STC values above the threshold in rats that were treated with either atomoxetine or DSP4 when compared to controls, indicating that any deviation from baseline LC activity would result in a decrease in QPPs. However, our study, albeit the effects being relatively small, shows the opposite in that tonic stimulation of the LC if anything increases the level of detected QPPs. An important distinction between these two studies is that the use of atomoxetine and DSP4 are considered more aggressive means of LC activity interference, whereas

optogenetic stimulation can be seen as a more conservative method of manipulating the activity of small regions ([Lee et al., 2022](#)).

The relative regions involved in the detected QPP as well as their activity during the pattern were also observed. The foundational structure of the QPP is very similar across groups and stimulation levels, with certain regions exhibiting stronger activity within the pattern and those regions belonging to one of two groups of structures whose activity is anticorrelated (Figure 3.9B). In particular, the somatosensory, insular, and striatal networks move in phase with each other whereas the activity of the retrosplenial cortex, hippocampus, visual network, and a few midbrain structures is in phase. These groupings of regions within the QPP largely reflect what has previously been reported for QPPs in rats ([Majeed et al., 2011](#); [van den Berg et al., 2022](#)). Interestingly, both of these studies show strong involvement of the cingulate cortex in the QPP at rest, whereas in our study strong activity from the cingulate cortex is only observed during stimulation of the LC at 5 Hz tonic and 15 Hz phasic levels. Under these conditions, the activity of the cingulate cortex is in phase with the retrosplenial cortex and hippocampus which both, in addition to the cingulate cortex, have been defined as part of the rat DMN ([Lu et al., 2012](#)). LC firing at 5 Hz tonic and 15 Hz phasic levels is associated with anxiety and focused attention, respectively ([Carter et al., 2010](#); [Chalermphanupap et al., 2017](#)). These results indicate that LC activity during states of high arousal, whether due to stress-like stimuli or goal-oriented behavior could lead to an increase in activity of the cingulate cortex in rats, especially in the context of slow spatiotemporal patterns like QPPs. It should also be noted that during 5 Hz LC stimulation there was a slight phase shift in the activity of the insular and striatal networks, meaning that their peaks in activity occurred slightly before those of

the other structures. Though this effect has not previously been reported, it is a point of interest that could be further investigated in future studies.

3.4.5 CPCA Findings

We used CPCA to assess whether LC stimulation had any effect on the presentation and occurrence of the first three principal components (PC1, PC2, and PC3) in these rats. A recent study showed that the majority of large-scale spatiotemporal signals that have been detected with fMRI can be explained by the first three principal components of activity as calculated through CPCA ([Bolt et al., 2022](#)). Specifically, they showed that PC1 was reflective of the global signal and that PC2 was indicative of what people define as the anti-correlated QPP. Correspondingly, our results show that in WT rats PC1 is very similar to the global signal, however it appeared to be mainly PC3 instead of PC2 that showed strong commonalities to the anti-correlated QPP (Figure 3.12A). The magnitude of PC1 showed strong resemblance to the spatial distribution of the global signal as shown both in this study (Figure 3.7) and in others ([Anumba et al., 2023](#)). Additionally, the majority of the brain was seen to be in phase for PC1, reflecting the activity of the global average. The spatial magnitude and phase of PC3 showed similarities to previous reports of QPPs in rats ([Majeed et al., 2011](#); [van den Berg et al., 2022](#)), showing that the association of these two spatiotemporal signals to the first three complex principal components is present in rats as well as humans. It is important to note that orthogonal rotation of the spatial weights of the PCs via varimax rotation was not used in this analysis and may account for the fact that PC2 also shows some similar features in phase and magnitude to PC3 ([Andersen et al.,](#)

1999). The inclusion of varimax rotation in future studies will most likely better separate these components.

LC stimulation appeared to have very subtle effects on the incidence of the principal components despite consistent trends being observed on account of the inclusion or omission of ChR2 in the virus used (Figure 3.10). It is not believed that the expression of ChR2 should be the direct cause of such a significant change and that this effect is most likely a result of the animals used in each group. Despite the small effects seen generally with LC stimulation, the comparison that came closest to significance was the incidence of PC2 during 5 Hz stimulation ($p = 0.0561$). This is worth noting because our other findings using the QPP pattern-detecting algorithm show us that stimulation at 5 Hz had notable changes in the presentation of the QPP (Figure 3.9). Given this and the fact that PC2 showed some similar attributes to QPPs, it is possible that these changes during 5 Hz stimulation could be responsible either for the signal that was detected as PC2 when using CPCA or for the reduced frequency of PC2 occurrence that we see in these scans.

We also were interested in whether Alzheimer's disease had an effect on the principal components that were extracted by CPCA. Using the TgF344-AD rat model we found that there were in fact changes in the AD animals when compared to WT (Figure 3.12). Interestingly, the phase and magnitude of PC1 were conserved in both the 6-month and 15-month AD animals. However, the magnitude and phase of PC2 in the AD animals more closely reflected those of PC3 in the WT animals, indicating that perhaps QPP-like patterns accounted for more variance in the AD animals than they did in the WT. Of additional importance is the apparent dephasing throughout the brain that is seen to occur in PC2 and PC3 in AD. This lack of regional structure in the phase of these components

indicates a decrease in synchronous activity within brain regions, which is not entirely surprising as functional connectivity and healthy neuronal signaling are known to decline as AD progresses ([Adriaanse et al., 2014](#); [Badhwar et al., 2017](#); [Brier et al., 2012](#); [Cohen et al., 2013](#); [Gour et al., 2013](#); [Jacobs et al., 2013](#); [Jr et al., 2011](#); [Zhou et al., 2010](#)). Additionally, aging appeared to play a role on the incidence of PC1, PC2, and PC3 depending on whether or not the animal was WT or AD (Figure 3.13). The pathophysiology of AD is known to change as the disease progresses ([Weinshenker, 2018](#)), so it is not surprising that the effects of AD on the first three principal components change with age.

3.4.6 *Potential Subtle Effects*

Despite the LC having global neuromodulatory influence, the majority of the results presented here display effects that are quite subtle and if present affect only specific brain regions or structures as opposed to the whole brain at large. There are multiple potential explanations for this, one of them being that the effects of stimulating small nuclei using optogenetic-fMRI are actually quite small. Studies using this modality to stimulate the ventral posteromedial nucleus (VPM) of the thalamus and LC have reported significant yet small changes in % BOLD signal as a result of stimulation ([Chuang et al., 2023](#); [Grimm et al., 2022](#)). Correspondingly, the sensitivity of optogenetic-fMRI is thought to potentially underreport whole-brain responses when used to stimulate small areas ([Lee et al., 2022](#)). The small effects that were observed could also be explained by the Yerkes-Dodson model which states that the relationship between arousal and performance is explained by an inverted-U-shaped curve where very low and very high levels of arousal result in weak

performance, whereas optimal performance results from an intermediate level of arousal (Watters et al., 1997). This inverted-U curve has also been shown to explain the relationship between LC-NE modulation and network function and behavior (Poe et al., 2020), in which case if, as stated earlier, optogenetic stimulation is seen as a moderate level of LC interference it would make sense that disruptions to our measured signals would be small. Additionally, although our study was designed to account for little interference of effects between scans, a study showed that high tonic firing of the LC can reduce the excitability and NE release of subsequent phasic firing modes (Li et al., 2023). Therefore, it is possible that the length of our scans (10 minutes) with constant stimulation may have resulted in NE depletion resulting in a lack of effects observed over the whole length of the scan. Looking at the same analyses in data with a shorter stimulation period would be a necessary direction for future study. Given the nature of the BOLD signal and its dependence on signal from the brain vasculature, it is important to recognize the role of NE as a vasoconstrictor and how this could have resulted in competing effects to LC stimulation (Bekar et al., 2012). This also speaks to the complexity of the neural and hemodynamic systems involved when measuring these spatiotemporal signals with fMRI. Lastly, despite the valuable advancements that work in rodents allows (Pagani et al., 2023), it is important to note that the animals presented were scanned under anesthesia and that no neuromodulatory system works in isolation. With this in mind, altering one system alone is likely to not give us a comprehensive view of how changes in LC function affect these spatiotemporal signals (van den Brink et al., 2019).

3.4.7 Limitations

One limitation of this study is the fact that in order to observe robust pupil dilation as a result of LC stimulation constant laser exposure was needed, which has not been the case in previous reports ([Grimm et al., 2022](#); [Privitera et al., 2020](#)). So, it is possible that our optogenetic paradigm was not strong enough to produce any widespread effects, however these prior studies were done in a different species using different viruses so a direct comparison in pupillometry outcome may not be appropriate. Additionally, unilateral optogenetic stimulation of the LC has been shown to produce unilateral effects ([Grimm et al., 2022](#)), something that this study was unable to assess due to the lack of bilateral symmetry in the functional atlas that was used. Lastly, the reported activity of certain brainstem structures should be taken cautiously due to the use of a surface coil which was unable to obtain optimal signal from structures at this depth.

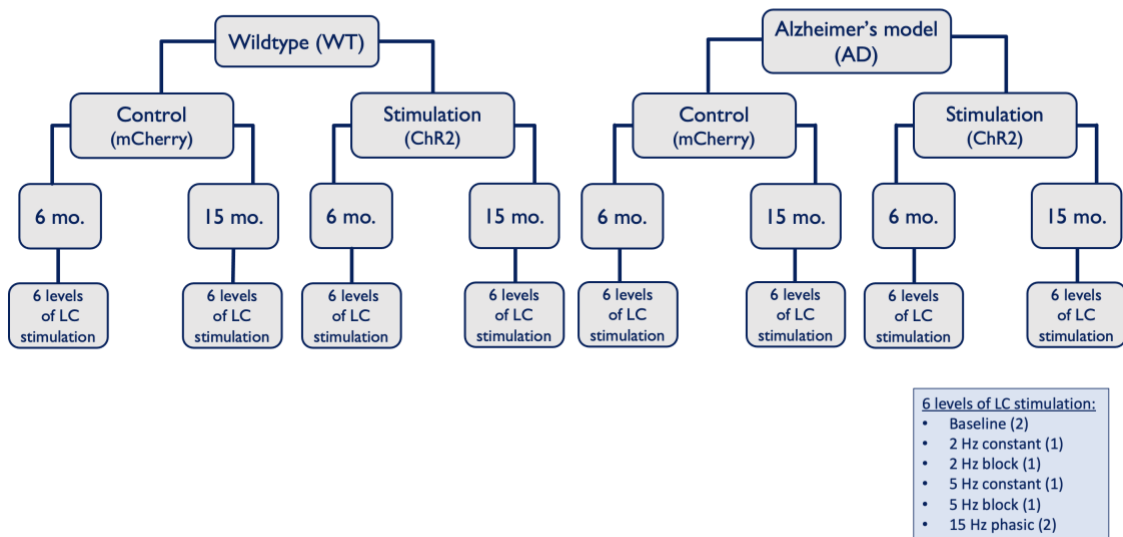
3.5 Conclusion

In this study we combined optogenetic stimulation of the LC with whole-brain fMRI recordings to assess the effects of LC activity on large-scale spatiotemporal dynamics. In this context, we assessed whole-brain functional connectivity, the spatial and spectral components of the BOLD global signal, and the presentation of QPPs. We also investigated how the outcomes of LC stimulation would affect the principal components extracted from CPCA and used an Alzheimer's model to look at differences in functional connectivity and CPCA as a result of the disease. Our findings provide evidence that LC stimulation at specific levels results in small regionally specific effects with regards to the global signal and QPPs. LC stimulation showed very subtle changes in the frequency of

occurrence of CPCA principal components. Comparison of the TgF344-AD rat model and their wildtype counterparts showed differences in functional connectivity and the presentation of the second and third CPCA principal components. These results seem to suggest that the effects of LC stimulation are not simultaneously widespread and large in scale, but instead result in more regional effects. This study contributes an additional puzzle piece of information towards our wholistic understanding of how resting state global dynamics are affected by ongoing neuromodulation and differing brain states such as arousal.

APPENDIX A. ADDITIONAL DATA FROM OPTOGENETIC-FMRI EXPERIMENTS

The study reported in Chapter 3 of this dissertation in which optogenetic-fMRI was used to stimulate the LC was carried out in a variety of groups to assess the influence of several variables (Appendix Figure 1). In addition to just assessing different levels of LC stimulation, we also looked at the effects of age (6-month vs. 15-month) and genotype (WT vs. TgF344-AD). With respect to the effects of LC stimulation, only the results of the 6-month-old WT animals are presented in Chapter 3. This appendix displays the functional connectivity, global signal distribution, and QPP results in the 6-month-old AD, 15-month-old WT, and 15-month-old AD animals.



Appendix Figure 1: Flowchart of Data Acquired. Cohorts of both WT and TgF344-AD (AD) rats were used, each containing control (mCherry) and stimulation (ChR2) rats. Each of these groups had both 6-month-old and 15-month-old animals, all of which underwent

the experimental paradigm involving the six different levels of LC stimulation. Block stimulation scans were not included in this section.

A.1 Animal Group Sizes and Sex

The group sizes for the remaining three groups that were not included in Table 3.1 are provided below in Appendix Table 1.

Appendix Table 1: Remaining Animal Group Sizes

	6-month AD ChR2	15-month WT ChR2	15-month AD ChR2
	Animals (Scans)	Animals (Scans)	Animals (Scans)
Baseline	4 (7)	4 (7)	5 (8)
2 Hz	3 (3)	3 (3)	5 (5)
5 Hz	4 (4)	4 (4)	5 (5)
15 Hz Phasic	4 (8)	4 (6)	5 (9)

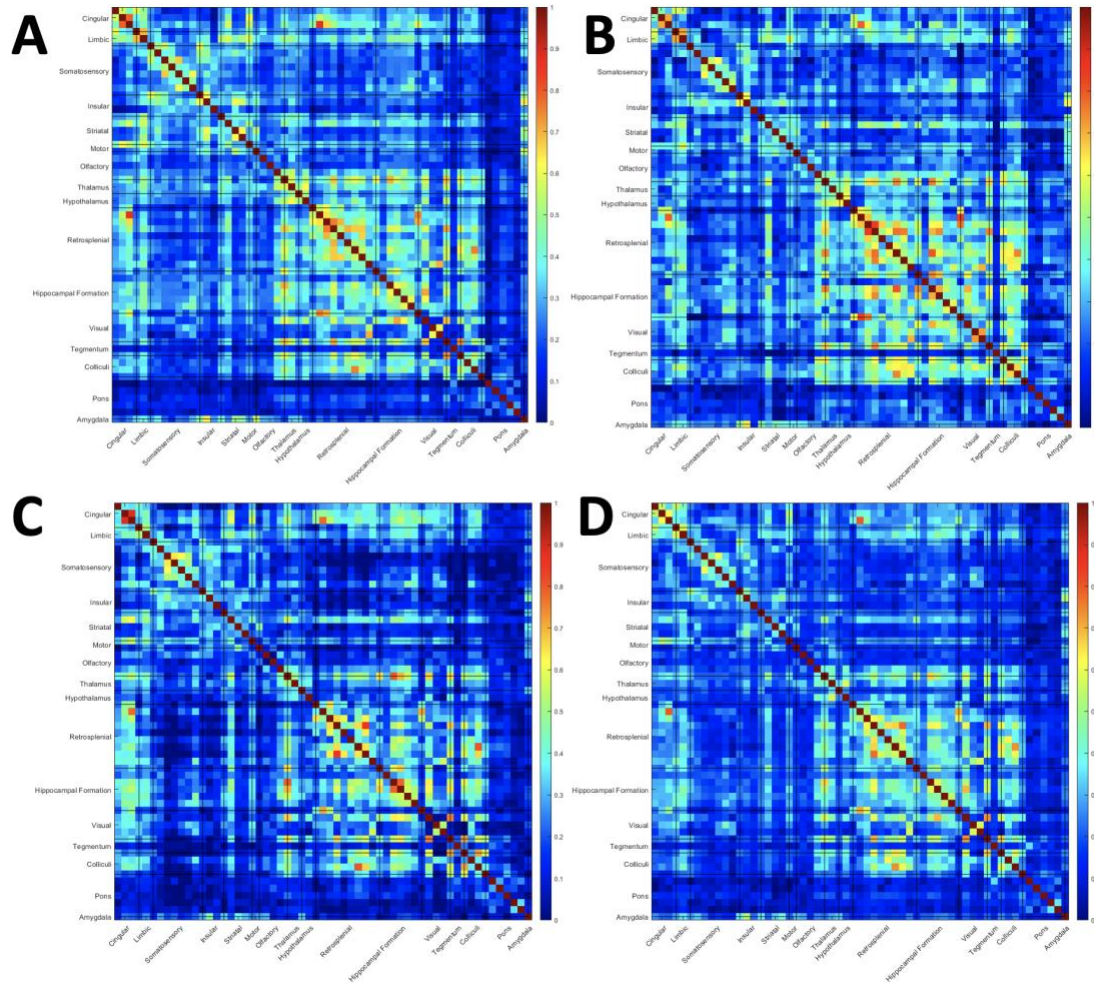
The division of how many male and female rats were included in each group is displayed below in Appendix Table 2.

Appendix Table 2: Animal Group Sizes by Sex

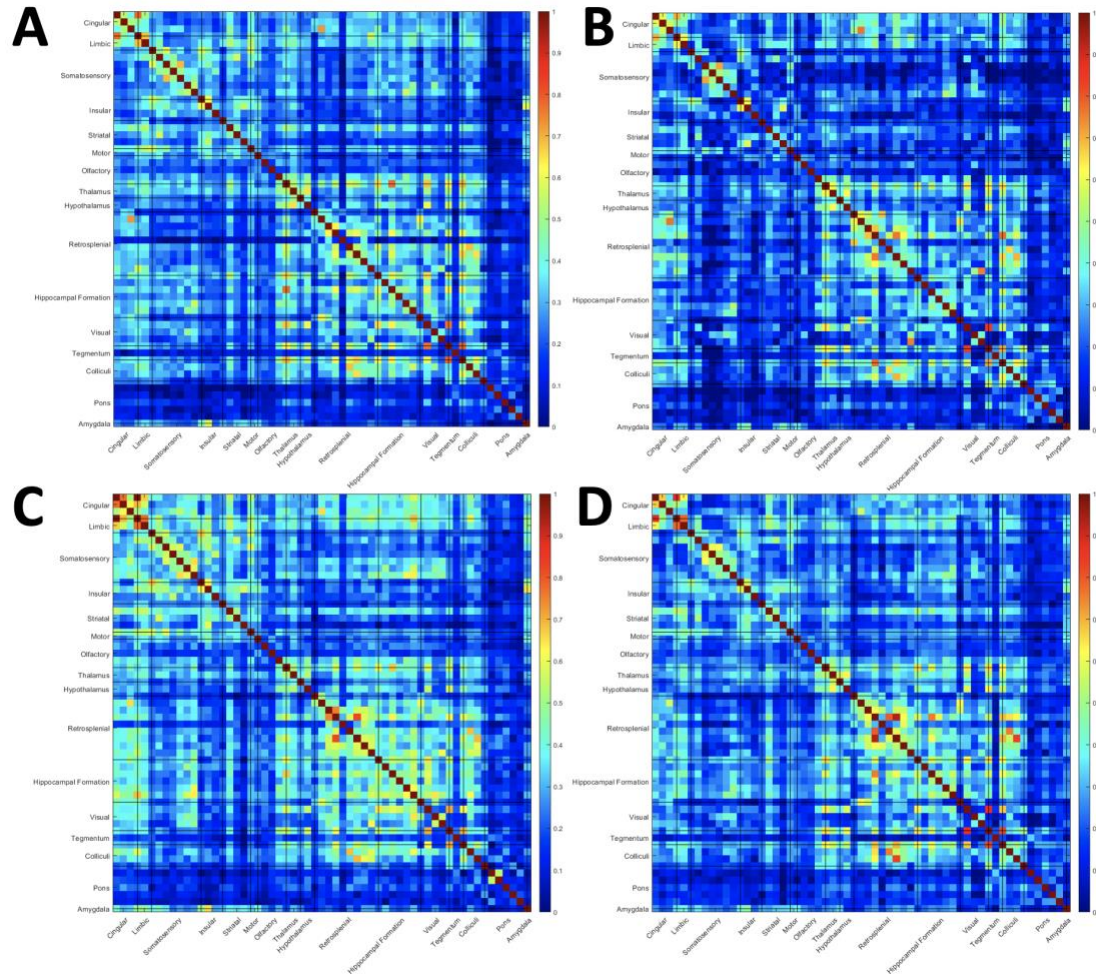
	6-month WT mCherry (M/F)	6- month WT ChR2 (M/F)	6-month AD mCherry (M/F)	6- month AD ChR2 (M/F)	15- month WT mCherry (M/F)	15- month WT ChR2 (M/F)	15- month AD mCherry (M/F)	15- month AD ChR2 (M/F)
Baseline	4/5	2/5	4/7	2/2	6/4	2/2	6/6	3/2
2 Hz	3/5	1/3	2/7	1/2	3/3	2/1	5/5	2/3
5 Hz	2/5	2/4	4/6	2/2	5/4	2/2	6/4	3/2
15 Hz Phasic	3/5	2/4	4/5	2/2	5/4	2/2	5/4	2/3

A.2 Functional Connectivity

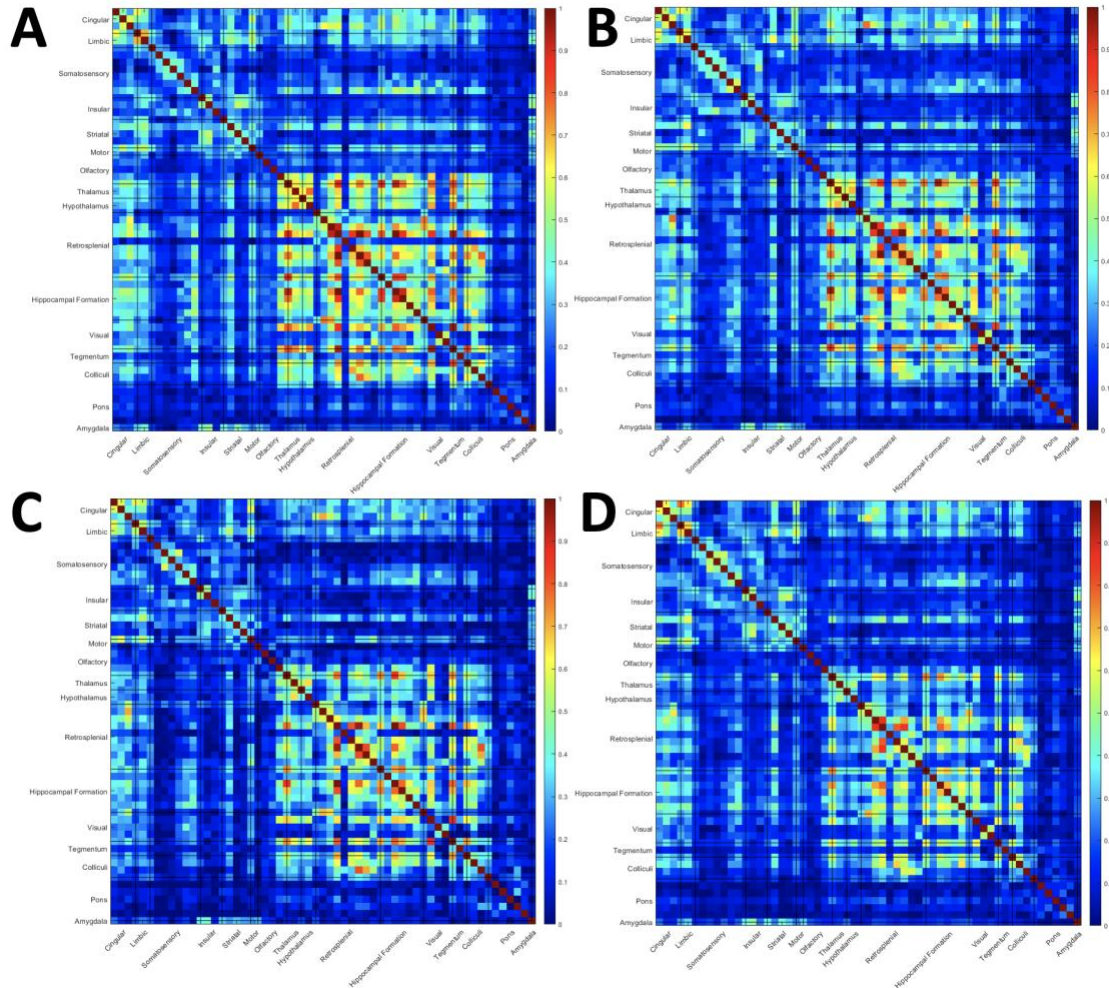
Below are the functional connectivity results for the groups not displayed in Section 3.3.2.



Appendix Figure 2: Functional connectivity for 6-month AD ChR2 animals. The functional connectivity matrices for this group at baseline (A), 2 Hz (B), 5 Hz (C), and 15 Hz phasic (D) stimulation.



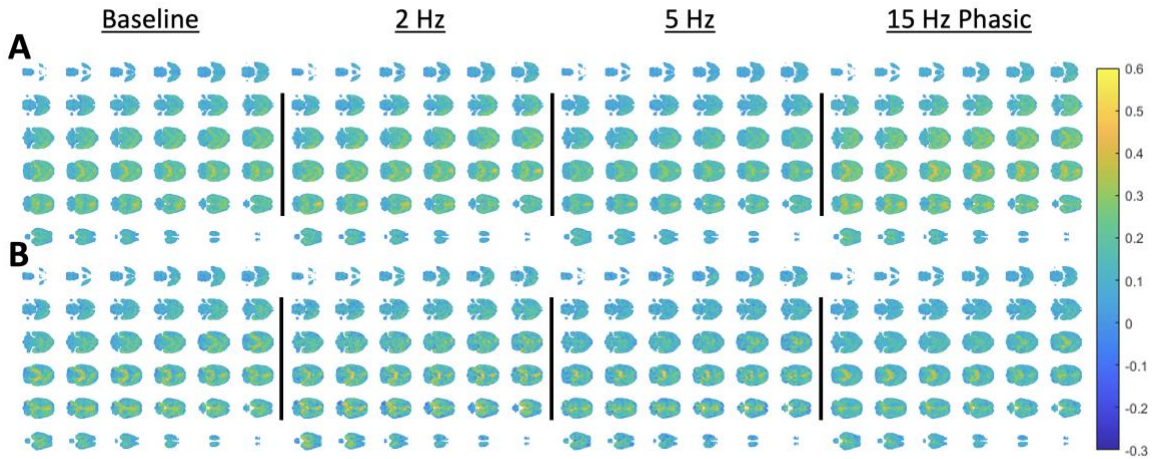
Appendix Figure 3: Functional connectivity for 15-month WT Chr2 Animals. The functional connectivity matrices for this group at baseline (A), 2 Hz (B), 5 Hz (C), and 15 Hz phasic (D) stimulation.



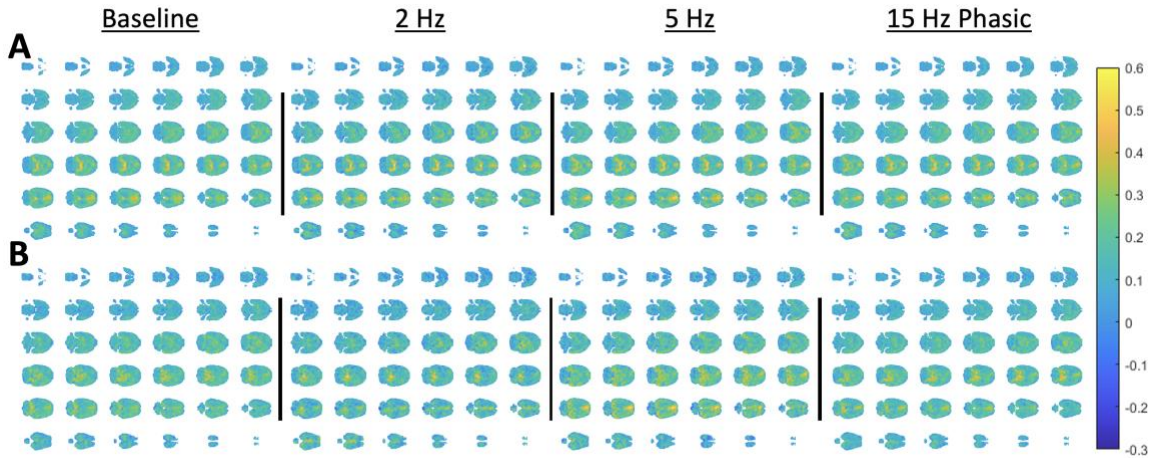
Appendix Figure 4: Functional connectivity for 15-month AD ChR2 animals. The functional connectivity matrices for this group at baseline (A), 2 Hz (B), 5 Hz (C), and 15 Hz phasic (D) stimulation.

A.3 Spatial Distribution of the Global Signal

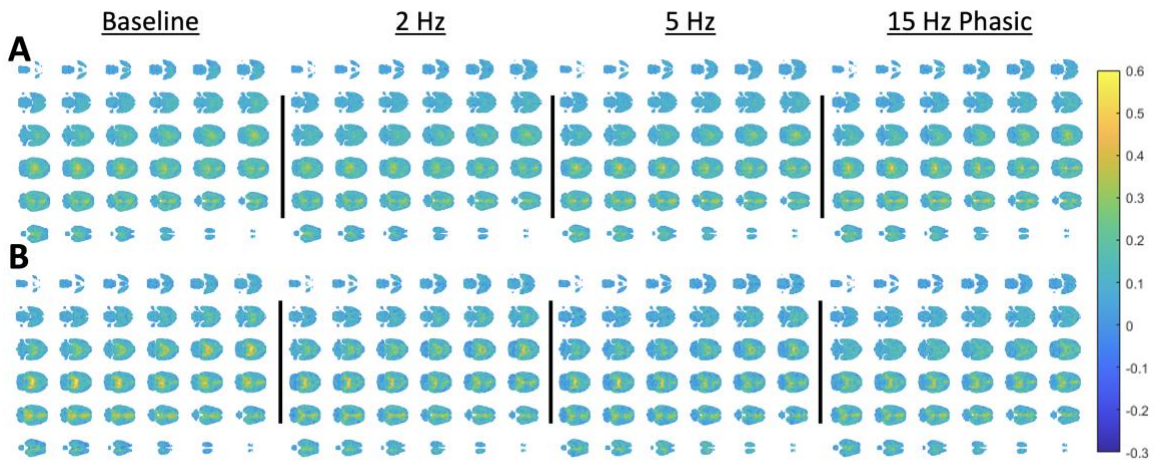
Below are the global signal spatial distribution results for the groups not displayed in Section 3.3.3.



Appendix Figure 5: Spatial distribution of the global signal for 6-month AD animals. The global signal distributions results for this group shown for the mCherry animals (A) and the ChR2 animals (B).



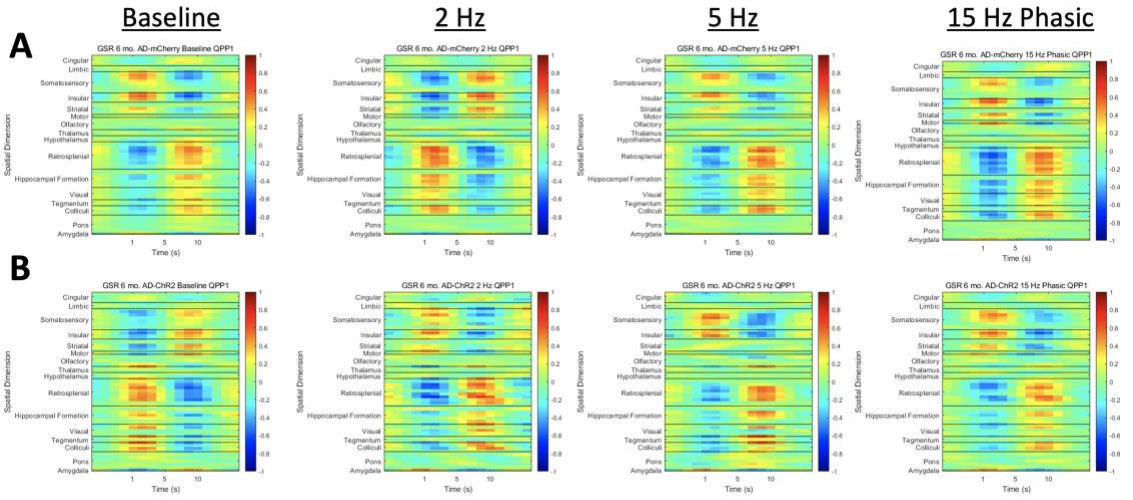
Appendix Figure 6: Spatial distribution of the global signal for 15-month WT animals. The global signal distributions results for this group shown for the mCherry animals (A) and the ChR2 animals (B).



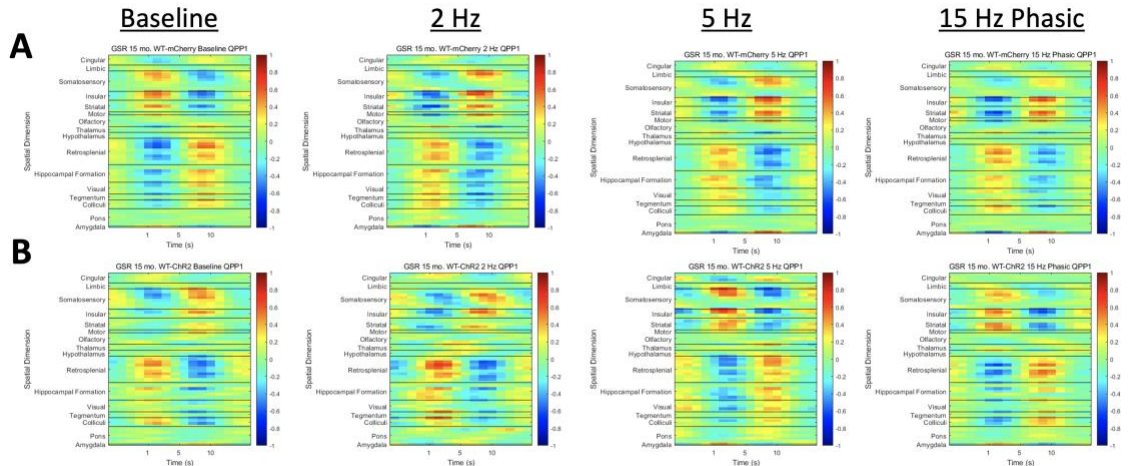
Appendix Figure 7: Spatial distribution of the global signal for 15-month AD animals. The global signal distributions results for this group shown for the mCherry animals (A) and the ChR2 animals (B).

A.4 QPP Analysis

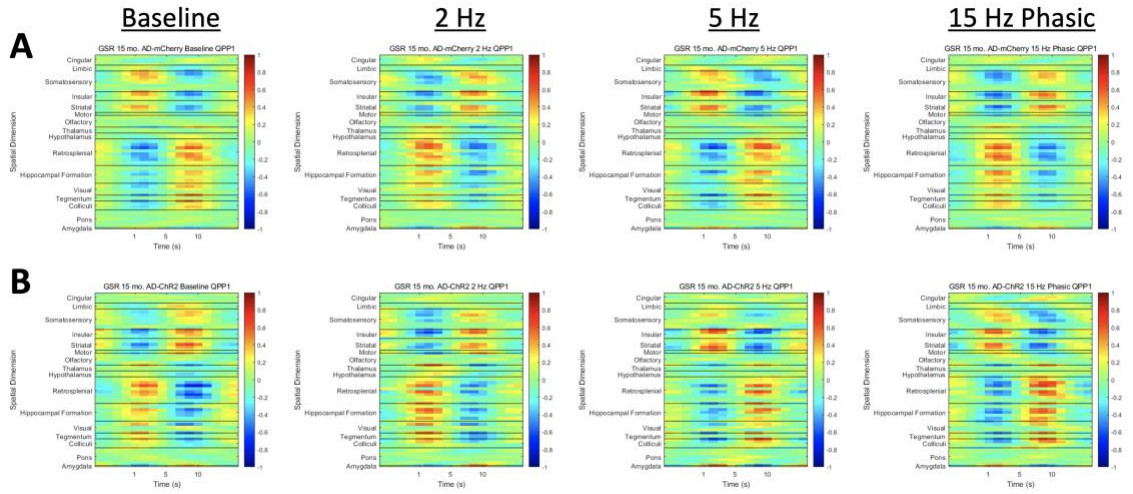
Below are the QPP templates for the groups not displayed in Section 3.3.5.



Appendix Figure 8: QPP templates for 6-month AD animals. QPP templates for this group shown for the mCherry animals (A) and the Chr2 animals (B).



Appendix Figure 9: QPP templates for 15-month WT animals. QPP templates for this group shown for the mCherry animals (A) and the Chr2 animals (B).



Appendix Figure 10: QPP templates for 15-month AD animals. QPP templates for this group shown for the mCherry animals (A) and the Chr2 animals (B).

REFERENCES

- Abbas, A., Bassil, Y., & Keilholz, S. (2019). Quasi-periodic patterns of brain activity in individuals with attention-deficit/hyperactivity disorder. *NeuroImage: Clinical*, *21*, 101653. <https://doi.org/10.1016/j.nicl.2019.101653>
- Abbas, A., Belloy, M., Kashyap, A., Billings, J., Nezafati, M., Schumacher, E. H., & Keilholz, S. (2019). Quasi-periodic patterns contribute to functional connectivity in the brain. *NeuroImage*, *191*, 193–204. <https://doi.org/10.1016/j.neuroimage.2019.01.076>
- Abbas, A., Nezafati, M., Thomas, I., & Keilholz, S. (2018). *Quasiperiodic Patterns in BOLD fMRI Reflect Neuromodulatory Input*. International Society for Magnetic Resonance in Medicine. <https://index.miramart.com/ISMRM2018/PDFfiles/1118.html>
- Adriaanse, S. M., Binnewijzend, M. A. A., Ossenkoppele, R., Tijms, B. M., Flier, W. M. van der, Koene, T., Smits, L. L., Wink, A. M., Scheltens, P., Berckel, B. N. M. van, & Barkhof, F. (2014). Widespread Disruption of Functional Brain Organization in Early-Onset Alzheimer's Disease. *PLOS ONE*, *9*(7), e102995. <https://doi.org/10.1371/journal.pone.0102995>
- Aguirre, G. K., Zarahn, E., & D'Esposito, M. (1998). The Inferential Impact of Global Signal Covariates in Functional Neuroimaging Analyses. *NeuroImage*, *8*(3), 302–306. <https://doi.org/10.1006/nimg.1998.0367>
- Anckaerts, C., Blockx, I., Summer, P., Michael, J., Hamaide, J., Kreutzer, C., Boutin, H., Couillard-Després, S., Verhoye, M., & Van der Linden, A. (2019). Early functional connectivity deficits and progressive microstructural alterations in the TgF344-AD rat model of Alzheimer's Disease: A longitudinal MRI study. *Neurobiology of Disease*, *124*, 93–107. <https://doi.org/10.1016/j.nbd.2018.11.010>

- Andersen, A. H., Gash, D. M., & Avison, M. J. (1999). Principal component analysis of the dynamic response measured by fMRI: A generalized linear systems framework. *Magnetic Resonance Imaging*, *17*(6), 795–815. [https://doi.org/10.1016/S0730-725X\(99\)00028-4](https://doi.org/10.1016/S0730-725X(99)00028-4)
- Andersson, J. L. R., Skare, S., & Ashburner, J. (2003). How to correct susceptibility distortions in spin-echo echo-planar images: Application to diffusion tensor imaging. *NeuroImage*, *20*(2), 870–888. [https://doi.org/10.1016/S1053-8119\(03\)00336-7](https://doi.org/10.1016/S1053-8119(03)00336-7)
- Anumba, N., Maltbie, E., Pan, W.-J., LaGrow, T. J., Xu, N., & Keilholz, S. (2023). Spatial and Spectral Components of the BOLD Global Signal in Rat Resting-State Functional MRI. *Magnetic Resonance in Medicine*, *90*(6), 2486–2499. <https://doi.org/10.1002/mrm.29824>
- Apps, M. A. J., Rushworth, M. F. S., & Chang, S. W. C. (2016). The Anterior Cingulate Gyrus and Social Cognition: Tracking the Motivation of Others. *Neuron*, *90*(4), 692–707. <https://doi.org/10.1016/j.neuron.2016.04.018>
- Aston-Jones, G., & Cohen, J. D. (2005). AN INTEGRATIVE THEORY OF LOCUS COERULEUS-NOREPINEPHRINE FUNCTION: Adaptive Gain and Optimal Performance. *Annual Review of Neuroscience*, *28*(1), 403–450. <https://doi.org/10.1146/annurev.neuro.28.061604.135709>
- Avants, B., Tustison, N., & Song, G. (2008). Advanced normalization tools (ANTs). *Insight J*, *1*–35. <https://doi.org/10.54294/uvnhin>
- Badhwar, A., Tam, A., Dansereau, C., Orban, P., Hoffstaedter, F., & Bellec, P. (2017). Resting-state network dysfunction in Alzheimer’s disease: A systematic review and meta-analysis. *Alzheimer’s & Dementia : Diagnosis, Assessment & Disease Monitoring*, *8*, 73–85. <https://doi.org/10.1016/j.dadm.2017.03.007>

- Barrière, D. A., Magalhães, R., Novais, A., Marques, P., Selingue, E., Geffroy, F., Marques, F., Cerqueira, J., Sousa, J. C., Boumezbeur, F., Bottlaender, M., Jay, T. M., Cachia, A., Sousa, N., & Mériaux, S. (2019). The SIGMA rat brain templates and atlases for multimodal MRI data analysis and visualization. *Nature Communications*, *10*(1), Article 1. <https://doi.org/10.1038/s41467-019-13575-7>
- Bekar, L. K., Wei, H. S., & Nedergaard, M. (2012). The Locus Coeruleus-Norepinephrine Network Optimizes Coupling of Cerebral Blood Volume with Oxygen Demand. *Journal of Cerebral Blood Flow & Metabolism*, *32*(12), 2135–2145. <https://doi.org/10.1038/jcbfm.2012.115>
- Belloy, M. E., Naeyaert, M., Abbas, A., Shah, D., Vanreusel, V., van Audekerke, J., Keilholz, S. D., Keliris, G. A., Van der Linden, A., & Verhoye, M. (2018). Dynamic resting state fMRI analysis in mice reveals a set of Quasi-Periodic Patterns and illustrates their relationship with the global signal. *NeuroImage*, *180*, 463–484. <https://doi.org/10.1016/j.neuroimage.2018.01.075>
- Belloy, M. E., Shah, D., Abbas, A., Kashyap, A., Roßner, S., Van der Linden, A., Keilholz, S. D., Keliris, G. A., & Verhoye, M. (2018). Quasi-Periodic Patterns of Neural Activity improve Classification of Alzheimer’s Disease in Mice. *Scientific Reports*, *8*(1), Article 1. <https://doi.org/10.1038/s41598-018-28237-9>
- Benarroch, E. E. (2018). Locus coeruleus. *Cell and Tissue Research*, *373*(1), 221–232. <https://doi.org/10.1007/s00441-017-2649-1>
- Berridge, C. W., & Waterhouse, B. D. (2003). The locus coeruleus–noradrenergic system: Modulation of behavioral state and state-dependent cognitive processes. *Brain Research Reviews*, *42*(1), 33–84. [https://doi.org/10.1016/S0165-0173\(03\)00143-7](https://doi.org/10.1016/S0165-0173(03)00143-7)
- Billings, J., & Keilholz, S. (2018). The Not-So-Global Blood Oxygen Level-Dependent Signal. *Brain Connectivity*, *8*(3), 121–128. <https://doi.org/10.1089/brain.2017.0517>

- Birn, R. M., Diamond, J. B., Smith, M. A., & Bandettini, P. A. (2006). Separating respiratory-variation-related fluctuations from neuronal-activity-related fluctuations in fMRI. *NeuroImage*, *31*(4), 1536–1548. <https://doi.org/10.1016/j.neuroimage.2006.02.048>
- Biswal, B., Zerrin Yetkin, F., Haughton, V. M., & Hyde, J. S. (1995). Functional connectivity in the motor cortex of resting human brain using echo-planar mri. *Magnetic Resonance in Medicine*, *34*(4), 537–541. <https://doi.org/10.1002/mrm.1910340409>
- Bolt, T. (2023). *Complex Principal Component Analysis for fMRI* [Python]. https://github.com/tsb46/complex_pca (Original work published 2023)
- Bolt, T., Nomi, J. S., Bzdok, D., Salas, J. A., Chang, C., Thomas Yeo, B. T., Uddin, L. Q., & Keilholz, S. D. (2022). A parsimonious description of global functional brain organization in three spatiotemporal patterns. *Nature Neuroscience*, *25*(8), Article 8. <https://doi.org/10.1038/s41593-022-01118-1>
- Braak, H., & Del Tredici, K. (2011). The pathological process underlying Alzheimer's disease in individuals under thirty. *Acta Neuropathologica*, *121*(2), 171–181. <https://doi.org/10.1007/s00401-010-0789-4>
- Braak, H., Thal, D. R., Ghebremedhin, E., & Del Tredici, K. (2011). Stages of the pathologic process in Alzheimer disease: Age categories from 1 to 100 years. *Journal of Neuropathology and Experimental Neurology*, *70*(11), 960–969. <https://doi.org/10.1097/NEN.0b013e318232a379>
- Brier, M. R., Thomas, J. B., Snyder, A. Z., Benzinger, T. L., Zhang, D., Raichle, M. E., Holtzman, D. M., Morris, J. C., & Ances, B. M. (2012). Loss of intranetwork and internetwork resting state functional connections with Alzheimer's disease progression. *The Journal of Neuroscience: The Official Journal of the Society for Neuroscience*, *32*(26), 8890–8899. <https://doi.org/10.1523/JNEUROSCI.5698-11.2012>

- Carter, M. E., Yizhar, O., Chikahisa, S., Nguyen, H., Adamantidis, A., Nishino, S., Deisseroth, K., & de Lecea, L. (2010). Tuning arousal with optogenetic modulation of locus coeruleus neurons. *Nature Neuroscience*, *13*(12), 1526–1533. <https://doi.org/10.1038/nn.2682>
- Chalermmpalanupap, T., Weinshenker, D., & Rorabaugh, J. M. (2017). Down but Not Out: The Consequences of Pretangle Tau in the Locus Coeruleus. *Neural Plasticity*, *2017*. <https://doi.org/10.1155/2017/7829507>
- Chang, C., Leopold, D. A., Schölvinck, M. L., Mandelkow, H., Picchioni, D., Liu, X., Ye, F. Q., Turchi, J. N., & Duyn, J. H. (2016). Tracking brain arousal fluctuations with fMRI. *Proceedings of the National Academy of Sciences*, *113*(16), 4518–4523. <https://doi.org/10.1073/pnas.1520613113>
- Chuang, K.-H., Lee, H.-L., Li, Z., Chang, W.-T., Nasrallah, F. A., Yeow, L. Y., & Singh, K. K. D. /O. R. (2019). Evaluation of nuisance removal for functional MRI of rodent brain. *NeuroImage*, *188*, 694–709. <https://doi.org/10.1016/j.neuroimage.2018.12.048>
- Chuang, K.-H., Li, Z., Huang, H. H., Khorasani Gerdekoohi, S., & Athwal, D. (2023). Hemodynamic transient and functional connectivity follow structural connectivity and cell type over the brain hierarchy. *Proceedings of the National Academy of Sciences*, *120*(5), e2202435120. <https://doi.org/10.1073/pnas.2202435120>
- Ciric, R., Wolf, D. H., Power, J. D., Roalf, D. R., Baum, G., Ruparel, K., Shinohara, R. T., Elliott, M. A., Eickhoff, S. B., Davatzikos, C., Gur, R. C., Gur, R. E., Bassett, D. S., & Satterthwaite, T. D. (2017). Benchmarking of participant-level confound regression strategies for the control of motion artifact in studies of functional connectivity. *NeuroImage*, *154*, 174–187. <https://doi.org/10.1016/j.neuroimage.2017.03.020>
- Cohen, R. M., Rezai-Zadeh, K., Weitz, T. M., Rentsendorj, A., Gate, D., Spivak, I., Bholat, Y., Vasilevko, V., Glabe, C. G., Breunig, J. J., Rakic, P., Davtayan, H., Agadjanyan, M. G., Kepe, V., Barrio, J. R., Bannykh, S., Szekely, C. A., Pechnick, R. N., & Town, T. (2013). A transgenic Alzheimer rat with plaques, tau

pathology, behavioral impairment, oligomeric $\text{a}\beta$, and frank neuronal loss. *The Journal of Neuroscience: The Official Journal of the Society for Neuroscience*, 33(15), 6245–6256. <https://doi.org/10.1523/JNEUROSCI.3672-12.2013>

Cox, R. W. (1996). AFNI: Software for analysis and visualization of functional magnetic resonance neuroimages. *Computers and Biomedical Research, an International Journal*, 29(3), 162–173. <https://doi.org/10.1006/cbmr.1996.0014>

Deco, G., Hagmann, P., Hudetz, A. G., & Tononi, G. (2014). Modeling Resting-State Functional Networks When the Cortex Falls Asleep: Local and Global Changes. *Cerebral Cortex*, 24(12), 3180–3194. <https://doi.org/10.1093/cercor/bht176>

Elobeid, A., Soininen, H., & Alafuzoff, I. (2012). Hyperphosphorylated tau in young and middle-aged subjects. *Acta Neuropathologica*, 123(1), 97–104. <https://doi.org/10.1007/s00401-011-0906-z>

Facebookarchive/fbpca. (2024). [Python]. Meta Archive. <https://github.com/facebookarchive/fbpca> (Original work published 2014)

Ferron, J.-F., Kroeger, D., Chever, O., & Amzica, F. (2009). Cortical Inhibition during Burst Suppression Induced with Isoflurane Anesthesia. *Journal of Neuroscience*, 29(31), 9850–9860. <https://doi.org/10.1523/JNEUROSCI.5176-08.2009>

Fowler, C., Goerzen, D., Madularu, D., Devenyi, G. A., Chakravarty, M. M., & Near, J. (2022). Longitudinal characterization of neuroanatomical changes in the Fischer 344 rat brain during normal aging and between sexes. *Neurobiology of Aging*, 109, 216–228. <https://doi.org/10.1016/j.neurobiolaging.2021.10.003>

Fox, M. D., Zhang, D., Snyder, A. Z., & Raichle, M. E. (2009). The Global Signal and Observed Anticorrelated Resting State Brain Networks. *Journal of Neurophysiology*, 101(6), 3270–3283. <https://doi.org/10.1152/jn.90777.2008>

- Franceschini, M. A., Radhakrishnan, H., Thakur, K., Wu, W., Ruvinskaya, S., Carp, S., & Boas, D. A. (2010). The effect of different anesthetics on neurovascular coupling. *NeuroImage*, *51*(4), 1367–1377. <https://doi.org/10.1016/j.neuroimage.2010.03.060>
- Ganjoo, P., Farber, N. E., Hudetz, A., Smith, J. J., Samso, E., Kampine, J. P., & Schmeling, W. T. (1998). In vivo effects of dexmedetomidine on laser-Doppler flow and pial arteriolar diameter. *Anesthesiology*, *88*(2), 429–439. <https://doi.org/10.1097/00000542-199802000-00022>
- Gour, N., Felician, O., Didic, M., Koric, L., Gueriot, C., Chanoine, V., Confort-Gouny, S., Guye, M., Ceccaldi, M., & Ranjeva, J. P. (2013). Functional connectivity changes differ in early and late-onset alzheimer’s disease. *Human Brain Mapping*, *35*(7), 2978–2994. <https://doi.org/10.1002/hbm.22379>
- Grandjean, J., Schroeter, A., Batata, I., & Rudin, M. (2014). Optimization of anesthesia protocol for resting-state fMRI in mice based on differential effects of anesthetics on functional connectivity patterns. *NeuroImage*, *102*, 838–847. <https://doi.org/10.1016/j.neuroimage.2014.08.043>
- Grimm, C., Duss, S. N., Privitera, M., Munn, B. R., Frässle, S., Chernysheva, M., Patriarchi, T., Razansky, D., Wenderoth, N., Shine, J. M., Bohacek, J., & Zerbi, V. (2022). *Locus Coeruleus firing patterns selectively modulate brain activity and dynamics* (p. 2022.08.29.505672). bioRxiv. <https://doi.org/10.1101/2022.08.29.505672>
- Grudzien, A., Shaw, P., Weintraub, S., Bigio, E., Mash, D. C., & Mesulam, M. M. (2007). Locus coeruleus neurofibrillary degeneration in aging, mild cognitive impairment and early Alzheimer’s disease. *Neurobiology of Aging*, *28*(3), 327–335. <https://doi.org/10.1016/j.neurobiolaging.2006.02.007>
- Hansen, J. Y., Cauzzo, S., Singh, K., García-Gomar, M. G., Shine, J. M., Bianciardi, M., & Masic, B. (2023). *Integrating brainstem and cortical functional architectures* (p. 2023.10.26.564245). bioRxiv. <https://doi.org/10.1101/2023.10.26.564245>

- Hassani, S. A., & Womelsdorf, T. (2023). *Noradrenergic alpha-2a Receptor Stimulation Enhances Prediction Error Signaling in Anterior Cingulate Cortex and Striatum* (p. 2023.10.25.564052). bioRxiv. <https://doi.org/10.1101/2023.10.25.564052>
- Hwang, D. Y., Carlezon, W. A., Isacson, O., & Kim, K. S. (2001). A high-efficiency synthetic promoter that drives transgene expression selectively in noradrenergic neurons. *Human Gene Therapy*, *12*(14), 1731–1740. <https://doi.org/10.1089/104303401750476230>
- Jacobs, H. I. L., Radua, J., Lückmann, H. C., & Sack, A. T. (2013). Meta-analysis of functional network alterations in Alzheimer’s disease: Toward a network biomarker. *Neuroscience & Biobehavioral Reviews*, *37*(5), 753–765. <https://doi.org/10.1016/j.neubiorev.2013.03.009>
- Jenkinson, M., Beckmann, C. F., Behrens, T. E. J., Woolrich, M. W., & Smith, S. M. (2012). FSL. *NeuroImage*, *62*(2), 782–790. <https://doi.org/10.1016/j.neuroimage.2011.09.015>
- Jr, P., Fc, S., Se, P., Vd, C., & Pm, D. (2011, February 8). *Default mode network connectivity in stable vs progressive mild cognitive impairment*. *Neurology*; *Neurology*. <https://doi.org/10.1212/WNL.0b013e31820af94e>
- Keilholz, S. D., Magnuson, M. E., Pan, W.-J., Willis, M., & Thompson, G. J. (2013). Dynamic properties of functional connectivity in the rodent. *Brain Connectivity*, *3*(1), 31–40. <https://doi.org/10.1089/brain.2012.0115>
- Keilholz, S., Maltbie, E., Zhang, X., Yousefi, B., Pan, W.-J., Xu, N., Nezafati, M., LaGrow, T. J., & Guo, Y. (2020). Relationship Between Basic Properties of BOLD Fluctuations and Calculated Metrics of Complexity in the Human Connectome Project. *Frontiers in Neuroscience*, *14*, 550923. <https://doi.org/10.3389/fnins.2020.550923>

- Kelberman, M. A., Anderson, C. R., Chlan, E., Rorabaugh, J. M., McCann, K. E., & Weinshenker, D. (2022). Consequences of Hyperphosphorylated Tau in the Locus Coeruleus on Behavior and Cognition in a Rat Model of Alzheimer's Disease. *Journal of Alzheimer's Disease*, *86*(3), 1037–1059. <https://doi.org/10.3233/JAD-215546>
- Kelberman, M. A., Rorabaugh, J. M., Anderson, C. R., Marriott, A., DePuy, S. D., Rasmussen, K., McCann, K. E., Weiss, J. M., & Weinshenker, D. (2023). Age-dependent dysregulation of locus coeruleus firing in a transgenic rat model of Alzheimer's disease. *Neurobiology of Aging*, *125*, 98–108. <https://doi.org/10.1016/j.neurobiolaging.2023.01.016>
- Lee, J.-Y., You, T., Woo, C.-W., & Kim, S.-G. (2022). Optogenetic fMRI for Brain-Wide Circuit Analysis of Sensory Processing. *International Journal of Molecular Sciences*, *23*(20), Article 20. <https://doi.org/10.3390/ijms232012268>
- Li, L., Rana, A. N., Li, E. M., Feng, J., Li, Y., & Bruchas, M. R. (2023). Activity-dependent constraints on catecholamine signaling. *Cell Reports*, *42*(12). <https://doi.org/10.1016/j.celrep.2023.113566>
- Liang, Z., King, J., & Zhang, N. (2012). Intrinsic Organization of the Anesthetized Brain. *Journal of Neuroscience*, *32*(30), 10183–10191. <https://doi.org/10.1523/JNEUROSCI.1020-12.2012>
- Liu, T. T., Nalci, A., & Falahpour, M. (2017). The Global Signal in fMRI: Nuisance or Information? *NeuroImage*, *150*, 213–229. <https://doi.org/10.1016/j.neuroimage.2017.02.036>
- Liu, X., de Zwart, J. A., Schölvinck, M. L., Chang, C., Ye, F. Q., Leopold, D. A., & Duyn, J. H. (2018). Subcortical evidence for a contribution of arousal to fMRI studies of brain activity. *Nature Communications*, *9*, 395. <https://doi.org/10.1038/s41467-017-02815-3>

- Liu, X., & Duyn, J. H. (2013). Time-varying functional network information extracted from brief instances of spontaneous brain activity. *Proceedings of the National Academy of Sciences*, *110*(11), 4392–4397. <https://doi.org/10.1073/pnas.1216856110>
- Liu, X., Zhang, N., Chang, C., & Duyn, J. H. (2018). Co-activation patterns in resting-state fMRI signals. *NeuroImage*, *180*, 485–494. <https://doi.org/10.1016/j.neuroimage.2018.01.041>
- Liu, X., Zhu, X.-H., Zhang, Y., & Chen, W. (2013). The Change of Functional Connectivity Specificity in Rats Under Various Anesthesia Levels and its Neural Origin. *Brain Topography*, *26*(3), 363–377. <https://doi.org/10.1007/s10548-012-0267-5>
- Lowe, A. S., Barker, G. J., Beech, J. S., Ireland, M. D., & Williams, S. C. R. (2008). A method for removing global effects in small-animal functional MRI. *NMR in Biomedicine*, *21*(1), 53–58. <https://doi.org/10.1002/nbm.1165>
- Lu, H., Zou, Q., Gu, H., Raichle, M. E., Stein, E. A., & Yang, Y. (2012a). Rat brains also have a default mode network. *Proceedings of the National Academy of Sciences*, *109*(10), 3979–3984. <https://doi.org/10.1073/pnas.1200506109>
- Lu, H., Zou, Q., Gu, H., Raichle, M. E., Stein, E. A., & Yang, Y. (2012b). Rat brains also have a default mode network. *Proceedings of the National Academy of Sciences*, *109*(10), 3979–3984. <https://doi.org/10.1073/pnas.1200506109>
- Macey, P. M., Macey, K. E., Kumar, R., & Harper, R. M. (2004). A method for removal of global effects from fMRI time series. *NeuroImage*, *22*(1), 360–366. <https://doi.org/10.1016/j.neuroimage.2003.12.042>
- Magnuson, M. E., Thompson, G. J., Pan, W.-J., & Keilholz, S. D. (2014). Time-dependent effects of isoflurane and dexmedetomidine on functional connectivity, spectral characteristics, and spatial distribution of spontaneous BOLD

fluctuations. *NMR in Biomedicine*, 27(3), 291–303.
<https://doi.org/10.1002/nbm.3062>

Majeed, W., Magnuson, M., Hasenkamp, W., Schwarb, H., Schumacher, E. H., Barsalou, L., & Keilholz, S. D. (2011). Spatiotemporal dynamics of low frequency BOLD fluctuations in rats and humans. *NeuroImage*, 54(2), 1140–1150.
<https://doi.org/10.1016/j.neuroimage.2010.08.030>

Majeed, W., Magnuson, M., & Keilholz, S. D. (2009). Spatiotemporal dynamics of low frequency fluctuations in BOLD fMRI of the rat. *Journal of Magnetic Resonance Imaging*, 30(2), 384–393. <https://doi.org/10.1002/jmri.21848>

Maltbie, E., Yousefi, B., Zhang, X., Kashyap, A., & Keilholz, S. (2022). Comparison of Resting-State Functional MRI Methods for Characterizing Brain Dynamics. *Frontiers in Neural Circuits*, 16, 681544.
<https://doi.org/10.3389/fncir.2022.681544>

Masamoto, K., Fukuda, M., Vazquez, A., & Kim, S.-G. (2009). Dose-dependent Effect of Isoflurane on Neurovascular Coupling in Rat Cerebral Cortex. *The European Journal of Neuroscience*, 30(2), 242–250. <https://doi.org/10.1111/j.1460-9568.2009.06812.x>

Masamoto, K., & Kanno, I. (2012). Anesthesia and the quantitative evaluation of neurovascular coupling. *Journal of Cerebral Blood Flow & Metabolism*, 32(7), 1233–1247. <https://doi.org/10.1038/jcbfm.2012.50>

McCall, J. G., Al-Hasani, R., Siuda, E. R., Hong, D. Y., Norris, A. J., Ford, C. P., & Bruchas, M. R. (2015). CRH engagement of the locus coeruleus noradrenergic system mediates stress-induced anxiety. *Neuron*, 87(3), 605–620.
<https://doi.org/10.1016/j.neuron.2015.07.002>

- Morris, L. S., McCall, J. G., Charney, D. S., & Murrrough, J. W. (2020). The role of the locus coeruleus in the generation of pathological anxiety. *Brain and Neuroscience Advances*, 4, 2398212820930321. <https://doi.org/10.1177/2398212820930321>
- Muñoz-Moreno, E., Tudela, R., López-Gil, X., & Soria, G. (2018). Early brain connectivity alterations and cognitive impairment in a rat model of Alzheimer's disease. *Alzheimer's Research & Therapy*, 10(1), 16. <https://doi.org/10.1186/s13195-018-0346-2>
- Muñoz-Moreno, E., Tudela, R., López-Gil, X., & Soria, G. (2020). Brain connectivity during Alzheimer's disease progression and its cognitive impact in a transgenic rat model. *Network Neuroscience*, 4(2), 397–415. https://doi.org/10.1162/netn_a_00126
- Murphy, K., Birn, R. M., & Bandettini, P. A. (2013). Resting-state fMRI confounds and cleanup. *NeuroImage*, 80, 349–359. <https://doi.org/10.1016/j.neuroimage.2013.04.001>
- Murphy, K., & Fox, M. D. (2017). Towards a consensus regarding global signal regression for resting state functional connectivity MRI. *Neuroimage*, 154, 169–173. <https://doi.org/10.1016/j.neuroimage.2016.11.052>
- Ohata, H., Iida, H., Dohi, S., & Watanabe, Y. (1999). Intravenous dexmedetomidine inhibits cerebrovascular dilation induced by isoflurane and sevoflurane in dogs. *Anesthesia and Analgesia*, 89(2), 370–377. <https://doi.org/10.1097/00000539-199908000-00023>
- Oyarzabal, E. A., Hsu, L.-M., Das, M., Chao, T.-H. H., Zhou, J., Song, S., Zhang, W., Smith, K. G., Sciolino, N. R., Evsyukova, I. Y., Yuan, H., Lee, S.-H., Cui, G., Jensen, P., & Shih, Y.-Y. I. (2021). *Chemogenetic activation of Locus Coeruleus Noradrenergic Neurons Modulates the Default Mode Network* (p. 2021.10.28.463794). <https://doi.org/10.1101/2021.10.28.463794>

- Pagani, M., Gutierrez-Barragan, D., de Guzman, A. E., Xu, T., & Gozzi, A. (2023). Mapping and comparing fMRI connectivity networks across species. *Communications Biology*, 6(1), Article 1. <https://doi.org/10.1038/s42003-023-05629-w>
- Pais-Roldán, P., Biswal, B., Scheffler, K., & Yu, X. (2018). Identifying Respiration-Related Aliasing Artifacts in the Rodent Resting-State fMRI. *Frontiers in Neuroscience*, 12. <https://www.frontiersin.org/articles/10.3389/fnins.2018.00788>
- Pan, W.-J., Khalizad Sharghi, V., Zhang, X., & Keilholz, S. (2020, August 8). *Brain mechanism of anesthesia and sedation: fMRI functional connectivity study with minimized impact of physiological background noise in rats*. ISMRM. <https://archive.ismrm.org/2020/3958.html>
- Pan, W.-J., Thompson, G. J., Magnuson, M. E., Jaeger, D., & Keilholz, S. (2013). Infralow LFP correlates to resting-state fMRI BOLD signals. *NeuroImage*, 74, 288–297. <https://doi.org/10.1016/j.neuroimage.2013.02.035>
- Parkes, L., Fulcher, B., Yücel, M., & Fornito, A. (2018). An evaluation of the efficacy, reliability, and sensitivity of motion correction strategies for resting-state functional MRI. *NeuroImage*, 171, 415–436. <https://doi.org/10.1016/j.neuroimage.2017.12.073>
- Pisauro, M. A., Benucci, A., & Carandini, M. (2016). Local and global contributions to hemodynamic activity in mouse cortex. *Journal of Neurophysiology*, 115(6), 2931–2936. <https://doi.org/10.1152/jn.00125.2016>
- Poe, G. R., Foote, S., Eschenko, O., Johansen, J. P., Bouret, S., Aston-Jones, G., Harley, C. W., Manahan-Vaughan, D., Weinshenker, D., Valentino, R., Berridge, C., Chandler, D. J., Waterhouse, B., & Sara, S. J. (2020). Locus coeruleus: A new look at the blue spot. *Nature Reviews Neuroscience*, 21(11), Article 11. <https://doi.org/10.1038/s41583-020-0360-9>

- Power, J. D., Plitt, M., Laumann, T. O., & Martin, A. (2017). Sources and implications of whole-brain fMRI signals in humans. *NeuroImage*, *146*, 609–625. <https://doi.org/10.1016/j.neuroimage.2016.09.038>
- Privitera, M., Ferrari, K. D., von Ziegler, L. M., Sturman, O., Duss, S. N., Floriou-Servou, A., Germain, P.-L., Vermeiren, Y., Wyss, M. T., De Deyn, P. P., Weber, B., & Bohacek, J. (2020). A complete pupillometry toolbox for real-time monitoring of locus coeruleus activity in rodents. *Nature Protocols*, *15*(8), Article 8. <https://doi.org/10.1038/s41596-020-0324-6>
- Raichle, M. E., MacLeod, A. M., Snyder, A. Z., Powers, W. J., Gusnard, D. A., & Shulman, G. L. (2001). A default mode of brain function. *Proceedings of the National Academy of Sciences*, *98*(2), 676–682. <https://doi.org/10.1073/pnas.98.2.676>
- Raut, R. V., Snyder, A. Z., Mitra, A., Yellin, D., Fujii, N., Malach, R., & Raichle, M. E. (2021). Global waves synchronize the brain's functional systems with fluctuating arousal. *Science Advances*, *7*(30), eabf2709. <https://doi.org/10.1126/sciadv.abf2709>
- Rorabaugh, J. M., Chalermpananupap, T., Botz-Zapp, C. A., Fu, V. M., Lembeck, N. A., Cohen, R. M., & Weinshenker, D. (2017). Chemogenetic locus coeruleus activation restores reversal learning in a rat model of Alzheimer's disease. *Brain*, *140*(11), 3023–3038. <https://doi.org/10.1093/brain/awx232>
- Saad, Z. S., Gotts, S. J., Murphy, K., Chen, G., Jo, H. J., Martin, A., & Cox, R. W. (2012). Trouble at rest: How correlation patterns and group differences become distorted after global signal regression. *Brain Connectivity*, *2*(1), 25–32. <https://doi.org/10.1089/brain.2012.0080>
- Samuels, E. R., & Szabadi, E. (2008). Functional Neuroanatomy of the Noradrenergic Locus Coeruleus: Its Roles in the Regulation of Arousal and Autonomic Function Part I: Principles of Functional Organisation. *Current Neuropharmacology*, *6*(3), 235–253. <https://doi.org/10.2174/157015908785777229>

- Satterthwaite, T. D., Wolf, D. H., Loughead, J., Ruparel, K., Elliott, M. A., Hakonarson, H., Gur, R. C., & Gur, R. E. (2012). Impact of in-scanner head motion on multiple measures of functional connectivity: Relevance for studies of neurodevelopment in youth. *NeuroImage*, *60*(1), 623–632.
<https://doi.org/10.1016/j.neuroimage.2011.12.063>
- Schneider, M., Hathway, P., Leuchs, L., Sämann, P. G., Czisch, M., & Spoormaker, V. I. (2016). Spontaneous pupil dilations during the resting state are associated with activation of the salience network. *NeuroImage*, *139*, 189–201.
<https://doi.org/10.1016/j.neuroimage.2016.06.011>
- Shine, J. M. (2019). Neuromodulatory Influences on Integration and Segregation in the Brain. *Trends in Cognitive Sciences*, *23*(7), 572–583.
<https://doi.org/10.1016/j.tics.2019.04.002>
- Sicard, K., Shen, Q., Brevard, M. E., Sullivan, R., Ferris, C. F., King, J. A., & Duong, T. Q. (2003). Regional cerebral blood flow and BOLD responses in conscious and anesthetized rats under basal and hypercapnic conditions: Implications for functional MRI studies. *Journal of Cerebral Blood Flow and Metabolism: Official Journal of the International Society of Cerebral Blood Flow and Metabolism*, *23*(4), 472–481.
<https://doi.org/10.1097/01.WCB.0000054755.93668.20>
- Slupe, A. M., & Kirsch, J. R. (2018). Effects of anesthesia on cerebral blood flow, metabolism, and neuroprotection. *Journal of Cerebral Blood Flow & Metabolism*, *38*(12), 2192–2208. <https://doi.org/10.1177/0271678X18789273>
- Smith, S. M., Jenkinson, M., Woolrich, M. W., Beckmann, C. F., Behrens, T. E. J., Johansen-Berg, H., Bannister, P. R., De Luca, M., Drobnjak, I., Flitney, D. E., Niazy, R. K., Saunders, J., Vickers, J., Zhang, Y., De Stefano, N., Brady, J. M., & Matthews, P. M. (2004). Advances in functional and structural MR image analysis and implementation as FSL. *NeuroImage*, *23*, S208–S219.
<https://doi.org/10.1016/j.neuroimage.2004.07.051>

- Stevens, F. L., Hurley, R. A., Taber, K. H., Hurley, R. A., Hayman, L. A., & Taber, K. H. (2011). Anterior Cingulate Cortex: Unique Role in Cognition and Emotion. *The Journal of Neuropsychiatry and Clinical Neurosciences*, 23(2), 121–125. <https://doi.org/10.1176/jnp.23.2.jnp121>
- Thomas Yeo, B. T., Krienen, F. M., Sepulcre, J., Sabuncu, M. R., Lashkari, D., Hollinshead, M., Roffman, J. L., Smoller, J. W., Zöllei, L., Polimeni, J. R., Fischl, B., Liu, H., & Buckner, R. L. (2011). The organization of the human cerebral cortex estimated by intrinsic functional connectivity. *Journal of Neurophysiology*, 106(3), 1125–1165. <https://doi.org/10.1152/jn.00338.2011>
- Tillage, R. P., Wilson, G. E., Liles, L. C., Holmes, P. V., & Weinshenker, D. (2020). Chronic Environmental or Genetic Elevation of Galanin in Noradrenergic Neurons Confers Stress Resilience in Mice. *Journal of Neuroscience*, 40(39), 7464–7474. <https://doi.org/10.1523/JNEUROSCI.0973-20.2020>
- Tudela, R., Muñoz-Moreno, E., Sala-Llonch, R., López-Gil, X., & Soria, G. (2019). Resting State Networks in the TgF344-AD Rat Model of Alzheimer’s Disease Are Altered From Early Stages. *Frontiers in Aging Neuroscience*, 11. <https://doi.org/10.3389/fnagi.2019.00213>
- Turchi, J., Chang, C., Ye, F. Q., Russ, B. E., Yu, D. K., Cortes, C. R., Monosov, I. E., Duyn, J. H., & Leopold, D. A. (2018). The Basal Forebrain Regulates Global Resting-State fMRI Fluctuations. *Neuron*, 97(4), 940-952.e4. <https://doi.org/10.1016/j.neuron.2018.01.032>
- Upadhyay, J., Baker, S. J., Chandran, P., Miller, L., Lee, Y., Marek, G. J., Sakoglu, U., Chin, C.-L., Luo, F., Fox, G. B., & Day, M. (2011). Default-Mode-Like Network Activation in Awake Rodents. *PLOS ONE*, 6(11), e27839. <https://doi.org/10.1371/journal.pone.0027839>
- van den Berg, M., Adhikari, M. H., Verschuuren, M., Pintelon, I., Vasilkovska, T., Van Audekerke, J., Missault, S., Heymans, L., Ponsaerts, P., De Vos, W. H., Van der Linden, A., Keliris, G. A., & Verhoye, M. (2022). Altered basal forebrain function during whole-brain network activity at pre- and early-plaque stages of

Alzheimer's disease in TgF344-AD rats. *Alzheimer's Research & Therapy*, 14(1), 148. <https://doi.org/10.1186/s13195-022-01089-2>

van den Brink, R. L., Pfeffer, T., & Donner, T. H. (2019). Brainstem Modulation of Large-Scale Intrinsic Cortical Activity Correlations. *Frontiers in Human Neuroscience*, 13. <https://doi.org/10.3389/fnhum.2019.00340>

Watters, P. A., Martin, F., & Schreter, Z. (1997). Caffeine and Cognitive Performance: The Nonlinear Yerkes–Dodson Law. *Human Psychopharmacology: Clinical and Experimental*, 12(3), 249–257. [https://doi.org/10.1002/\(SICI\)1099-1077\(199705/06\)12:3<249::AID-HUP865>3.0.CO;2-J](https://doi.org/10.1002/(SICI)1099-1077(199705/06)12:3<249::AID-HUP865>3.0.CO;2-J)

Weinshenker, D. (2018). Long Road to Ruin: Noradrenergic Dysfunction in Neurodegenerative Disease. *Trends in Neurosciences*, 41(4), 211–223. <https://doi.org/10.1016/j.tins.2018.01.010>

Wise, R. G., Ide, K., Poulin, M. J., & Tracey, I. (2004). Resting fluctuations in arterial carbon dioxide induce significant low frequency variations in BOLD signal. *NeuroImage*, 21(4), 1652–1664. <https://doi.org/10.1016/j.neuroimage.2003.11.025>

Wong, C. W., DeYoung, P. N., & Liu, T. T. (2016). Differences in the resting-state fMRI global signal amplitude between the eyes open and eyes closed states are related to changes in EEG vigilance. *NeuroImage*, 124(Pt A), 24–31. <https://doi.org/10.1016/j.neuroimage.2015.08.053>

Wong, C. W., Olafsson, V., Tal, O., & Liu, T. T. (2012). Anti-correlated networks, global signal regression, and the effects of caffeine in resting-state functional MRI. *NeuroImage*, 63(1), 356–364. <https://doi.org/10.1016/j.neuroimage.2012.06.035>

Wong, C. W., Olafsson, V., Tal, O., & Liu, T. T. (2013). The amplitude of the resting-state fMRI global signal is related to EEG vigilance measures. *NeuroImage*, 83, 983–990. <https://doi.org/10.1016/j.neuroimage.2013.07.057>

- Xu, N., LaGrow, T. J., Anumba, N., Lee, A., Zhang, X., Yousefi, B., Bassil, Y., Clavijo, G. P., Khalilzad Sharghi, V., Maltbie, E., Meyer-Baese, L., Nezafati, M., Pan, W.-J., & Keilholz, S. (2022). Functional Connectivity of the Brain Across Rodents and Humans. *Frontiers in Neuroscience*, *16*.
<https://www.frontiersin.org/articles/10.3389/fnins.2022.816331>
- Xu, N., Zhang, L., Larson, S., Li, Z., Anumba, N., Daley, L., Pan, W.-J., Chuang, K.-H., & Keilholz, S. D. (2023). Rodent Whole-Brain fMRI Data Preprocessing Toolbox. *Aperture Neuro*, *3*, 1–3. <https://doi.org/10.52294/001c.85075>
- Yan, C.-G., Cheung, B., Kelly, C., Colcombe, S., Craddock, R. C., Di Martino, A., Li, Q., Zuo, X.-N., Castellanos, F. X., & Milham, M. P. (2013). A comprehensive assessment of regional variation in the impact of head micromovements on functional connectomics. *NeuroImage*, *76*, 183–201.
<https://doi.org/10.1016/j.neuroimage.2013.03.004>
- Yao, H., Liu, Y., Zhou, B., Zhang, Z., An, N., Wang, P., Wang, L., Zhang, X., & Jiang, T. (2013). Decreased functional connectivity of the amygdala in Alzheimer’s disease revealed by resting-state fMRI. *European Journal of Radiology*, *82*(9), 1531–1538. <https://doi.org/10.1016/j.ejrad.2013.03.019>
- Yousefi, B., Shin, J., Schumacher, E. H., & Keilholz, S. D. (2018). Quasi-Periodic Patterns of Intrinsic Brain Activity in Individuals and their Relationship to Global Signal. *NeuroImage*, *167*, 297–308.
<https://doi.org/10.1016/j.neuroimage.2017.11.043>
- Yu-Feng, Z., Yong, H., Chao-Zhe, Z., Qing-Jiu, C., Man-Qiu, S., Meng, L., Li-Xia, T., Tian-Zi, J., & Yu-Feng, W. (2007). Altered baseline brain activity in children with ADHD revealed by resting-state functional MRI. *Brain and Development*, *29*(2), 83–91. <https://doi.org/10.1016/j.braindev.2006.07.002>
- Yushkevich, P. A., Piven, J., Hazlett, H. C., Smith, R. G., Ho, S., Gee, J. C., & Gerig, G. (2006). User-guided 3D active contour segmentation of anatomical structures: Significantly improved efficiency and reliability. *NeuroImage*, *31*(3), 1116–1128.
<https://doi.org/10.1016/j.neuroimage.2006.01.015>
- Zarahn, E., Aguirre, G. K., & D’Esposito, M. (1997). Empirical Analyses of BOLD fMRI Statistics. *NeuroImage*, *5*(3), 179–197. <https://doi.org/10.1006/nimg.1997.0263>

- Zerbi, V., Floriou-Servou, A., Markicevic, M., Vermeiren, Y., Sturman, O., Privitera, M., von Ziegler, L., Ferrari, K. D., Weber, B., De Deyn, P. P., Wenderoth, N., & Bohacek, J. (2019). Rapid Reconfiguration of the Functional Connectome after Chemogenetic Locus Coeruleus Activation. *Neuron*, *103*(4), 702-718.e5.
<https://doi.org/10.1016/j.neuron.2019.05.034>
- Zhou, J., Greicius, M. D., Gennatas, E. D., Growdon, M. E., Jang, J. Y., Rabinovici, G. D., Kramer, J. H., Weiner, M., Miller, B. L., & Seeley, W. W. (2010). Divergent network connectivity changes in behavioural variant frontotemporal dementia and Alzheimer's disease. *Brain: A Journal of Neurology*, *133*(Pt 5), 1352–1367.
<https://doi.org/10.1093/brain/awq075>
- Zou, Q.-H., Zhu, C.-Z., Yang, Y., Zuo, X.-N., Long, X.-Y., Cao, Q.-J., Wang, Y.-F., & Zang, Y.-F. (2008). An improved approach to detection of amplitude of low-frequency fluctuation (ALFF) for resting-state fMRI: Fractional ALFF. *Journal of Neuroscience Methods*, *172*(1), 137–141.
<https://doi.org/10.1016/j.jneumeth.2008.04.012>